Dissertation
submitted to the
Combined Faculties for the Natural Sciences and for Mathematics
of the Ruperto-Carola University of Heidelberg, Germany
for the degree of
Doctor of Natural Sciences

presented by
Jakob Walcher
born in Darmstadt, Germany
oral examination: 26. January 2005

The nuclei of bulge-less galaxies

Referees: **Prof. Dr. Hans-Walter Rix**
Prof. Dr. Rainer Spurzem

Zusammenfassung

Als Beitrag zur Vervollständigung unseres Wissens über Galaxienzentren wurde die Zentral-Region sehr später (bulge-loser) Spiralgalaxien untersucht. Die besonders hellen (10^6 – 10^8 $L_\odot$), aber kompakten ($r_e \sim 5$ pc) Sternhaufen, die von Böker et al. (2002) in den Zentren dieser Galaxien gefunden wurden, wurden mit UVES am VLT spektroskopiert. Die Geschwindigkeitsdispersionen wurden bestimmt und verwendet um die Massen der Sternhaufen zu bestimmen, die zwischen 8×10^5 und 6×10^7 $M_\odot$ liegen. Von denselben Spektren wurden die mittleren Alter der Sternhaufen bestimmt (3×10^6 bis 3×10^9 Jahre). Die Metallizitäten betragen typischerweise 2/5 des solaren Wertes. Es konnte nachgewiesen werden, daß die Sternhaufen aus mehreren Sterngenerationen bestehen.

Aus den dynamischen Eigenschaften der Sternhaufen folgt, dass sie von der Struktur her nicht bulges, sondern anderen massereichen Sternhaufen ähnlich sind. Sie gehören zu den Objekten mit der größten mittleren Massendichte innerhalb des halb-licht Radius' im Universum. Diese Sternhaufen sind außerdem außergewöhnlich, weil sie wiederkehrende Sternenstehungszyklen durchlaufen. Diese ungewöhnlichen Eigenschaften sind vermutlich die Folge ihrer ausgezeichneten Position im Zentrum ihrer Muttergalaxien. Es ergab sich jedoch keine Korrelation zwischen den Eigenschaften des Haufens und den großskaligen Eigenschaften dieser Muttergalaxie.

Abstract

I present a study of the central region of very late type (bulge-less) galaxies, as a contribution to a full census of the nuclear properties of galaxies. The exceptionally bright (10^6 – 10^8 $L_\odot$) but compact ($r_e \sim 5$ pc) nuclear star clusters found by Böker et al. (2002) have been studied using spectra taken with UVES at the VLT. I measure the velocity dispersions of nine clusters and use these to determine masses between 8×10^5 and 6×10^7 $M_\odot$. The same spectra together with a population synthesis model yield mean luminosity weighted ages, which range between 3×10^6 and 3×10^9 years. The mean metallicities are 2/5 the solar value. It is also shown that the clusters are composed of several stellar populations with different ages.

It follows from their dynamical properties that, rather than small bulges, the closest structural kin of nuclear clusters are massive compact star clusters. Nuclear clusters are among the objects with the highest mean mass density inside the effective radius. Nuclear clusters are also exceptional in that they experience repeated episodes of star formation. The unusual properties of this type of clusters probably are a consequence of their location in the centers of their respective host galaxies. No relation could be found between the large scale properties of the host galaxy and those of the cluster.

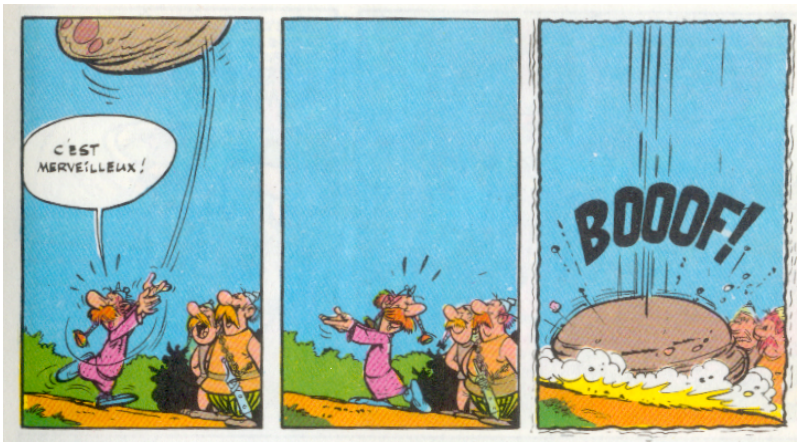

Goscinny and Uderzo (1961)

Contents

Chapter 1

Bulge-less galaxies and their nuclei

In which bulge-less spirals and their star clusters are introduced.

Supermassive black holes are present in the centers of all galaxies with a non-negligible spheroidal component (Kormendy and Richstone, 1995). Magorrian et al. (1998) showed that there is a correlation between the mass of this central dark object and the mass of the spheroid. Several other relations between the properties of the dynamically hot component of a galaxy and its central black hole have backed up these early findings (Gebhardt et al., 2000; Ferrarese and Merritt, 2000; Graham et al., 2001; Ferrarese, 2002; Häring and Rix, 2004). It has thus become increasingly clear that the evolution of galaxies is linked to the evolution of their nuclei, despite many orders of magnitude difference in scale. To explore this relation down to the least massive bulges, and therefore presumably down to the very lowest black hole masses, it is necessary to have a complete census of the nuclear properties of galaxies over the full Hubble sequence. Until recently, however, few centers of very late type, bulge-less spirals have been studied in greater detail.

It is indeed not clear that in these galaxies the center is as unique as in earlier types. Very shallow central potential wells have been measured from Hα rotation curves (e.g. Marchesini et al., 2002; Matthews and Gallagher, 2002, and references therein). The linear rise of velocity with radius goes out to several kpc in the stellar disk. It thus implies a constant surface density and a harmonic potential with a vanishing gravity vector in the central region.

The lack of a central spheroidal or bulge component shows that late type spirals are the disk galaxies in the local universe that have undergone the least dynamical heating, star formation, and angular momentum transport. They have neither experienced major mergers, nor violent bar instabilities. Both of these processes are central in the evolution of earlier type galaxies. Major mergers of galaxies are the natural consequence of the hierarchical build-up of galaxies in the cold dark matter model and are expected to be particularly frequent in the early universe.

Major mergers, however, inevitably lead to a spheroidal remnant (see e.g. Naab and Burkert, 2003) in contrast to the very definition of a late type spiral. Bars, on the other hand, are effective in transferring angular momentum to the outer disk (see e.g. Prendergast, 1983, for a review), thereby driving gas to the center of a spiral. This gas almost inevitably forms stars, which are believed to give rise to so-called 'pseudobulges' (Kormendy and Kennicutt, 2004). It is at present not clear which properties of late-type spirals make inward gas transport so inefficient during their lifetime. One might speculate that the flat dark matter potential they seem to possess might be connected to this absence of violent evolution.

Late type spirals, however, do share one central property with their earlier type cousins. It has been thought for 20 years that "the centers of some, perhaps most, galaxies contain a nuclear stellar system which is dynamically distinct from the surrounding bulge or disk components" (O'Connell, 1983). In the last decade the image quality of HST has boosted the study of the centers of spiral galaxies. These observations have indeed confirmed that star clusters are a common feature in the nuclei of spiral galaxies of all Hubble types (Phillips et al., 1996; Matthews and Gallagher, 1997; Carollo et al., 1997, 1998; Böker et al., 2002), from bulge-dominated galaxies to bulge-less galaxies. However nuclear star clusters are hard to observe in early type spirals against the bright bulge. In contrast, in late-type, bulge-less galaxies, they stand out well against the low surface brightness disk. The HST survey by Böker et al. (2002, hereafter B02) showed that 75% of all late type spirals host such a nuclear cluster in their photometric center. Throughout this thesis we use the term nuclear cluster (NC) for a luminous and compact star cluster near the overall photometric center of the galaxy. Although their effective radii (~ 5 pc, Böker et al., 2004, hereafter B04) are comparable to globular clusters, the luminosities of these NCs exceed those of the most luminous Milky Way globular clusters by up to 2 orders of magnitude.

While HST's high spatial resolution allows surface photometry of the clusters, other fundamental parameters, such as, e.g., age and mass, remain largely unknown. Several case studies in the literature, however, have revealed massive, young objects. M33 is the nearest Sc galaxy hosting a NC and its nucleus has been extensively studied in the past (e.g. van den Bergh, 1976; Gallagher et al., 1982; Hernquist et al., 1991; Davidge, 2000; Long et al., 2002; Stephens and Frogel, 2002). Despite some differences in the details, all studies on M33 agree that there is a stellar population younger than 0.5 Gyr in the central parsec and that star formation has varied significantly over the past several Gyrs. The mass of the central cluster in M33 was estimated from a detailed population analysis in Gordon et al. (1999) to be 5×10^5 $M_\odot$, consistent with the upper limit derived from the velocity dispersion by Kormendy and McClure (1993) of 2×10^6 $M_\odot$. From Hα rotation curves of late type spirals, Matthews and Gallagher (2002) found that the velocity offsets at the position of five semi-stellar nuclei — which are certainly to be identified with NCs

— are consistent with masses of $\approx 10^6$ – 10^7 $M_\odot$. They also noted that the location of the cluster and the dynamical center of the galaxy do not always coincide. The only direct mass determination for a NC from a measurement of the stellar velocity dispersion and detailed dynamical modeling was done for the NC in IC34 by Böker et al. (1999); they found 6×10^6 $M_\odot$, with a K-band mass-to-light ratio of 0.05 in solar units. The derived mean age is $\leq 10^8$ years. Böker et al. (2001) also studied the NC in NGC4449 using population synthesis models. They estimated an age of $\approx 10^7$ years, in agreement with Gelatt et al. (2001), and inferred a lower limit for the mass, of 4×10^5 $M_\odot$.

In the absence of any obvious bulge (Böker et al., 2003b), NCs represent the closest thing to a central "hot component". The almost ubiquitous presence of NCs at the same physical location in their host galaxy as a bulge would have brings up the question whether bulges and NCs are related. A plausible scenario would be that NCs are protobulges that grow by repeated accretion of gas and subsequent star formation. The pace of that growth and the resulting size of the central component would then determine whether we call the central component a NC or a small bulge. The available sizes, masses and ages, however, suggest a more likely kinship is that between NCs and either globular clusters (GCs), super star clusters (SSCs) or the nuclei of dwarf ellipticals (dE). Alternatively, NCs could be a new class of objects which would then be part of the wide range of special phenomena occuring in galaxy centers. To establish the nature of these objects, we clearly need reliable determinations of the velocity dispersion, σ, and thereby masses as well as ages for a statistically significant sample of objects. This thesis presents the results of a project carried out using spectra from UVES at the VLT with the goal of determining these fundamental parameters for a sample of nine nuclear clusters.

Chapter 2

Measuring velocity dispersions

Where we present a fundamental tool.

Dynamically hot stellar systems are supported against gravitational collapse through the random motion of their stars. The exact distribution of stars in phase space depends on the internal structure and therefore on the history of the system under consideration. The velocity dispersion is defined as the root mean square of the stellar velocities. In practice one finds that velocity distributions are usually roughly Gaussian. For a Gaussian, the velocity dispersion is identical to the Gaussian σ.

For unresolved stellar populations the velocity dispersion is usually measured along the line of sight through the Doppler broadening of absorption lines. Stellar kinematic analyses assume that an observed galaxy spectrum can be represented by the convolution of one or several stellar templates with a broadening function. The linewidth in the template spectra represents both the intrinsic width of the stellar photospheric lines and the instrumental broadening. This assumption is best satisfied when the template spectra have been taken with the same instrumental setup and atmospheric conditions as the galaxy spectra. The galaxy spectra are then presumed to only differ by the additional Gaussian line-of-sight-velocity distribution (losvd), reflecting the velocity dispersion of the stars. Bulk rotation of the system, multiple kinematic components or coexistence of a dynamically hot system with a cold gaseous or stellar disk can change the shape of the losvd significantly. In those cases where one has good reason *a priory* to expect exactly two distinct kinematic subcomponents, a decomposition into two Gaussians is a possible approach. More generally, Gauss-Hermite polynomials (van der Marel and Franx, 1993) can be used to quantify the deviations from Gaussianity. However, for the data used in this thesis, we will limit ourselves to measuring the velocity dispersion itself, which will prove to be challenging enough.

2.1 Methods for estimating the velocity dispersion

Several methods have been introduced in the literature to measure the line-of-sight velocity distribution of galaxy spectra. Methods that perform a deconvolution, i.e. compute the broadening function analytically, are, e.g., the Fourier quotient (Simkin, 1974; Sargent et al., 1977), the cross correlation (Tonry and Davis, 1979) and the Fourier correlation quotient (Bender, 1990) methods. The best-fitting parameters of the losvd can however also be determined by minimizing, in a χ^2 sense, the difference between a broadened template spectrum and the galaxy spectrum. The later approach has the advantage of making the error analysis more straightforward. In particular, χ^2 provides a convenient way to assess the quality of the fit, i.e., the validity of the underlying assumption that the galaxy spectrum differs from the template by the broadening only.

Let the galaxy spectrum be called $g(n)$, where n is an index indicating the bin (pixel) in the spectrum. The standard deviation of the galaxy spectrum is $\sigma(n)$ and the template spectrum is accordingly called $t(n)$. The assumption is that $g(n)$ is the convolution of the template with a broadening function $b(n)$. That is

$$g(n) = b(n) \circ t(n). \tag{2.1}$$

Here $\circ$ means the convolution product. In the direct pixel fitting method (Rix and White, 1992), the best fitting parameters of the broadening function $b(n)$ are now estimated by directly minimizing the expression

$$\chi^2(b) = \sum_n \left[\frac{t(n) \circ b(n) - g(n)}{\sigma(n)} \right]^2 \tag{2.2}$$

In brief, a biased random walk is performed that ends up in the global minimum of the χ^2 plane. As this method will be used throughout this thesis, details will be given in Section 2.2. This approach is however computationally expensive, as each step of the random walk requires one convolution. However, such a fit can be done equivalently in either pixel space or Fourier space. Let $G(k)$ be the Fourier transform of $g(n)$. Then Parsevals' Theorem states that

$$\int_{-\infty}^{\infty} \mid g(n) \mid^2 dn = \frac{1}{2\pi} \int_{-\infty}^{\infty} \mid G(k) \mid^2 dk, \tag{2.3}$$

therefore χ^2 in the pixel domain is proportional to χ_f^2 in the Fourier domain. The Fourier transform of $t \circ b - g$ is $TB - G$. Inserting Equation 2.2 into Equation 2.3 therefore yields

$$\chi_f^2 = \sum_n [T(n)^* B(n)^* - G(n)^*][T(n)B(n) - G(n)]. \tag{2.4}$$

Minimizing Equation 2.4 is computationally less expensive because the convolution is replaced by a multiplication. It remains, however, an underlying assumption for every method involving Fourier transforms that the spectra are infinite (or periodic) and continuous, which is never fulfilled in real data. The pixel fitting method further makes the masking of emission lines straightforward, something that could only be achieved with Fourier methods by applying complex window functions.

2.2 Description of the code `losvdfit`

We use a code that simultaneously matches a linear combination of template stars and the width of a single Gaussian broadening function. No Fourier transform is involved, as the code works directly with the measured spectra. Each pixel in the spectrum is weighted with its specific error during the fitting process. The mathematical details of the method are described in Rix and White (1992), we will however repeat some of these details pertinent to the implementation of the method. The code was originally written by Hans-Walter Rix in 1992, it has however been largely rewritten for transparency and several new features have been added in the course of this thesis work. This Section will cover some of the details of the input and setup as well as its internal workings, and is intended to be a reference for other users of the code. The code is basically a wrapper to iterate minimization of the χ^2 quantity described in Equation 2.2 and the determination of the best-fitting linear superposition of the available template stars.

The input to the code consists of one-dimensional FITS (Flexible Image Transport System) files (for a description of FITS see http://fits.gsfc.nasa.gov/). To read in and output the FITS file the code uses the `cfitsio` library (Pence, 1999). The object spectrum, its error and the template spectra need to be rebinned in $\log(\lambda)$ to make velocity shifts linear in pixel space. The broadening can then be thought of as resulting from a superposition of the templates, shifted in pixel space (or velocity space) to represent the various motions of the constituent stars of the galaxy.

The code also allows us to correct for the effects of extinction. We use the extinction law of Cardelli et al. (1989), which is appropriate for non-starbursting systems. These authors parameterize the extinction, $A(\lambda)$ in magnitudes, at any given wavelength as depending on the absolute extinction at a chosen reference wavelength (conventionally chosen to be $A(V)$), and a shape parameter, R_v, defined as $R_v \equiv A(V)/E(B-V)$. The mean extinction law then takes the form

$$< A(\lambda)/A(V) >= a(x) + b(x)/R_v, \tag{2.5}$$

where $a(x)$ and $b(x)$ are tabulated in their paper and $x \equiv 1/\lambda$. The free parameters are the extinction in magnitudes and the effective wavelength at which it

applies. This extinction is then applied to all of the templates prior to the fitting process. Following Cardelli et al. (1989), we choose $R_v = 3.08$.

In the spectra of galactic nuclei a non-thermal continuum can be present. Therefore the projections (in a linear algebraic sense) of the spectra onto a specified set of orthonormal polynomials can be subtracted from them. Note that this is NOT a substitute for correction of the instrumental response function (flux-calibration in relative terms) of the spectra. Continuum subtraction is an additive procedure, while response correction is multiplicative. For spectra covering a significant range in wavelength, the relative strengths of the different absorption lines in non-response corrected spectra will not be correct. This caveat does not apply if templates and object spectrum were taken with the same instrument, as then the response function of the spectra will be identical.

A further complication in the analysis of real galaxy spectra is the possible presence of 1) emission lines, 2) CCD defects covering small wavelength regions or 3) bright telluric emission line bands that cannot be well subtracted during the reduction. The code allows us to define wavelength regions that are excluded from the fit. The standard deviations of the corresponding pixels in the galaxy spectrum are set to a very high value, thereby effectively removing them from the χ^2 sum. It should be pointed out here that this simple trick is exclusively possible with the pixel fitting method.

When recovering the losvd from the galaxy spectra, the results can be affected by a mismatch between the templates and the object (i.e., a breakdown of the assumption that the two spectra really only differ by the broadening). To minimize these problems, we can create a template of composite spectral type from a library of templates. In practice we choose an iterative approach, i.e., we first determine a first approximation for the broadening from a fit to an initial single template. We then construct the composite template which best matches the object for this fixed broadening. Then we determine a new broadening estimate, using this composite template.

The best velocity distribution is determined by assuming that it is drawn from a parameterized model. In this version, the model is assumed to be a Gaussian described by three parameters: amplitude A, velocity shift v, and velocity dispersion σ_0. The task is simply to find the set of parameters that minimizes the difference between the model and the object spectrum (non-linear χ^2 minimization). The minimization method used here is a χ^2-biased random walk (for the basic concepts see Chapter 10.9, "Simulated annealing", in Press et al., 1992). Starting from initial guess values for the parameters, the random walk generates new, random, parameter values for each step. After computing χ^2, these values are accepted if

$$R \leq \exp(-\Delta\chi^2/T)), \tag{2.6}$$

where R is a random number between 0 and 1 (i.e., a parameter change that

makes χ^2 smaller is always accepted) and T is a control parameter. T is similar to a temperature, with an annealing schedule by which it is gradually reduced. After three passes with diminishing step values for the parameter changes and diminishing values of T, the solution is considered to have converged. The velocity and velocity dispersion parameters are not allowed to vary by more than a factor of ten times the initial guess for the velocity dispersion to avoid unnecessary steps in the random walk.

After applying the resulting estimate for the broadening to all templates in the library, the best linear superposition of these templates is determined. Again in brief, the galaxy spectrum $g(n)$ (with standard deviation $\sigma(n)$) is expected to be described by

$$g(n) = \sum_{k=1}^{M} a_k t(n), \tag{2.7}$$

where a_k are weighting factors and the M broadened template spectra are denoted by $t(n)$. For this linear model, a merit function is defined as

$$\chi^2 = \sum_n \left[\frac{g(n) - \sum_{k=1}^{M} a_k t(n)}{\sigma(n)} \right]^2 . \tag{2.8}$$

The minimum of Equation 2.8 occurs where the derivative of χ^2 with respect to all M parameters vanishes. This translates into a matrix problem which can be solved conveniently as a non-negative least squares problem (`nnls`, Lawson and Hanson, 1974) that has a unique solution. Although the template spectra are of course non-linear, in this discussion "linear" refers only to the model's dependence on its parameters. This procedure does not only allow us to determine the best fitting template for a kinematic analysis. The `nnls` routine calculates the relative weights (contribution) of each template spectrum to the galaxy spectrum. With a suitable choice of template library, these can be used to understand the physical composition of the galaxy spectrum. Which and how many templates to use depends on the physical question that one wants to ask. Note that the present version of the code does not normalize the templates to the galaxy spectrum. Weights need to be interpreted accordingly. In Chapter 5 we will use population synthesis models as the template library. For the purposes of this work, the mass-to-light ratios of the composite template can be calculated by the code from weights given in one of the input files. More details will be given in Chapter 5.5.

To improve the estimate of the velocity dispersion, a specifiable number of outlier pixels (as compared to the best fitting template) in the galaxy spectrum is excluded from further fitting. Then the χ^2-biased random walk is repeated and the final velocity shift and velocity dispersion are written to the logfile.

Chapter 3

Data description

In which we sample, observe and reduce.

The observation of nuclear star clusters is a challenging task. They are comparatively faint systems (typically ≈ 19 mag in I band) with small sizes and small velocity dispersions. This thesis combines data from two of the world's forefront observatories, the Hubble Space Telescope (HST, NASA and ESA) and the Very Large Telescope (VLT, ESO).

3.1 Hubble Space Telescope imaging data

The imaging data was taken with the HST Wide Field and Planetary Camera 2 (WFPC2) and was described in detail in B02 and B04. We will only repeat some central points here which are relevant to this thesis. Galaxies in this snapshot survey were selected to have Hubble types between Scd and Sm, to have line-of-sight velocities $v_{hel} < 2000$ km s^{-1} and to be nearly face-on. The galaxy center was centered on the PC chip which has a pixel size of $0.0464''$ and a field of view of $36'' \times 36''$. The F814W filter was used, which corresponds approximately to the I-band. The images for the nine nuclear clusters in our UVES sample are shown in Figure 3.1

Isophotal fits were performed in B02, which yielded the location of the photocenter and the surface brightness profile (SBP). A nuclear cluster was identified in this photocenter in 75% of the cases. The observed distribution of cluster positions relative to the photocenter position shows that the clusters indeed occupy the photocenter to within the measurement error of its position. Visual inspection of the surface brightness profile was then used to derive the radius R_u of the distinct upturn in the SBP caused by the presence of the NC. Cluster luminosities were then derived from the integrated luminosity inside R_u, subtracting an inward extrapolation of the disk surface brightness profile.

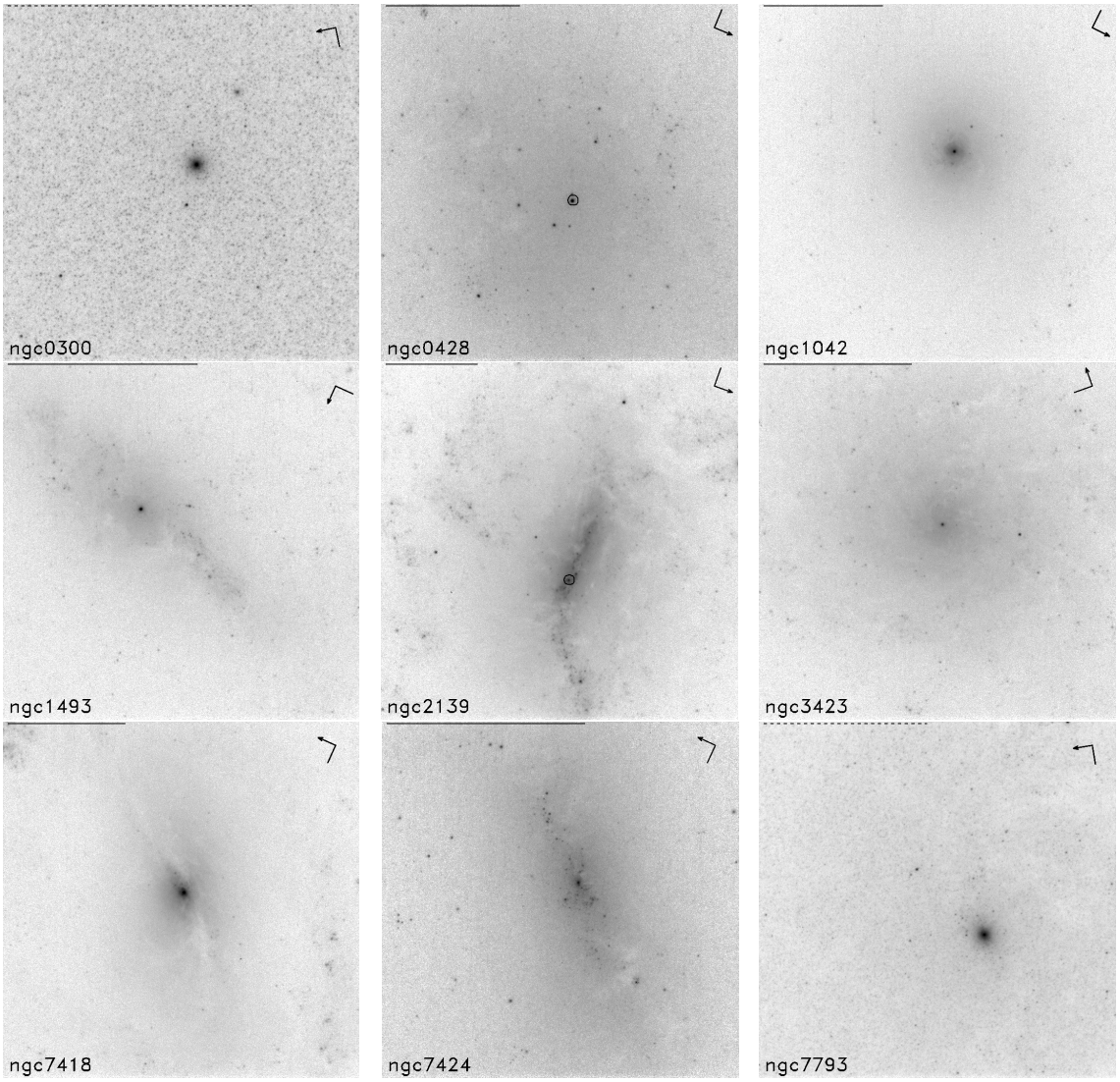

Figure 3.1: The HST/WFPC2 I-band images as presented originally in B02. Solid bars in upper left corners represent a scale of 1 kpc; dotted bars bars indicate 250 pc. Symbols in top right corners indicate North (*arrow*) and East directions. Objects identified as the central clusters are circled in sources where a visual identification may be ambiguous.

Accurate effective radii r_e were determined for this nuclear cluster sample in B04. For their analysis, B04 used the software package `ISHAPE` (Larsen, 1999) to fit PSF-convolved King or Moffat profiles with different concentration indices to the data. Although about half of the clusters have r_e that are smaller than the FWHM of the HST PSF of 0.07″, r_e can be determined reliably from the outer parts of the profile. They thus found a median effective radius of $< r_e >= 3.5$ pc, with 50% of the sample falling between 2.4 pc and 5.0 pc. This narrow size distribution is indistinguishable from that of Galactic globular clusters.

3.2 UVES data description and reduction

A subset of 9 nuclear clusters from the 75 objects in the sample of B02 were observed with UVES at the VLT.

3.2.1 Sample selection

The observed objects are listed in Table 3.1. They were selected from the full catalogue to be accessible on the sky and to be bright enough to be observed in less than three hours, maximizing the number of observable objects. We thus sample the brighter 2/3 of the luminosity range covered by the clusters identified from the HST images (see Figure 3.2). Whether this bias in absolute magnitude introduces others, either towards younger or more massive clusters, is at present unclear.

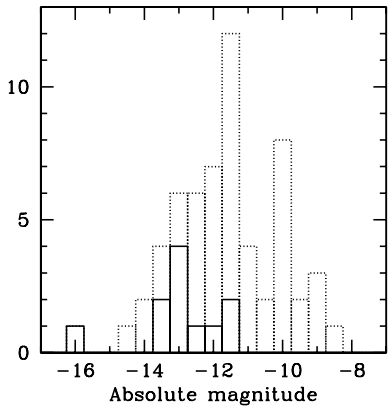

Figure 3.2: Histogram of the clusters observed with UVES (solid line) compared to the full sample of B02 (dotted line).

3.2.2 Observations

The VLT spectra were taken with the Ultraviolet and Visual Echelle Spectrograph (UVES) attached to Kueyen (UT2) during three nights of observation from the 9th to the 11th of December 2001. All nights were clear with a seeing around 0.8″. UVES can work in parallel at blue and red wavelengths by using a dichroic beam splitter that divides the light from the object at the entrance of the instrument. Our main goal was to derive ages from the spectral region around the Balmer break and velocity dispersions from the Calcium Triplet. In order to also include the Hα line we chose a non-standard setting with the dichroic #2 and the

Table 3.1: Sample and observations

Galaxy	type	Distance [Mpc]	m_I	M_I	S/N	Apert. [″]	NCL [%]
(1)	(2)	(3)	(4)	(5)	(6)	(7)	(8)
NGC 300	SAd	2.2	15.29	-11.43	37	1.09	0
NGC 428	SABm	16.1	17.95	-13.15	16	0.93	30
NGC 1042	SABcd	18.2	18.40	-12.95	24	0.93	81
NGC 1493	SBcd	11.4	17.17	-11.43	20	1.24	33
NGC 2139	SABcd	23.6	19.28	-12.65	19	1.24	89
NGC 3423	SAcd	14.6	19.04	-11.84	15	0.93	76
NGC 7418	SABcd	18.4	15.12	-16.23	41	1.40	18
NGC 7424	SABcd	10.9	18.80	-11.41	16	1.55	77
NGC 7793	SAd	3.3	14.00	-13.64	65	1.55	0

Cols. (1) and (2) Galaxy name and type as taken from NED. Col. (3) Distances were taken from B02, where they were calculated from the recession velocity (from LEDA, corrected for virgocentric infall) and assume $H_0 = 70$ km s^{-1}. Col. (4) and (5) Apparent and absolute magnitude of the NC as taken from Böker et al. (2002). Col. (6) Signal-to-noise per pixel ($\sim$ 0.07 Å) in the region around the Calcium Triplet. Col. (7) Width of the extraction aperture in spatial direction. Col. (8) Contamination from galaxy disk light in percent, measured as described in Section 3.2.3.

crossdispersers #2 and #4 centered on the wavelengths 4200 and 8000 Å. The resulting wavelength range is thus 3570 – 4830 Å in the blue arm; the red arm spectra are imaged on two CCDs, one (called "lower red") covering 6120 – 7980 Å and the other one (called "upper red") covering 8070 – 9920 Å. The length of the slit was 10″, the width 1″. The slit was always oriented perpendicular to the horizon to minimize effects of differential refraction. The spectral resolution is ≈35000 around the Calcium Triplet as measured from sky lines. This corresponds to a Gaussian dispersion of the instrumental line-spread function of 3.4 km s^{-1}. The pixel size in the reduced spectra is $\sim$ 0.07 Å. Because the effective radii r_e determined for the clusters in B04 are smaller than 0.2″ for all observed clusters, they are much smaller than the seeing disk and we thus essentially measure integrated properties. The observed NCs together with exposure times are listed in Table 3.1. The HST images for all objects in our sample can be found in B02.

We also observed a number of template stars of known spectral type ranging from B to K and listed in Table 4.1. As will be explained in Section 4.1 these are used to reliably measure the velocity dispersion of the NCs.

3.2.3 Reduction

The data were reduced with the UVES reduction pipeline version 1.2.0 provided by ESO (see "UVES pipeline and Quality Control User's Manual" prepared by P.Ballester et al. (2001) and the website: http://www.eso.org/instruments/uves/). For each observing night the following steps for preparing the calibration database were performed: first, using a physical model of UVES a first guess wavelength solution was determined. Then the order positions were identified from an order definition flatfield. Next the final wavelength calibration was done using a ThAr-lamp exposure. Finally master bias and master flatfields were created from the median of five input frames each.

Cosmic ray removal was done on the 2-D science frames by means of the MIDAS routine `filter/cosmic`. The science frames were then bias subtracted and the interorder background was subtracted by fitting a spline function to the grid of background positions. For each background position the median of pixels within a certain window was used as the measurement at that point. The flatfielding was not done on the 2D raw frames, but after extraction for each order on the extracted 1D spectrum. The extraction can be done using either an optimal extraction method or a simple average over a predefined slit. For our high signal-to-noise (S/N) data we found that the optimal extraction method shows quality problems appearing as sudden spikes and ripples, especially in the blue. We were able to recover almost the same S/N with the average method also for the lower S/N spectra by fine-tuning the extraction parameters (position and width of the extraction slit and position of the sky windows). We verified that the noise we derive is consistent with expectations from a combination of read-out noise and Poisson statistics. For consistency we therefore decided to extract all spectra with the average method. In Table 3.1 we list the width of the extraction apertures used for each single spectrum as well as the S/N values around the Calcium Triplet. The extraction apertures have been optimized for signal-to-noise. They are therefore relatively large and lead to somewhat larger contamination fractions. For the analysis done in Section 4 S/N is however crucial to allow fitting of metal lines with small equivalent width. The apertures in the blue have been chosen to be the same to allow for a consistent interpretation.

It is important to note that background light from the galaxy disk underlying the NC is subtracted together with the sky background during extraction, so that the contamination from non-cluster light is reduced. However, not all the disk light is subtracted, because the disk brightness is not generally constant with radius. One could think of using the surface brightness profiles from B02 and scaling up the background to an extrapolated central value. However there are some ambiguities in such a procedure: the background is composed of sky and disk light. While we scale up the disk light, the sky background will be scaled up by the same factor,

which will lead to an oversubtraction of sky from the cluster light. Also the subtraction of sky emission lines in the red spectra is already now a mess. Scaling up the background light would have worsened that problem. It might be possible in principle to construct a sky emission line mask and thereby avoid this difficulty (and improve on the subtraction of sky lines in general), however that would have busted the timeline of this thesis. Finally we have no physical reason to assume that the stellar population in the disk is the same in a few parsec distance from such an exceptional object as the nuclear cluster and in a 100pc distance, which is the typical physical size of the seeing disk in the galaxy.

To quantify the fraction of cluster light in the final spectra we simulate our UVES observations using the high spatial resolution HST data. The I-band, at an effective wavelength of 8000 Å, will yield a correct fraction for the wavelength of the Ca Triplet. We convolve the HST images with a Gaussian of 0.8″ seeing. From the known slit position we can derive the position of the spectroscopic object and sky windows on the HST image. The expected total flux in the reduced object spectrum $F_{\rm spec}$ is then computed by subtracting the flux in the sky windows from that in the object window. The total flux $\mathrm{F_{cl}}$ from the cluster alone is known from the magnitudes given in B02. The fraction f of the total cluster flux that falls within the spectroscopic object window is

$$\mathrm{f} = \frac{1}{4}[\mathrm{erf}(x/\sqrt{2}\sigma) - \mathrm{erf}(-x/\sqrt{2}\sigma)][\mathrm{erf}(y/\sqrt{2}\sigma) - \mathrm{erf}(-y/\sqrt{2}\sigma)] \tag{3.1}$$

where

$$\sigma = \sqrt{\sigma^2_{\rm PSF} + \sigma^2_{\rm cluster}}, \tag{3.2}$$

and erf is the error function. Here x is half the size of the spectroscopic object extraction window along the slit and y is half the slit width. In this equation it is assumed for simplicity that the PSF and cluster are well approximated by Gaussians with the correct FWHM. Finally the contamination from non-cluster light (NCL) in the extracted spectra (as given in Table 3.1) is:

$$\mathrm{NCL} = 1 - \frac{f \times F_{\rm cl}}{F_{\rm spec}}. \tag{3.3}$$

3.3 Response correction

The UVES pipeline delivers extracted spectra which are de-biased, flattened, background subtracted, wavelength calibrated and extracted. These data come in non-physical units ('quasi-ADU'), with their large-scale slope determined by the ratio of stellar and flat field spectral slopes. More specifically, flatfielding corrects for the pixel-to-pixel variation in sensitivity of the detector. However the transmission of the instrument optics as well as that of the atmosphere (called the response function)

depends on wavelength too. Flux calibrated spectra can therefore only be obtained by comparison with a calibrated flux standard star.

To this end, the standard star measurement are processed by the pipeline into the flat-fielded, extracted and wavelength-calibrated result. This pipeline product can then be further processed (which includes extinction correction, normalization for exposure time, binning and gain) into the normalized standard star spectrum, f_{std}. This corrected to the lower spectral resolution and divided by the tabulated flux, F_{std}, of the standard star, finally yields the response curve, R:

$$R = \frac{F_{std}}{f_{std}} \tag{3.4}$$

where F_{std} is in physical units (erg/[s cm^2 Å]) and f_{std} is in arbitrary units (quasi-ADU). Having determined a reasonable response curve R, this can readily be used to flux-calibrate any point-source object spectrum, f_{obj}:

$$F_{obj} = f_{obj} \times R. \tag{3.5}$$

Two different spectrophotometric standard stars were observed on two of the three nights, albeit with a small range in zenith distance. We therefore have no means to accurately correct for the atmospheric extinction. However it is possible to flux-calibrate the spectra in relative terms, i.e. for the continuum shape. Figure 3.3 shows the two response curves we obtained, which agree to a level of approximately 2%. We will use this number as an estimate on the accuracy of our response correction.

3.4 Final data products

Two of the nine star clusters were observed on two different nights (NGC7418 and NGC7424). To combine these two spectra into one we used the following optimal weight scheme: Let f_1 be the spectrum of the first night and f_2 be the spectrum of the second night, with the associated standard deviations σ_1 and σ_2. Then the combination spectrum f with the highest S/N ratio is given by

$$f = \frac{f_1\sigma_1^{-2} + f_2\sigma_2^{-2}}{\sqrt{\sigma_1^{-2} + \sigma_2^{-2}}}. \tag{3.6}$$

Figures 3.4 to 3.6 show the reduced, response corrected, sky-subtracted spectra of all nine star clusters in the three segments that are dictated by the data, namely the blue CCD chip and the two red CCD chips. For presentation purposes the spectra have been adjusted arbitrarily to fit at their specific location on the plot. Some of the residuals of prominent telluric emission lines have been clipped in the

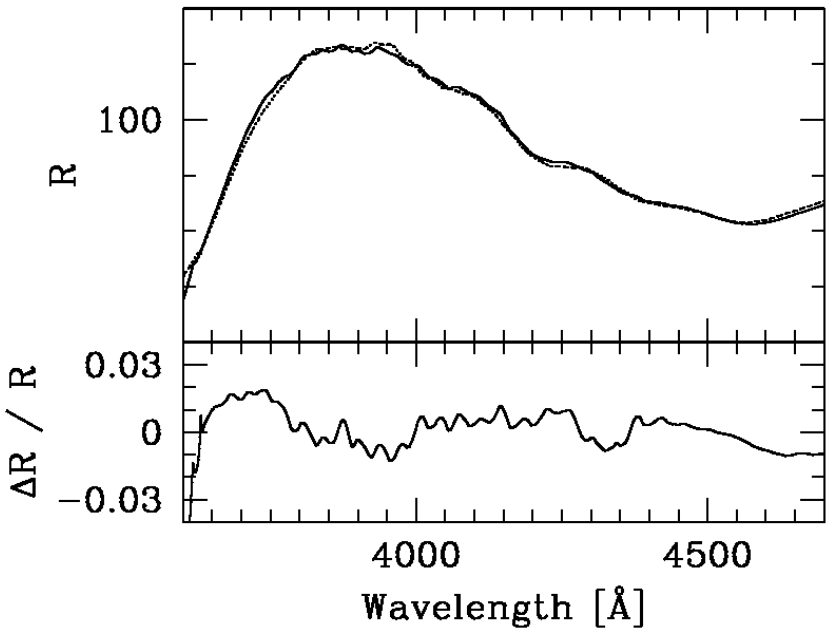

Figure 3.3: Two response curves obtained from two different spectro-photometric standard stars on two different nights. Note that they agree to $\approx 2\%$.

red spectra. The nuclear clusters are ordered approximately in the age sequence that will be derived in Chapter 5, young on top.

In the red spectra considerable residuals from telluric emission lines remain. These are due to the long exposure times that were needed for the faint clusters, causing saturation for some lines. This problem is therefore less severe for NGC7793, NGC7418 and NGC300, which had the shortest exposure times. Additionally deep atmospheric absorption bands occur (e.g. around 6850 and around 7600 Å). Large parts of the red spectra therefore can not be used for the analysis. These unusable regions have been shaded in the plots. Fortunately the interesting regions around the Hα line (6385 – 6525 Å, the Hα line itself is mostly seen in emission) and around the Ca Triplet (8400 – 8900 Å, in absorption) are relatively free of telluric features. Although the red spectra do not "look nice" in this representation, information can be extracted reliably as will be shown in the next chapters.

Out of the 9 objects, 6 show prominent emission lines of OII, Hα, Hγ, NII and SII. However emission lines do not only occur in the clusters. For most of the objects, extended emission in the disk occurs too, which often shows a complex velocity structure. As the disk light is subtracted as "sky" during the reduction process, the emission lines in the sky-subtracted spectra therefore do not bear any resemblance to the true emission line profiles.

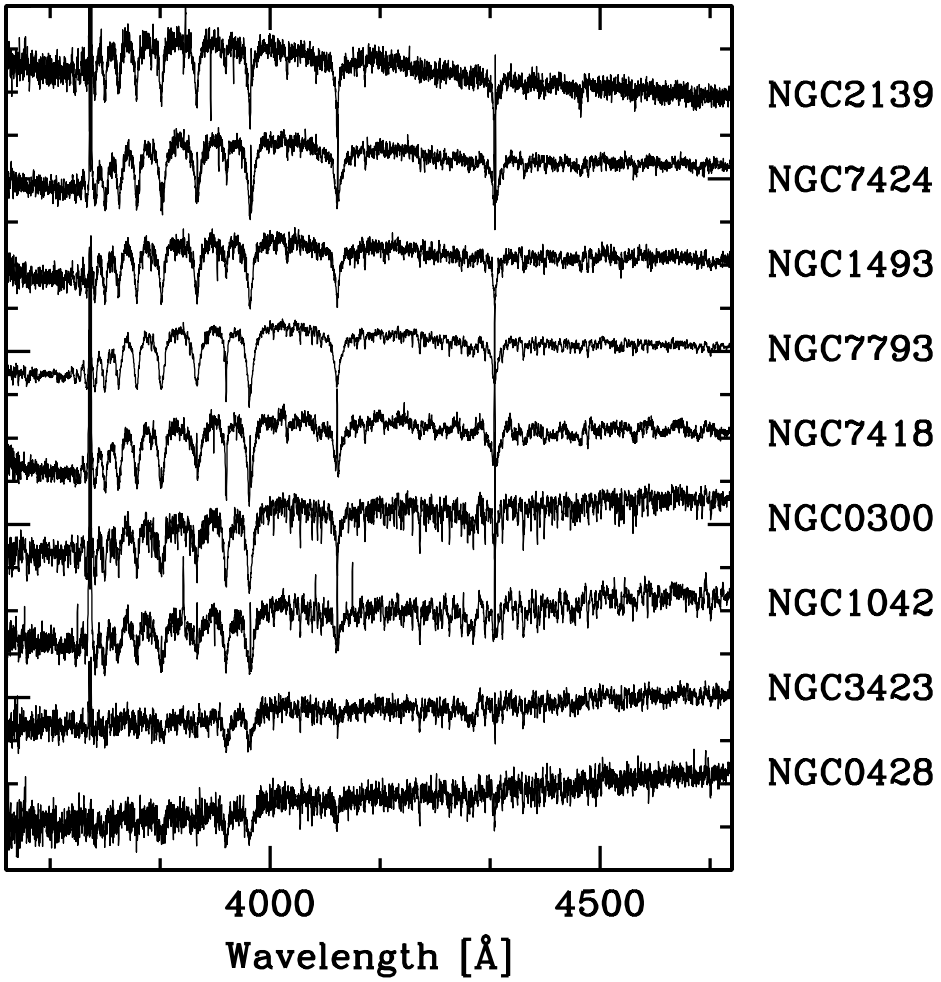

Figure 3.4: The reduced, response corrected blue spectra of the nine star clusters.

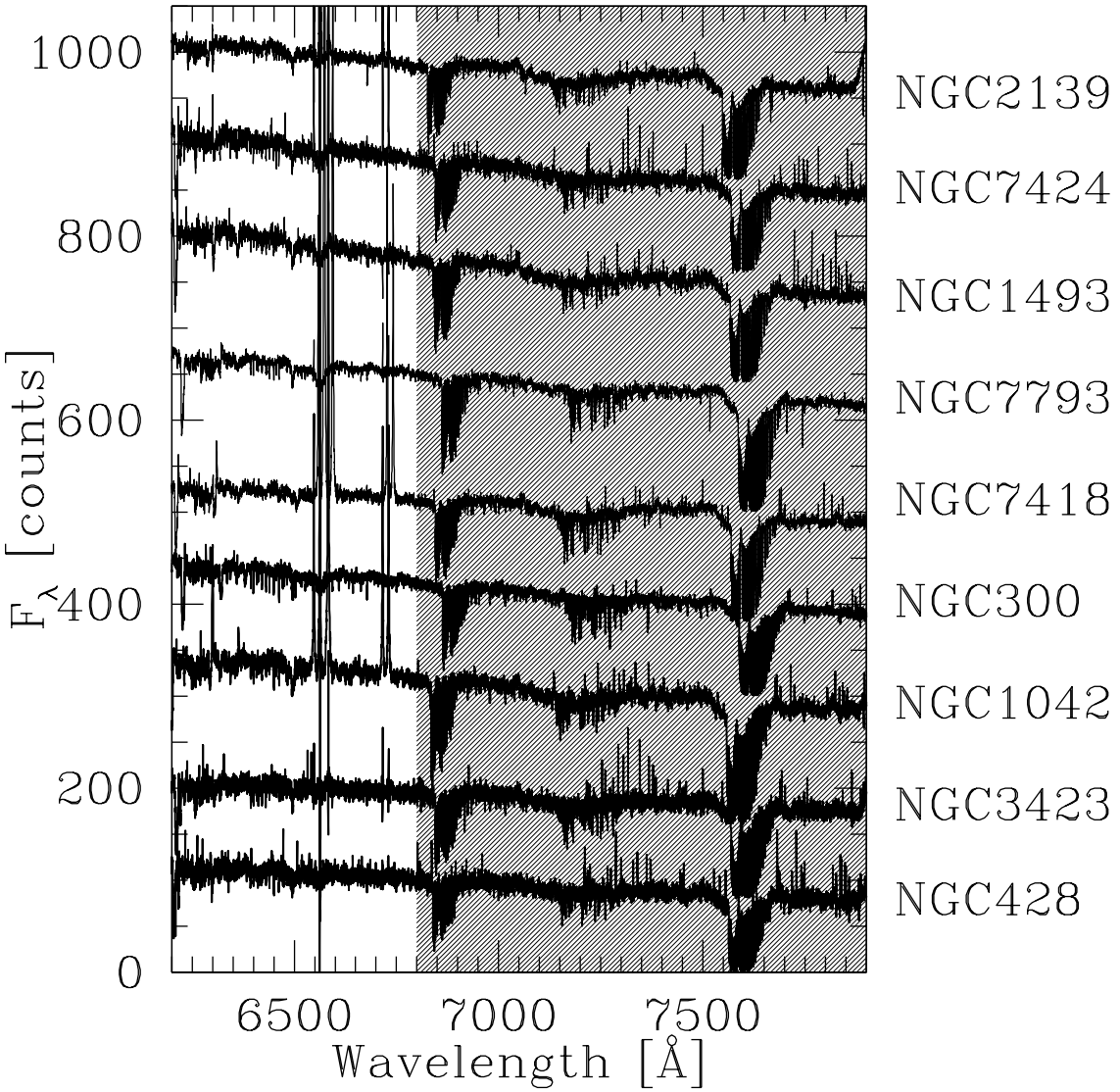

Figure 3.5: The reduced, response corrected lower red spectra of the nine star clusters. In the shaded region the spectra are dominated by telluric features and will not be used for analysis.

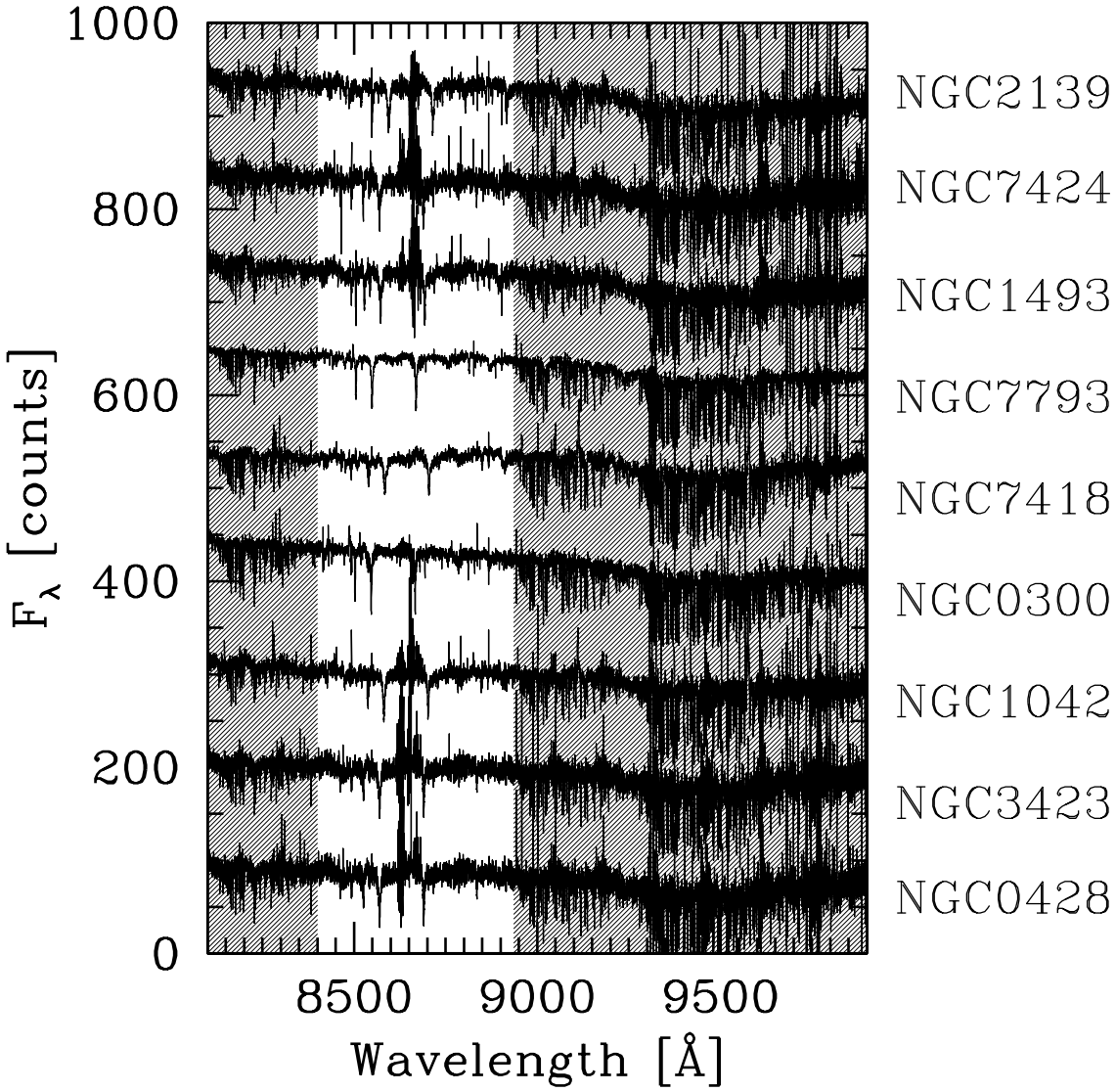

Figure 3.6: The reduced, response corrected upper red spectra of the nine star clusters. In the shaded region the spectra are dominated by telluric features and will not be used for analysis.

Chapter 4

Mass measurements

Where our sample clusters get their velocity dispersion, their surface brightness profile and finally their mass measured.

4.1 Velocity dispersions

The code we use to measure velocity dispersions has been introduced in Chapter 2. It has been pointed out there that particular care has to be taken to observe template and scientific target with the same instrumental setup in order to avoid resolution mismatch interpreted as velocity dispersion differences. In typical cases of velocity dispersion measurements, i.e. for massive galaxies, the Doppler broadening dominates the instrumental broadening and the intrinsic linewidth by a wide margin, and the estimated velocity dispersion is nearly insensitive to the choice of spectral type of the template stars. This is however not the case for the objects in our sample as we will show that their measured velocity dispersions range from only 13 to 34 km s^{-1}. We use the seven template stars ranging from type B to K listed in Table 3. An inherent strength of the code is the ability to determine an optimized template from the linear combination of the available template stars. It is thus possible to account to some extent for the influence of the generally young mean age of the clusters on the intrinsic width of the absorption lines. A further advantage of the direct fitting in pixel space is that masking spectral regions, which is essential to our analysis, is straightfoward.

Velocity dispersions are measured from the spectral region around the Calcium Triplet. We choose the largest region that is relatively free of telluric absorption bands and emission lines (8400 – 8900 Å, see below). The Calcium Triplet region does not only include the very prominent Ca II lines, but also several other metal lines whose width can be measured at our signal-to-noise ratio. Other regions of common use to measure velocity dispersions (as e.g. the CO bandhead in the infrared, see e.g. Böker et al. (1999) or the region around 5100-5500 Å as in Maraston

et al. (2004)) are not covered by our data. We however also investigated two other regions of the observed spectrum, namely 6385 – 6525 Å and 4380 – 4800 Å which are also free of telluric lines and do have other metal lines. The measured velocity dispersions agree to 15 % for those clusters where the signal-to-noise ratio of the metal lines is sufficient to measure σ reliably. These are most notably the old clusters NGC300 and NGC428 and the high signal-to-noise spectrum of NGC7793. The Calcium Triplet has been shown to give reliable results for old stellar populations, e.g. in elliptical galaxies, by a variety of authors (e.g. Dressler 1984; Barth, Ho & Sargent 2002). However, as the analysis of the blue parts of the UVES spectra show (see Chapter 5), some of our objects have ages between 10^7 and 10^8 years. Unfortunately, kinematic measurements are more complicated in populations significantly younger than 1 Gyr. Although the intrinsic width of the Ca triplet changes only slightly from main-sequence K to late F stars, for earlier types rotation and temperature cause the intrinsic width to increase rapidly. Further, in supergiants the damping wings of the Voigt profile become increasingly important due to the depth of the lines. It is in this context very unfortunate that we do not have a supergiant in our stellar template set. A further complication comes from the presence of intrinsically broad absorption lines from the Paschen series. Especially the lines Pa16, Pa17 and Pa13 (8504.8, 8547.7 and 8667.9 Å, respectively) overlap with the Ca-Triplet lines. All of these effects lead to an overestimation of the velocity dispersion, if only measured from main sequence stars. We thus need to analyze carefully the composition of the stellar populations under consideration. On the other hand the intervening Paschen absorption lines provide an additional diagnostic tool for the age of the population. With good signal-to-noise in the spectra this can be used to constrain the optimal stellar template mix for the velocity dispersion determination. For all spectra we also have age information from the blue parts of the spectrum. While we use this information for assessment of age related problems, a more detailed analysis of the age composition of the clusters will be covered in Chapter 5

To assess the influence of the Calcium Triplet problems we follow two different approaches concerning the wavelength coverage of the velocity dispersion fits. In what we will call "case 1" we use almost the full wavelength range between 8400 and 8900 Å as the fitting region. Unfortunately, the Ca-Triplet line at 8498 Å falls onto a CCD defect in the interval from 8470 – 8510 Å, which we exclude from all fits. We thus cover the two Ca lines at 8542 and 8662 Å and further metal lines, mostly Fe I. For case 1, the χ^2 that measures the quality of the fit is dominated by the Calcium Triplet lines. In "case 2" we use only the weaker metal lines of Fe and Si in the region for the fit. These are not as deep as the Ca II lines and tend to disappear in earlier type stellar spectra, so that they are much less affected by the systematic problems with the Ca triplet mentioned above. Figure 4.1 illustrates the spectral region in use. Case 2 clearly is limited by S/N in the galaxy spectra and increases possible systematic uncertainties because of metallicity

Table 4.1: Stellar template weights

Star	type	300	428	1042	1493	2139	3423	7418	7424	7793
HR3611	B6V	0.0	0.0	0.0	0.0	0.0	0.0	0.0	0.0	0.32
HR3230	A1V	0.26	0.31	0.63	0.75	0.76	0.36	0.79	0.73	0.19
HR3473	A5V	0.12	0.0	0.0	0.0	0.0	0.0	0.0	0.0	0.0
HR3070	F1V	0.0	0.0	0.0	0.0	0.0	0.0	0.0	0.0	0.0
HR3378	G5III	0.0	0.0	0.0	0.0	0.0	0.0	0.0	0.0	0.0
HR1167	G8III	0.0	0.59	0.25	0.18	0.22	0.50	0.8	0.23	0.48
HR1216	K2III	0.61	0.09	0.12	0.07	0.02	0.13	0.13	0.4	0.01

Cols. (4) to (12) are labelled by NGC number and contain the relative weights of the template stars that contribute to the velocity dispersion fit, as determined by the fitting code.

mismatches. So we divide our sample in two bins, the "old" ($\gtrsim$ 1 Gyr) and the "young" ($<$ 1 Gyr) bin. The three clusters NGC300, NGC428 and NGC3423 are old and we therefore use the case 1 value because of the larger fitting region and thus better constrained fit. In the other 6 clusters, the young clusters, we prefer the case 2 values because they avoid the systematic uncertainties related with the Ca triplet. For all cases the velocity dispersion for case 1 is higher than for case 2. However the mean offset between case 1 and case 2 is 4.3 km s^{-1} in the old bin, but 11.6 km s^{-1} in the young bin, demonstrating the influence of age on the velocity dispersion as measured from the Ca triplet. Table 4.1 quotes the weights that the fitting code attributes to every single template star in its best fitting composite template. Note that the division in an old and a young bin is born out by the lower contribution of A stars to the three NCs NGC300, NGC428 and NGC3423. Table 4.2 contains only the finally adopted velocity dispersion. Formal random errors are available from χ^2 statistics. However, these do not include any systematic uncertainties and are therefore not particularly realistic. Useful error estimates are hard to obtain with all the complications from systematic effects just discussed. Typical systematic uncertainties from fitting different initial templates and different subsets of the available template set, are of the order of 15%. These are the errors we quote in Table 4.2.

The measured velocity dispersion is the luminosity weighted mean of the two components (disk and nuclear cluster) that contribute to the light inside the ground-based aperture. Section 4.3 details how we account for this in our dynamical modelling. Typical disk velocity dispersions are around 30 km s^{-1} for early type spirals (Bottema 1993). The Sm galaxy UGC4325 has a central disk velocity dispersion of 19$\pm$2km s^{-1} (Swaters 1999). Velocity dispersion of cluster and disk could therefore

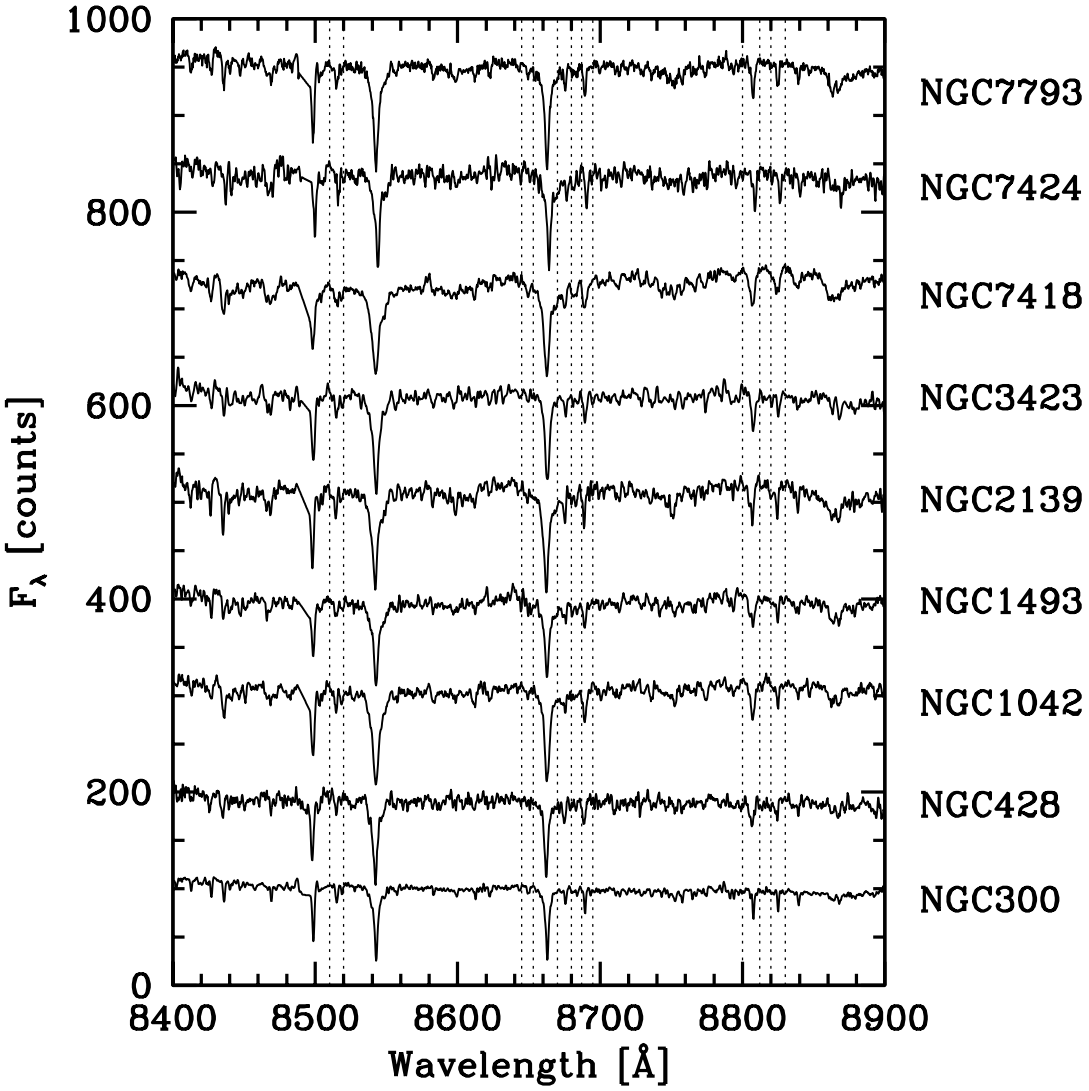

Figure 4.1: The region around the Calcium Triplet used for the velocity dispersion measurements. For better presentation, the spectra have been clipped to exclude residuals from sky lines and binned over three pixels. Fluxes have been arbitrarily adjusted to fit into the plot. Almost the full region was used for case 1 fitting, excluding only the region from 8470 to 8510 Å because of a CCD defect. The dotted lines bracket the six metal lines used for case 2 fitting.

be of comparable magnitude.

4.2 Surface brightness profiles

For the purposes of dynamical modeling we need PSF-deconvolved surface brightness profiles of the nuclear clusters and the surrounding galaxy disk. To this end we derive I-band surface brightness profiles from the HST/WFPC2 imaging data described in B02. Data reduction has been described there and will not be repeated here. While B02 inferred surface brightness profiles from their data, they did not perform PSF deconvolution. However accurate effective radii for most nuclear clusters in the B02 sample have been measured for most objects in our sample in B04. For their analysis, B04 used the software package `ISHAPE` (Larsen 1999) to fit PSF-convolved King or Moffat profiles with different concentration indices to the data. We here present a new analysis with the `galfit` routine (Peng et al. 2002). The reasons to repeat the excercise with a different software are twofold:

- Three out of the nine clusters in our present sample are placed in galaxy centers with irregular morphologies. As the fits from `ISHAPE` were therefore deemed unsatisfactory in B04, they were rejected at the time. A careful reexamination with `galfit` however yielded useful results at least for the purposes of our dynamical modeling.

- In B04 the main goal was to derive accurate effective radii for the clusters alone, implying the use of a single component for the cluster profile only. This one component then does not represent the light profile outside the cluster radius, called R_u in B04. However we here need the full deconvolved surface brightness profile, including the background galaxy, for the dynamical modeling. `Galfit` allows us to model the cluster and its surroundings with an unlimited number of different components, thereby optimizing the fit to the surface brightness profile at all radii.

In brief, `galfit` convolves a two-dimensional model which has a user-defined number of different analytic components (e.g. Sersic, Gaussian, exponential, constant background) with a user-supplied PSF, and finds the particular parameter set that best describes the observations. In most cases we use an exponential for the galaxy disk and a Sersic profile for the cluster. Very few complicated cases require more components. For example, the most complicated case is NGC2139, which needs five components to be fit well. That means a constant background, one exponential for the overall galaxy disk, one exponential component for the bar, one Sersic component for some extended emission around the cluster and one Sersic component for the cluster itself. Only one galaxy (NGC7418) shows evidence for

large amounts of dust. Only for this galaxy we therefore created a dust mask that was used to cover the region in the west of the nuclear cluster from the `galfit` fit. We use the same PSFs as in B04, constructed using the `Tiny Tim` software (Krist and Hook). Our dynamical modeling, described in Section 4.3, is based on the assumption of spherical symmetry. The calculations start from the projected surface brightness profile. For this purpose we use the best-fitting analytic `galfit` model for each galaxy to calculate the azimuthally averaged surface brightness profile. The averaging is done over circles that are centered on the component that we identify as the nuclear cluster. Figure 4.2 shows the derived "deconvolved" surface brightness profiles in comparison to the non-deconvolved ones from B02. While the general shape agrees well, all deconvolved profiles are more concentrated, as expected. Note also that the size of a pixel on the PC chip is $0.04555''$. The shape of the profile at smaller radii is therefore not well constrained.

Although the different components of the `galfit` fits were not chosen to have any physical meaning, it turns out that the least spatially extended component can be identified with the NC, except for one case (in NGC7418, the cluster is represented by an addition of one Sersic and one Gaussian profile with very similar effective radii). When comparing effective radii derived for the NCs under this identification with those determined with `ISHAPE`, we find that they agree well to about 30%. However strictly speaking the effective radii from `ISHAPE` are in general more reliable than the ones derived from the `galfit` models, because the extended wings of Sersic profiles may change the total luminosity content (and therefore the effective radius) of a model significantly with only small changes of the Sersic parameter n. In contrast King profiles do have a cutoff at large radius. B04 showed that the effective radius of the NCs is then well constrained, independent of uncertainties in their exact spatial profile.

4.3 Dynamical modelling

The luminosity L, effective radius r_e, and line-of-sight velocity dispersion $\sigma_{\rm obs}$ are known for each of the clusters in our sample. It follows from simple dimensional arguments that the cluster mass-to-light ratio M/L is given by

$$M/L = \alpha\, \sigma_{\rm obs}^2 r_e/GL, \tag{4.1}$$

where G is the gravitational constant. The dimensionless constant α is determined by the density and velocity distribution of the cluster, and by the spatial area incorporated in $\sigma_{\rm obs}$. If $\sigma_{\rm obs}$ corresponds to the mass-weighted average dispersion of the entire cluster, then generally α is of order ≈ 10 by virtue of the virial theorem. For example in this situation a spherical isotropic King (1962) model with concentration $c = 2$ has $\alpha = 9.77$. The value of α can be adjusted to account for the fact that

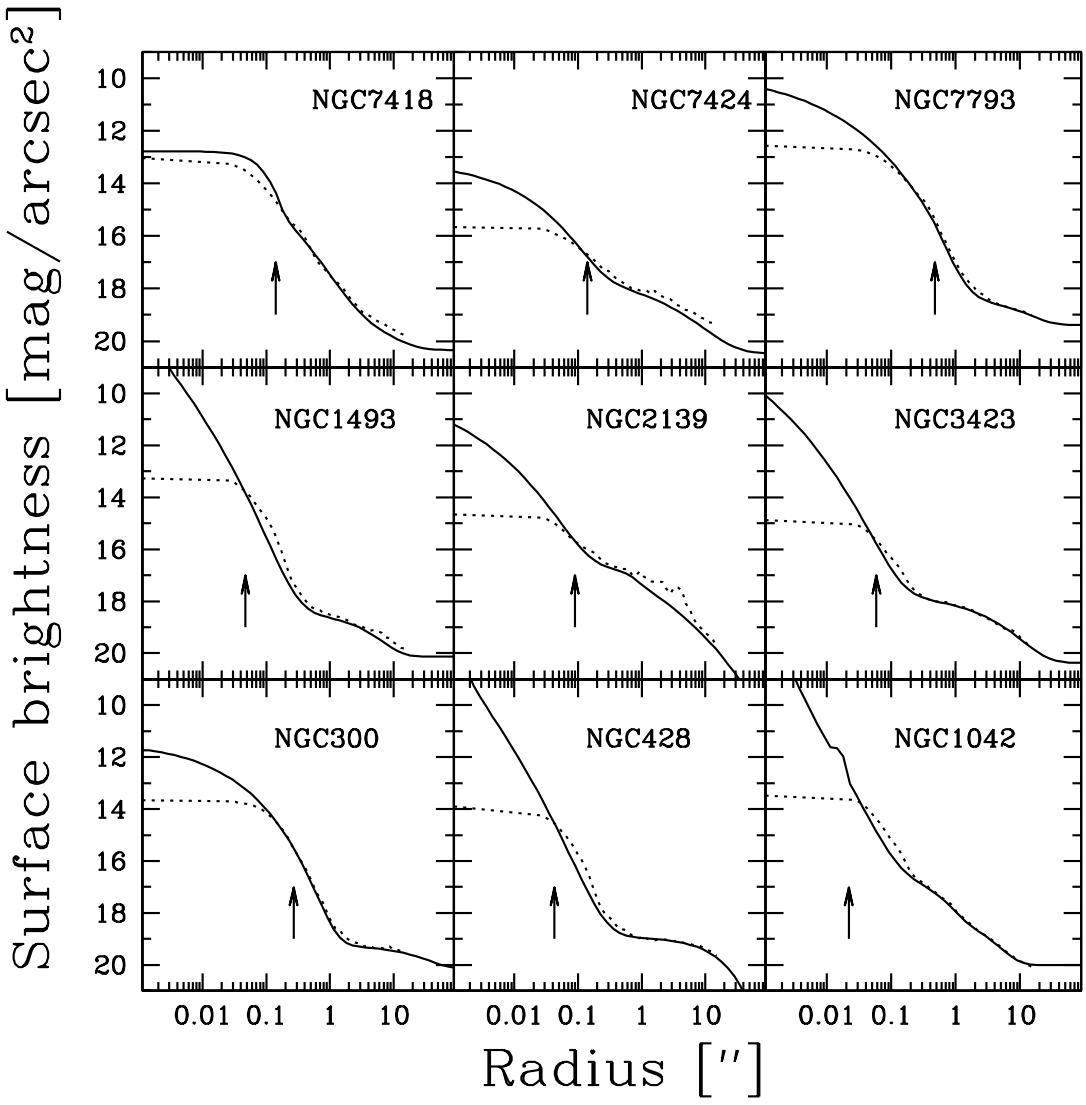

Figure 4.2: The I-band surface brightness profiles (i.e. deconvolved from the PSF) obtained for the combined nuclear clusters and stellar disks in our present sample with `galfit` (full line) compared with the non-deconvolved profiles obtained directly from the HST image (dotted line, from B02). The arrow corresponds to the effective radius of the star cluster. Note that the profile shapes agree reasonably well, but the deconvolved ones are always more concentrated towards the NC. Small differences between the profiles at large radii are due to differences in the methods used for model fitting and azimuthal averaging. These do not affect our dynamical modeling results.

not all of the cluster stars contributed to the observed spectrum, due to the finite slit width, extraction aperture size, and PSF FWHM of the observations. However, we are dealing with clusters that reside in galaxy centers, therefore application of equation (4.1) does not generally give accurate results. It ignores that some of the light in the observed spectrum actually came from stars in the disk, rather than in the cluster (see the contamination fractions in Table 3.1). Most importantly, equation (4.1) ignores the gravitational potential of the disk. This is important, as is most easily seen for stars in the outskirts of the cluster. For a model of a cluster in isolation (such as a King model) these stars would have a dispersion profile that falls to zero at some finite radius. However, in reality these stars will behave as test particles in the gravitational potential of the disk. Their dispersion will therefore not fall to zero, but will instead converge to the same dispersion that the disk stars have. As a result of this effect, equation (4.1) tends to overestimate the cluster M/L. In practice, we found for our sample that the results from equation (4.1) are in error by factors of up to 5. For accurate results it is therefore important to model the galaxies in more detail.

We adopt an approach based on the Jeans equation for a spherical system. The details of this approach are described in van der Marel (1994). We start with the deconvolved galaxy surface brightness profile, obtained with the `galfit` software as described in Section 4.2, to which we fit a smooth parameterized profile as in Geha, Guhathakurta & van der Marel (2002). This profile is then deprojected using an Abel integral under the assumption of spherical symmetry. With an assumed constant $M/L = 1$ (in solar units) this yields a trial three-dimensional mass density $\rho(r)$. Solution of Poisson's equation yields the gravitational potential $\Phi(r)$, and subsequent solution of the Jeans equation yields the three-dimensional velocity dispersion profile $\sigma(r)$. Luminosity-weighted projection along the line of sight gives the projected velocity dispersion profile $\sigma_{\rm p}(R)$. Convolution with the observational PSF and integration over pixels along the slit yields the predicted velocity dispersion profile along the slit. Upon modeling the extraction apertures and background subtraction procedures that were used for the actual observations, this yields the predicted dispersion $\sigma_{\rm pred}$. The trial mass-to-light ratio is then adjusted to $M/L = (\sigma_{\rm obs}/\sigma_{\rm pred})^2$ to bring the predictions into agreement with the observations. The fractional random error on the inferred M/L is twice the fractional random error on $\sigma_{\rm obs}$. The M/L values and their uncertainties thus obtained for all the sample NCs are listed in Table 4.2. The masses obtained by multiplication with the luminosities from B02 are also listed in the table. Errors on the masses include the errors on the luminosities as quoted in B02 and the error estimate on the velocity dispersion. In Section 4.1 we found that use of the Calcium Triplet lines for young clusters yields velocity dispersion values that are ≈ 10 km s^{-1} higher than the ones we have adopted. As explained there, we believe that the Calcium Triplet lines give biased results for young stellar populations. Nonetheless, if one were to adopt those results anyway, then this would

Table 4.2: Dynamical quantities

Galaxy (1)	σ [km s^{-1}] (2)	log(L$_I$) [L$_\odot$] (3)	M/L$_I^{dyn}$ (4)	log(M) [M$_\odot$] (5)
NGC 300	13.3 ± 2.0	6.21 ± 0.20	0.65 ± 0.20	6.02 ± 0.24
NGC 428	24.4 ± 3.7	6.89 ± 0.04	0.42 ± 0.13	6.51 ± 0.14
NGC 1042	32.0 ± 4.8	6.81 ± 0.16	0.50 ± 0.15	6.51 ± 0.21
NGC 1493	25.0 ± 3.8	6.89 ± 0.05	0.31 ± 0.09	6.38 ± 0.14
NGC 2139	16.5 ± 2.5	6.69 ± 0.16	0.17 ± 0.05	5.92 ± 0.20
NGC 3423	30.4 ± 4.6	6.37 ± 0.06	1.46 ± 0.44	6.53 ± 0.14
NGC 7418	34.1 ± 5.1	8.13 ± 0.13	0.45 ± 0.14	7.78 ± 0.19
NGC 7424	15.6 ± 2.3	6.20 ± 0.06	0.78 ± 0.23	6.09 ± 0.14
NGC 7793	24.6 ± 3.7	7.08 ± 0.05	0.64 ± 0.19	6.89 ± 0.14

Col. (1) Galaxy name. Col. (2) Measured velocity dispersion with systematic error. Col. (3) Logarithm of the I-band cluster luminosity in L$_\odot$ (from B02). The errors we use here are somewhat larger than quoted in B02 because they include the uncertainty of 0.1 mag due to difficulties in determining the outer radius of the cluster. Col. (4) and (5) M/L (in solar I-band units) and $\log(M) = \log(M/L * L)$ of the cluster as derived from the dynamical modeling.

translate into a factor of 2 increase in mass for a cluster with a velocity dispersion of 20 km s^{-1}.

Although our results are significantly more accurate than those obtained with equation (4.1), it should be kept in mind that there are some remaining uncertainties. First of all, each system is assumed to be spherical. This is probably quite accurate for the cluster, but much less so for the disk. However, this is a reasonable lowest order approximation given that our only application is to an extraction aperture on the center. Here there is zero net rotation, and the disk is generally not the dominant contributor to the observed light. Construction of fully axisymmetric models would be more accurate, but this is considerably more complicated and beyond the scope of the present thesis. A second caveat on the adopted approach is that we assume that the cluster and the disk have the same M/L. If in reality the components have different mass-to-light ratios then one would expect

$$(M/L)_{\rm inferred} \approx (1-f)(M/L)_{\rm cluster} + f(M/L)_{\rm disk}, \tag{4.2}$$

where f is the disk light contamination fraction listed in Table 3.1. We used the formalism described in Geha et al. (2002) to calculate several test models for one of the sample galaxies in which we assumed different values for $(M/L)_{\rm cluster}$ and $(M/L)_{\rm disk}$. The results confirm equation (4.2). So our inferred M/L values

are a weighted average of all the light in the extraction aperture. While for some galaxies this is almost exclusively light from the nuclear cluster, this is not true for all galaxies.

Interpretation of the results obtained in this chapter will be deferred to Chapter 6, where they will be discussed together with the age determinations obtained in the next chapter.

Chapter 5

Age analysis

> In which we study the wrinkles in the spectra of our sample clusters to determine their ages, metallicities, extinctions and the age of their last burst of star formation.

In the following we will apply three different methods to measure the ages of the spectra. This procedure will not only allow us to cross-check the methods against each other, but it will also yield the maximum amount of information available from the spectra and the current population synthesis models. Note that we will only talk about the spectra and not about the nuclear clusters themselves during this chapter. As has been shown in Table 3.1, the spectra do not only contain light from the nuclear clusters themselves, but some are heavily contaminated by disk light.

Design and use of population synthesis models exploit the fact that stellar populations with any star formation history can be expanded in series of instantaneous starbursts, conventionally named simple stellar population (SSP). The spectral energy distribution (SED) of such a single age burst population is the sum of the spectra of stars defining the isochrone of an SSP, weighted by the initial mass function (IMF). The location and form of the isochrone in the Hertzsprung-Russel diagram as well as the SEDs of each contributing star depend on the metallicity and the age. Good examples of coeval star cluster are e.g. globular clusters or very young star clusters. The SED of any stellar population at time t can then be written as

$$F_\lambda(t) = \int_0^t \Psi(t-t')S_\lambda[t, \zeta(t-t')]dt'. \tag{5.1}$$

Here, $\Psi(t-t')$ is the star formation rate over time, $\zeta(t-t')$ is the metal-enrichment law and $S_\lambda[t, \zeta(t-t')]$ is the power radiated per unit wavelength per unit initial mass by an SSP of age t' and metallicity $\zeta(t-t')$. It follows from this equation that by choosing suitably spaced SSPs covering a range of ages and metallicities, the problem of solving for the star formation history of a stellar system is equivalent to defining and minimizing the merit function

$$\chi^2 = \sum_{i=0}^{n} \left[\frac{F_i - \sum_{k=1}^{M} a_k S_i[t, Z]}{\sigma_i} \right]^2, \tag{5.2}$$

where F_i is the observed spectrum in each bin i, σ_i is its standard deviation and a_k are weights attributed to each SSP model $S_i[t, Z]$ of Age t and metallicity Z.

In theory the full SED contains all available constraints on all the different parameters of the system. We therefore use our velocity dispersion fitting code introduced in Chapter 2 to fit the whole observed SED with the stellar population models to derive ages, metallicities and extinctions for the spectra in our sample in Section 5.3. An alternative method is the use of spectral indices that are designed to compress the information available in the spectrum into a small set of numbers. Due to the nature of these indices, it is only possible to derive the mean luminosity weighted age of the spectra, i.e. their age under the assumption that they are single-age systems.

5.1 The population synthesis model

We use the population synthesis model presented by Bruzual and Charlot (2003). This model has a number of desirable features for the following analysis, which will be described very briefly. The model covers a wide wavelength range from 3200 to 9500 Å for a wide range of metallicities (from 0.0004 to 0.05, where 0.02 is solar). In the following only metallicities from 0.004 to 0.05 are used as lower metallicities are not well sampled by the empirical stellar library used for predicting SEDs (STELIB Le Borgne et al., 2003). As the observed spectra reach from 3600 to 9900 Å (albeit with a gap from 4800 to 6150 Å) such a large wavelength coverage is desirable. The model SEDs cover an age range from 10^5 to 2×10^{10} years. Model uncertainties become large for ages younger than 10^6 years and we will therefore restrain the used age range to SED ages larger than 1 Myr. Star formation timecales are of the order of 10^6 years, the assumption that all stars are on

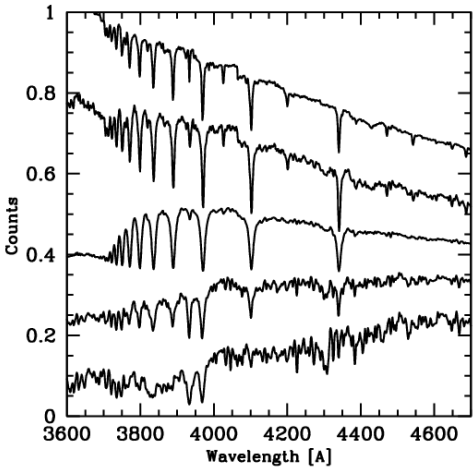

Figure 5.1: Example spectra from the population synthesis models by Bruzual and Charlot (2003). The models have solar metallicity and ages of 1, 10, 100, 1000, 10000 Myr from top to bottom.

the zero-age main sequence might therefore not be justified. Further such very young stellar populations can be expected to be still embedded in the original gas cloud from which they formed and thus to be heavily reddened. The SEDs have a resolution of $\lambda/\Delta\lambda = 2000$ (3 Å FWHM) across the whole wavelength range. This is as close as it gets to the resolution of our data. [1]

The initial mass function is a free parameter of the model and we follow Bruzual and Charlot (2003) in choosing a Chabrier (2003) IMF. The SED of each model SSP is normalized to an initial total mass in stars of 1 $M_\odot$. Thus a 10 Gyr old SSP will represent only about 0.5 $M_\odot$ in stars, as the rest of the initial mass is lost through stellar winds and explosions.

5.2 Ages from spectral indices

Ages and metallicities of stellar populations can be determined from stellar population models using what is known as the Lick/IDS system (Worthey, 1994; Worthey and Ottaviani, 1997; Trager et al., 1998). In this method, the stellar population models are used to predict the values of a set of absorption feature indices for different values of the input parameters metallicity ([Fe/H]), single-burst age, and initial mass function (IMF) exponent. More recently Thomas et al. (2003) also introduced the abundance ratio of the so-called α elements (N, O, Mg, Ca, Na, Ne, S, Si, Ti) to the Fe-peak elements (Cr, Mn, Fe, Co, Ni, Cu, Zn) as an additional parameter. Although the strength of each index depends on all input parameters, one is mainly interested in indices that are sensitive mostly to only one parameter, as e.g. the Hβ index, which depends mostly on age. After measuring the same indices in the observed spectra of globular clusters or galaxies, best fitting ages and metallicities can be derived. For the population synthesis models of Bruzual and Charlot (2003) a set of 31 spectral indices is available in tabulated form.

For the present work, several problems with this system of indices occur. First, most of the indices lie in spectral regions not covered by our data. Among them are the strongest age indicator, namely the Hβ index at 4861 Å, and most of the Fe indices (Fe5270, Fe5335, Fe5406, Fe5709 and Fe5782). Second, emission lines are present in the spectra that partially fill up the Balmer absorption troughs and thus bias age measurements to higher ages. Third the index libraries have been designed mostly for populations older than 1 Gyr. Especially the metallicity of young populations is not well constrained by most of the indices. To illustrate this statement, Figure 5.2 shows all the indices that we will measure in our data as a function of metallicity and age. Although in our wavelength range, the CN and

[1] Only one model has become available very recently that has a higher resolution of 10000 (Le Borgne et al., 2004), however the SEDs cover a somewhat smaller wavelength range (4000 to 6800 Å) and do not predict SEDs for ages younger than 10^7 years.

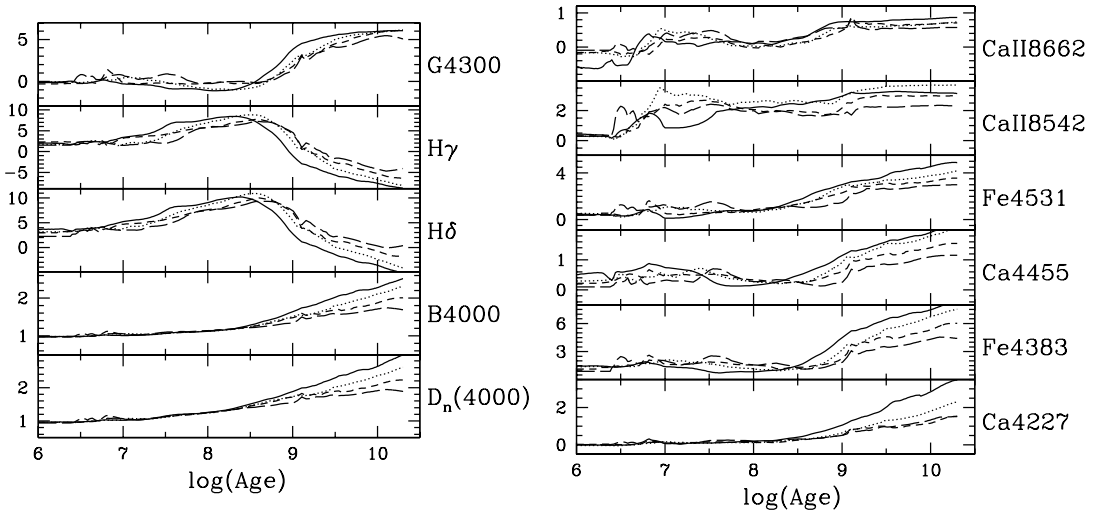

Figure 5.2: The dependence on age of different spectral indices measurable in the UVES data as predicted from the Bruzual and Charlot (2003) models. The different lines correspond to different metallicities (solid Z=0.05, dotted Z=0.02, short dash Z=0.008, long dash Z=0.004). Note that the left five indices are good age indicators for ages older than $10^{7.5}$ years. The six indices on the right are more sensitive to metallicity, again in particular at old ages.

Mg indices will not be considered here as they fall into the family of α-element-like indices (as found by Trager et al., 1998) and are thus not a good measure of metallicity as defined by the [Fe/H] ratio. We also do not use the third Ca index at 8498 Å because of a CCD defect in this region of the spectrum.

Indices are measured as follows, following the procedures outlined in Worthey (1994): Two pseudocontinuum bandpasses are defined on either side of a central bandpass (compare Table 5.1). A line representing the continuum is then drawn between the midpoints of the flanking bandpasses, and the flux difference between this line and the central bandpass flux is integrated and then determines the index. Indices are measured in equivalent width. More explicitly, the average bandpass flux from the spectrum is:

$$F_r = \int_{\lambda_1}^{\lambda_2} \frac{F_\lambda}{(\lambda_1 - \lambda_2)} d\lambda \tag{5.3}$$

The local continuum $F_{C\lambda}$ for the index is then the run of flux defined by drawing a straight line from the midpoint of the blue continuum level to the midpoint of the red continuum level.

An equivalent width is then

$$\mathrm{EW} = \int_{\lambda_1}^{\lambda_2} \left(1 - \frac{F_{I\lambda}}{F_{C\lambda}}\right) d\lambda, \tag{5.4}$$

where $F_{I\lambda}$ and $F_{C\lambda}$ are the fluxes per unit wavelength in the index bandpass and the straight line continuum flux in the index bandpass, respectively. $D_n(4000)$ and B4000 are defined as ratios of the two different bandpasses and not as equivalent widths. For the indices we measure in this work, the bandpasses and pseudo-continuum bands are listed in Table 5.1.

The measured indices for our nine objects are tabulated in Table 5.2. The spectra have been degraded to the resolution of the models by convolving them with a Gaussian of 3 Å FWHM and then rebinning them to the 1 Å pixel size. The error vectors have been first squared (without prior convolution), then rebinned to the same pixel size of 1 Å before taking the square root again. Although after convolution the measurement of each single pixel in the object spectrum is not independent anymore, errors should have stayed realistic. We have verified that the rebinning process changes the index values only slightly, i.e. less than the statistical 1 σ error. This is negligible for our interpretation. Three of the spectra (NGC1042, NGC7418, NGC7424) have prominent Balmer emission lines. These have been subtracted by interpolating the absorption line as exemplified in Figure 5.3. Our goal is to compare the age determinations from the Lick indices with the direct fitting method introduced below. Therefore emission line removal based on the fit of the Bruzual and Charlot (2003) models, though possible, would have led to circular reasoning and was not applied. To allow for an assessment of the magnitude of the effect of removing the emission lines, we also quote the index values derived from the non-interpolated spectra in Table 5.2. This non-sophisticated procedure of emission line removal underestimates the equivalent width of the absorption lines. To derive the errors we use the measured noise vectors to generate 300 representations of the observed spectra. The errors are taken to be Gaussian on each pixel, with a 1σ error as given by the error vector. We then measure the indices on each of these representations and determine the final error on

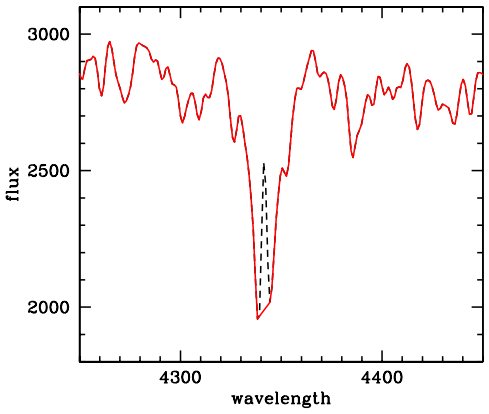

Figure 5.3: Emission line removal by interpolation. Solid line: fudged spectrum, dashed line: measured spectrum with emission line.

Table 5.1: Index bandpasses

Index	Index bandpass	pseudocontinua	reference
$D_n(4000)$		3750 - 3950	3
		4050 - 4250	
B4000		3850 - 3950	4
		4000 - 4100	
Hδ	4083.500 - 4122.250	4041.600 - 4079.750	1
		4128.500 - 4161.000	
Ca4227	4222.250 - 4234.750	4211.000 - 4219.750	1
		4241.000 - 4251.000	
G4300	4281.375 - 4316.375	4266.375 - 4282.625	1
		4318.875 - 4335.125	
Hγ	4319.750 - 4363.500	4283.500 - 4319.750	1
		4367.250 - 4419.750	
Fe4383	4369.125 - 4420.375	4359.125 - 4370.375	1
		4442.875 - 4455.375	
Ca4455	4452.125 - 4474.625	4445.875 - 4454.625	1
		4477.125 - 4492.125	
Fe4531	4514.250 - 4559.250	4504.250 - 4514.250	1
		4560.500 - 4579.250	
CaII8542	8527.000 - 8557.000	8447.500 - 8462.500	2
		8842.500 - 8857.500	
CaII8662	8647.000 - 8677.000	8447.500 - 8462.500	2
		8842.500 - 8857.500	

References: 1 Trager et al. (1998), 2 Diaz et al. (1989), 3 Balogh et al. (1999) 4 Gorgas et al. (1999)

the index as the root mean square:

$$\mathrm{rms} = \sqrt{\frac{\sum_1^{300}(I_i - I_o)^2}{300}}, \tag{5.5}$$

where I_o is the index as measured in the original spectrum and I_i are the indices as measured on the 300 random representations.

Figures 5.6 and 5.4 should allow to gain a feeling of how good the measured index values can be reproduced by the models. The four graphs in Figure 5.4 show four different combinations of the measured indices. The upper left graph in Figure 5.4 shows two age indicators, namely the $D_n(4000)$ index against the Hδ index. Both age indicators do not seem to agree well. One likely reason for the disagreement

Table 5.2: Measured indices

NGC No.	0300	0428	1042
$D_n(4000)$	1.5335 ± 0.0045	1.8488 ± 0.0270	1.4076 ± 0.0079
B4000	1.3686 ± 0.0055	1.5655 ± 0.0318	1.2673 ± 0.0098
Hδ	4.3741 ± 0.1747	2.6902 ± 0.7666	3.5529 ± 0.3293
Ca4227	0.6177 ± 0.0968	0.1944 ± 0.3745	0.7833 ± 0.1749
G4300	2.4635 ± 0.1744	1.5820 ± 0.7151	2.2495 ± 0.3542
Hγ	1.1035 ± 0.1804	-0.0613 ± 0.6904	-0.0667 ± 0.3397
Fe4383	2.0037 ± 0.2226	1.5828 ± 0.9005	3.1668 ± 0.4687
Ca4455	0.9794 ± 0.1106	0.0178 ± 0.4445	1.1794 ± 0.2273
Fe4531	2.2719 ± 0.2011	2.2142 ± 0.7114	2.5028 ± 0.4010
CaII8542	2.8548 ± 0.1397	1.8867 ± 0.2528	3.7021 ± 0.1293
CaII8662	2.3566 ± 0.1397	2.3220 ± 0.2530	3.3519 ± 0.1292

NGC No.	1493	2139	3423
$D_n(4000)$	1.2307 ± 0.0018	1.0424 ± 0.0045	1.6320 ± 0.0051
B4000	1.1298 ± 0.0023	1.0114 ± 0.0062	1.4826 ± 0.0060
Hδ	5.8382 ± 0.0893	5.3124 ± 0.2828	1.9221 ± 0.1896
Ca4227	0.2037 ± 0.0504	0.0501 ± 0.1736	1.4469 ± 0.0889
G4300	0.0869 ± 0.1066	0.1426 ± 0.3605	3.7313 ± 0.17981
Hγ	3.9740 ± 0.0965	4.7860 ± 0.3411	-2.2092 ± 0.1953
Fe4383	0.3366 ± 0.1453	1.0242 ± 0.5251	4.5396 ± 0.2283
Ca4455	0.2397 ± 0.0707	1.4273 ± 0.2613	1.8277 ± 0.1109
Fe4531	1.3538 ± 0.1254	0.4998 ± 0.5133	2.5427 ± 0.1997
CaII8542	2.9145 ± 0.1871	2.5466 ± 0.1294	3.0602 ± 0.2100
CaII8662	3.1098 ± 0.1870	2.7803 ± 0.1297	2.1950 ± 0.2101

NGC No.	7418	7424	7793
$D_n(4000)$	1.3168 ± 0.0046	1.2227 ± 0.0053	1.3168 ± 0.0046
B4000	1.1570 ± 0.0056	1.1120 ± 0.0066	1.1823 ± 0.0010
Hδ	4.7034 ± 0.2358	6.4383 ± 0.2631	7.2915 ± 0.0336
Ca4227	0.3372 ± 0.1242	0.3677 ± 0.1441	0.4456 ± 0.0199
G4300	-0.0042 ± 0.2628	-0.3344 ± 0.3174	0.2253 ± 0.0421
Hγ	2.6294 ± 0.2441	4.5771 ± 0.2895	4.8789 ± 0.0373
Fe4383	1.7153 ± 0.3514	1.4080 ± 0.4329	1.0043 ± 0.0573
Ca4455	1.0912 ± 0.1661	1.0495 ± 0.2108	0.5170 ± 0.0280
Fe4531	0.7925 ± 0.2981	1.1275 ± 0.3978	1.4582 ± 0.0498
CaII8542	3.0666 ± 0.0974	2.3939 ± 0.2174	3.4344 ± 0.0901
CaII8662	3.1150 ± 0.0974	2.4328 ± 0.2176	3.3382 ± 0.0902

Note: The following values are obtained for the Balmer indices if no interpolation of the emission lines is performed.
NGC1042: Hδ = 3.3190 ± 0.3300, Hγ = -0.8815 ± 0.3666
NGC7418: Hδ = 4.4261 ± 0.2363, Hγ = 1.4905 ± 0.2466
NGC7424: Hδ = 6.3427 ± 0.2633, Hγ = 4.0523 ± 0.2909

between data and model is the fact that, as we will show in Section 5.5, the spectra are not well represented by a single-age population. Such a behaviour has been studied quantitatively by Kauffmann et al. (2003) for the combination of indices $D_n(4000)$ versus Hδ. These authors carry out large sets of simulations showing the locus of galaxies with different star formation history in this plane. They find that continuous star formation histories occupy a narrow band in the $D_n(4000)$-Hδ plane, more or less at the same locus where our measurements fall too. Galaxies with stronger Hδ absorption strength at a given value of $D_n(4000)$ must have formed a significant fraction of their stars in a recent burst. Consider for another example the lower right panel of Figure 5.4. Adding two bursts of star formation of different ages will actually yield measured index values that are some average of the index values of the individual age components, thereby shifting the points around in the plot. At a constant value of H$\gamma = 4$, the Fe4531 index has two possible values. If two bursts with the right ages are mixed, the Fe4531 will lie in the region between the curves, exactly as is seen for three of the points in the graph.

The two metallicity indicators shown in the upper right graph in Figure 5.4 agree reasonably well with each other and the models. This is not the case for the Ca indices however, as seen from Figure 5.6. The measured index values for CaII8662 are never matched by the models. This undermines the trust in the other Ca-triplet index CaII8542 as well. The index Ca4455 value would lead to widely different ages than the other indices in several cases (e.g. NGC3432) and therefore does not seem to be a useful abundance indicator (compare also Thomas et al., 2003). It is possible, that the use of models with different [α/Fe] ratios would lead to an improved fit, as a increase of the [α/Fe] ratio by 0.3 dex could lead to an increase of the index strength by 0.5.

Figure 5.4 also shows two different combinations of indices potentially able to allow simultaneous measurement of age and metallicity. Unfortunately, the $D_n(4000)$ and B(4000) index depend on metallicity in the same way as do the well-reproduced indices Fe4383 and Fe4531. This combination, shown in the lower left graph is therefore not very well suited to determine both of these quantities. The combination of the Fe4531 index with the Hγ index, shown in the lower right, is in fact the only one, where none of the measured index values disagrees totally with the models. In summary, Figure 5.4 shows that the measured indices are not very well reproduced by the population synthesis models, which is probably due to mixed stellar populations in the spectra.

Despite the significant mismatch between the models and the data, it remains interesting to use the indices to compute the best fit value for the age and the metallicity of the spiral nuclei. We have detailed above, why the indices CaII8662, CaII8542 and Ca4455 seem to be of little use. The D_n4000 index is drawn from the same spectral region as the B(4000) index, these two measurements are therefore not statistically independent. The Fe4383 index is very similar to Fe4531, however

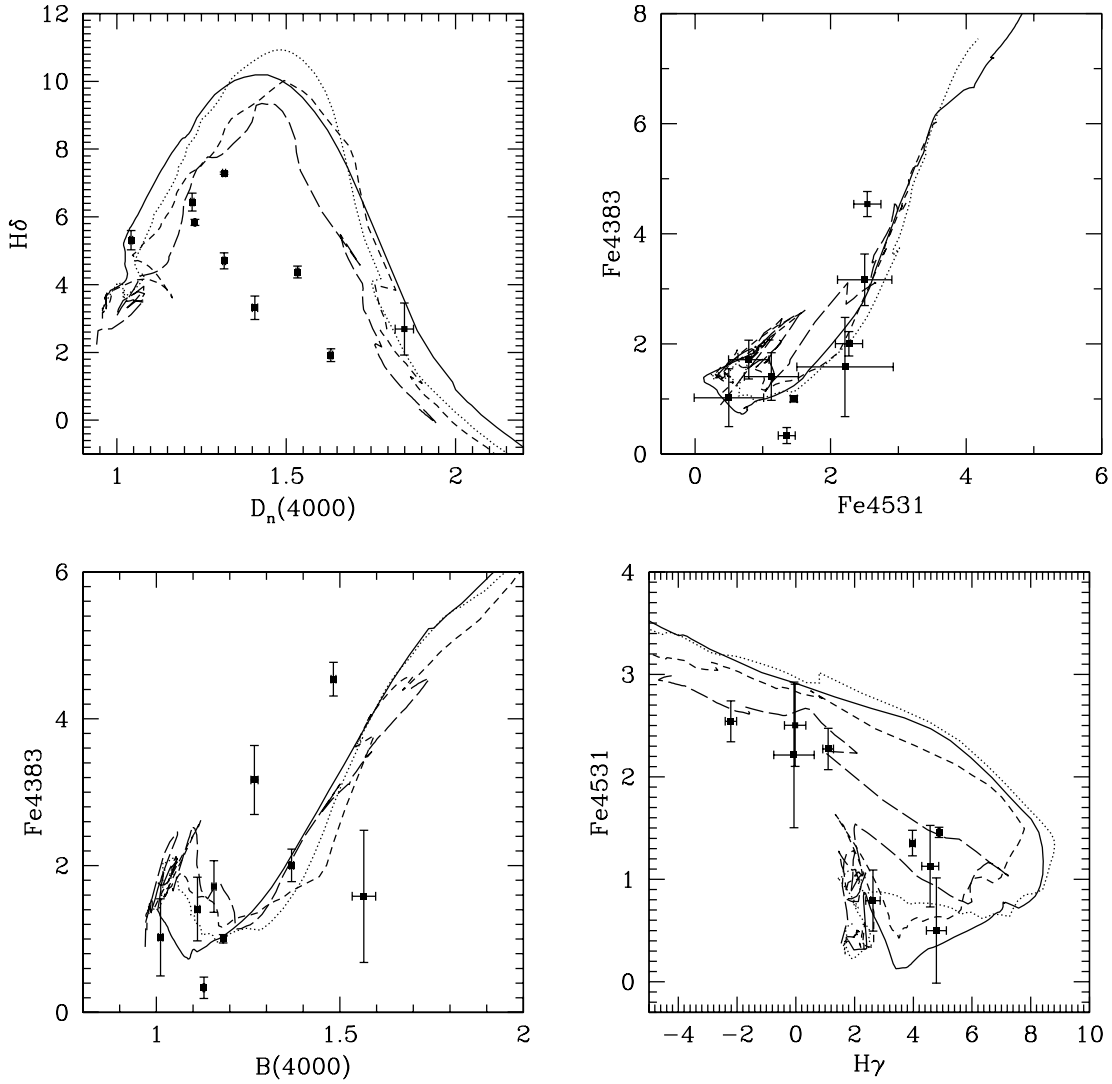

Figure 5.4: Index values as measured for the nine spectra compared to the predictions made by the population synthesis models. Again the different lines correspond to different metallicities (solid Z=0.05, dotted Z=0.02, short dash Z=0.008, long dash Z=0.004). In the upper left are two age sensitive indices, in the upper right two metallicity sensitive indices. The lower graphs show two combinations potentially able to disentangle age and metallicity. Note that the measured indices are not well predicted by the models which can be explained at least partially if the spectra do not represent single-age populations.

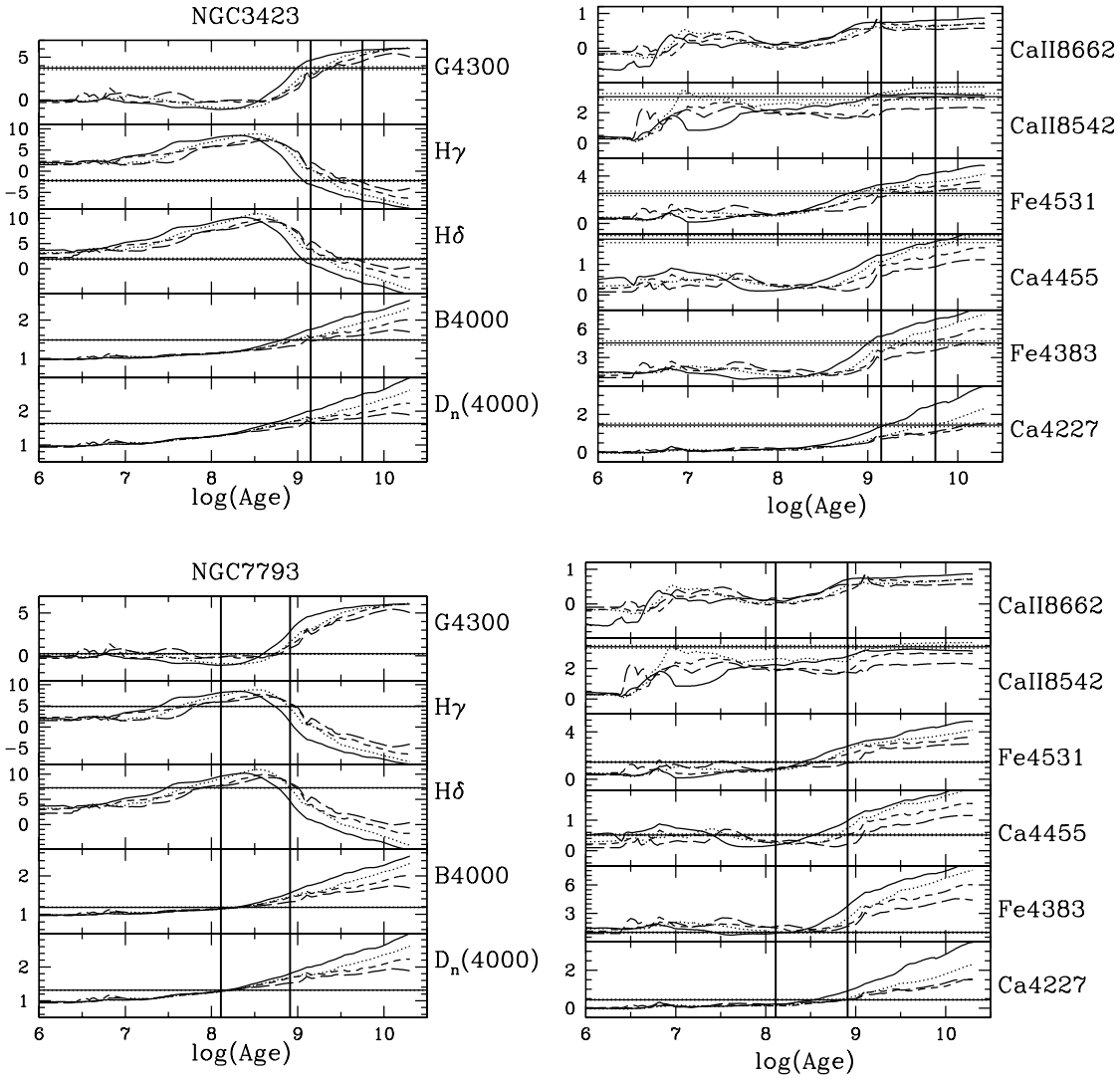

Figure 5.5: Figure 5.6 continues next page

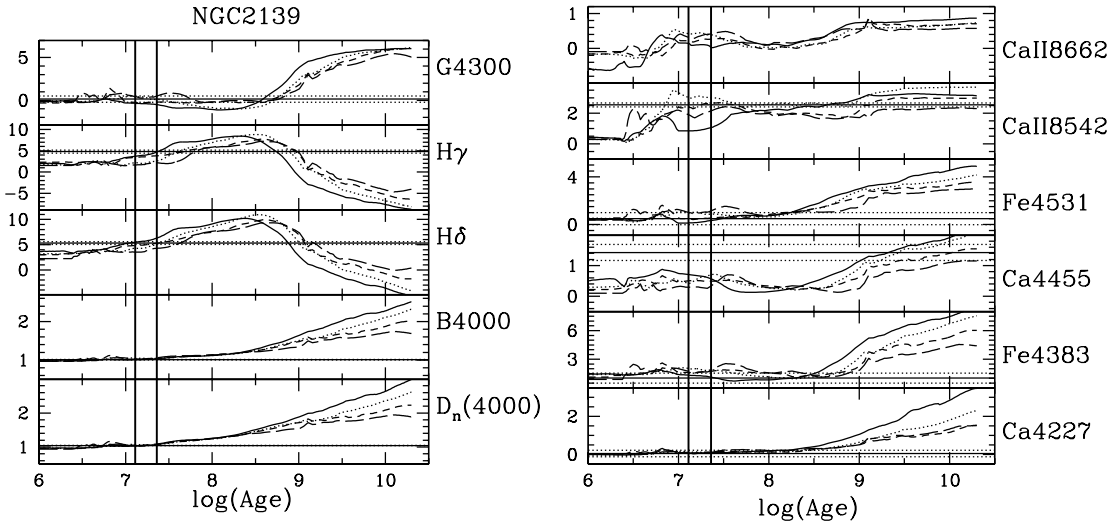

Figure 5.6: Index values as measured for three objects compared to the predictions made by the population synthesis models for all the indices. Again the different lines correspond to different metallicities (solid Z=0.05, dotted Z=0.02, short dash Z=0.008, long dash Z=0.004). Note that the Ca4455 index as well as the near-infrared index CaII8662 always fail to match.

seems to depend somewhat more on the [α/Fe] ratio (Thomas et al., 2003). The Hδ index is very similar to Hγ, however the Hγ absorption line is deeper and therefore the index should be better defined. The G4300 index has no age dependency at ages smaller than $10^{8.5}$ years, where most of our objects lie. Leaving aside all these problematic cases, we are left with the following four indices: B(4000), Hγ, Fe4531 and Ca4227. We compute the χ^2 plane spanned by the two parameters age and metallicity for all nine spectra in our sample. More explicitly, we compute the following quantity:

$$\chi^2 = \sum_1^4 \frac{(I_{meas} - I_{pred})^2}{(\Delta I_{meas})^2}. \tag{5.6}$$

Here I_{meas} is the measured value of the index with standard deviation ΔI_{meas} and I_{pred} is the value of the index as tabulated. We sample every combination of age and metallicity available in the model, i.e. 4 metallicities and 220 ages ranging from 10^6 to 2×10^10 years. The age spacing is very roughly logarithmic in time. The resulting best fit χ^2 values are quoted in Table 5.3. The expected value for χ^2 is 2 (i.e. the number of degrees of freedom minus the number of free parameters). The huge χ^2 values in Table 5.3 are just another indication of the mismatch between the models

and the data. To derive any error estimate at all, we have nonetheless rescaled the resulting χ^2 to the expected value. For a two parameter space, the 68.3%, 90% and 99% confidence intervals are then given by iso-$\Delta\chi^2$ contours of 2.30, 4.61 and 9.21, respectively (Press et al., 1992, Chapter 15.6). These are shown in Figure 5.7. The width and form of the 68.3% region is intended to give a feeling for how well age and metallicity parameters are constrained. For the ages, Table 5.3 quotes the best fit value along with its 68.3% confidence region. For the metallicities the range encompassing the 68.3% confidence region is given. The age and metallicity of NGC1042 is very poorly constrained by this type of fit. However, given that we found above that the objects are not well represented by the model indices, one should not overinterpret any of these contours. Note however that the two objects with the lowest χ^2 in Table 5.3, i.e. with the best quality of the fit, also have the best defined resulting age and metallicity.

Table 5.3: Ages and metallicities from absorption indices

Galaxy	χ^2	log(Age)	Metallicity
NGC 300	154	$9.11^{+0.1}_{-0.0}$	0.004
NGC 428	4.2	$9.36^{+0.08}_{-0.26}$	0.004 - 0.02
NGC1042	225	8^{+1}_{-1}	0.004 - 0.05
NGC1493	69	$7.74^{+0.11}_{-0.05}$	0.004
NGC2139	6	$7.30^{+0.06}_{-0.19}$	0.05
NGC3423	194	$9.39^{+0.36}_{-0.24}$	0.004 - 0.02
NGC7418	75	$7.70^{+0.16}_{-0.21}$	0.004
NGC7424	1.8	$7.81^{+0.05}_{-0.05}$	0.004
NGC7793	1417	$8.26^{+0.65}_{-0.15}$	0.004 - 0.008

Note: NGC7418 has two minima that are equally good fits. The age quoted here is chosen to agree roughly with the age that will be determined later by the spectral fitting.

5.3 Fitting Simple Stellar Populations

We now use the full blue SED from 3600 to 4700 Å to derive the best fit SSP in a χ^2 sense for each of the spectra. This means that we simply calculate

$$\chi^2 = \sum_n \left[\frac{t(n) - g(n)}{\sigma(n)} \right]^2 \tag{5.7}$$

where $g(n)$ is the observed SED, $\sigma(n)$ is the standard deviation on each bin in the SED and $t(n)$ is the SSP SED. We sample the full available parameter space of

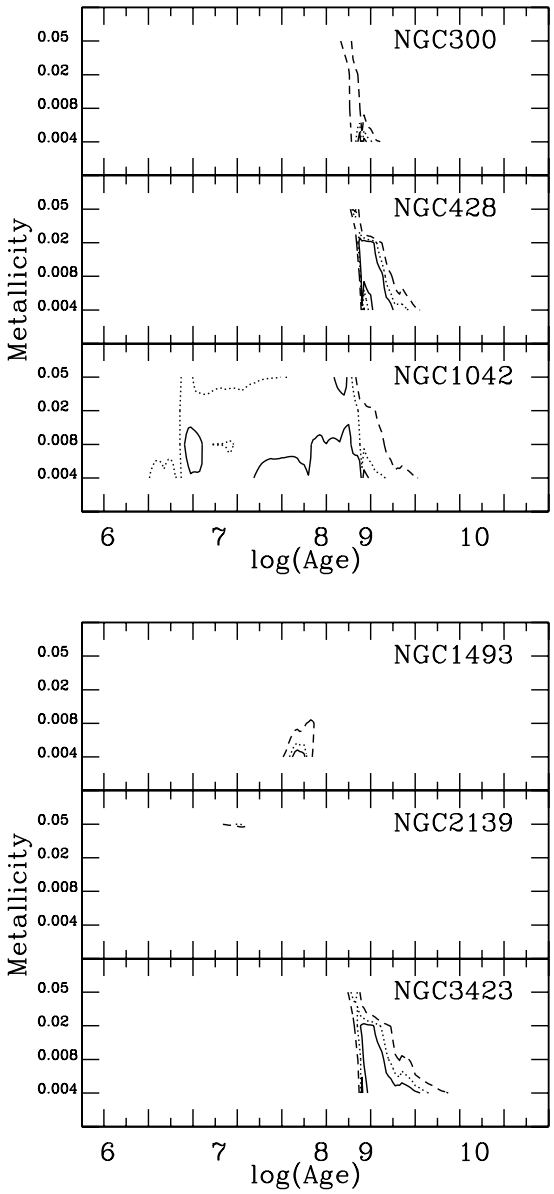

Figure 5.7: The χ^2 planes as derived from four spectral indices for all the nine spectra. Solid, dotted and dashed lines are 68.3%, 90% and 99% confidence regions, respectively. The size of these χ^2 contours is probably mostly determined by how well or how bad the indices measured in the object spectra can be reproduced by the models.

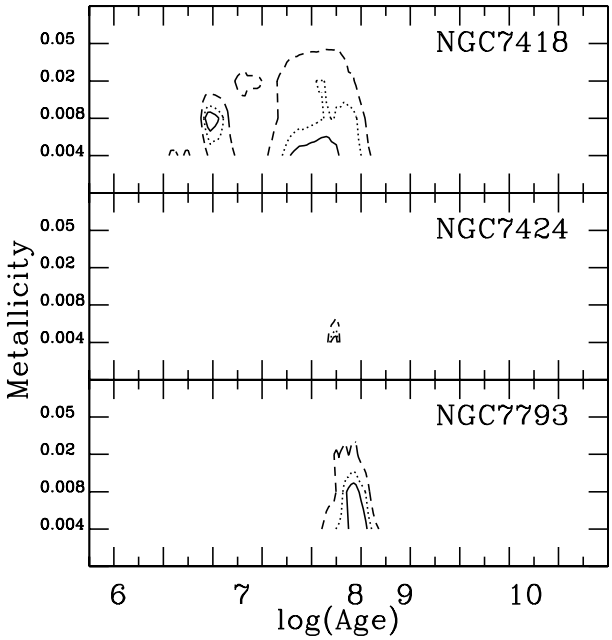

Figure 5.7 – *continued*

age and metallicity. The available metallicities are Z=0.004, 0.008, 0.02, 0.05, where Z=0.02 is solar. We have chosen 14 SSPs, logarithmically spaced in age, i.e. 1, 3, 6, 10, 30, ..., 10000, 20000 Myrs. It will be shown later on that this corresponds to the age resolution we can actually achieve. We additionally introduce an extinction parameter A_I which we sample in steps of 0.1 mag (for comparison: the foreground Galactic extinction is of the order $A_I = 0.1$). The chosen effective wavelength is 8000 Å, therefore similar to the I-band.

We use the `losvdfit` code introduced in Chapter 2. Although it was originally designed to be used for kinematic studies, certain aspects of this code make it a useful tool for population synthesis. First it adjusts automatically for any velocity shift between templates and objects. As the spectral resolution of the model SSPs is much lower than that of the spectra, the code correctly finds a very low velocity dispersion, typically of order 10 km s^{-1} in each fit. Second, `losvdfit` also allows for a convenient way to mask emission lines from the finally derived χ^2. We are thus able to minimize the influence of the Balmer emission lines on the derived age, in stark contrast to methods based on the Lick indices. Emission lines were located by eye. Masks were then constructed specifically for every observed spectrum and applied. At this stage we do not allow for template superposition, i.e. we only fit one SSP with fixed age and metallicity to the object spectrum. Note that no continuum

Table 5.4: Ages and metallicities from fitting SSPs

Galaxy	χ^2	log(Age)	Z	A_I	M/L
NGC 300	2491	9±0.3	0.02	0.0	0.41
NGC 428	340	9±0.3	0.05	0.3	0.41
NGC1042	669	9±0.3	0.004	0.0	0.41
NGC1493	2775	7.48±0.3	0.008	0.6	0.07
NGC2139	484	6.78±0.3	0.004	0.0	0.02
NGC3423	4436	9.48±0.3	0.004	0.0	0.87
NGC7418	319	7.78±0.3	0.004	0.6	0.10
NGC7424	264	7.78±0.3	0.004	0.2	0.10
NGC7793	14759	8±0.3	0.008	0.3	0.15

component is subtracted, as the spectra are reasonably well flux calibrated and the continuum shape therefore provides an additional constraint on the age.

Table 5.4 lists the best fitting ages, metallicities and extinctions as well as the χ^2 value for the best fit. Taking into account the number of pixels used in the fit and the number of free parameters, the expected value for χ^2 is ≈4200. In contrast to what we find for the index method, χ^2 is almost always lower than the expected value, which possibly indicates that the errors on the spectra are overestimated by the UVES reduction pipeline. Due to the 3-dimensional nature of the parameter space under consideration, graphical representation of the results is difficult. We choose to display the full χ^2 parameter space for two example spectra in Figures 5.8 and 5.9. The examples we choose are again NGC7793 because it has the highest S/N ratio of all observed spectra and NGC300 because it is older than 1 Gyr in contrast to NGC7793. It is comforting to note that the best fitting age does not depend very much on either metallicity or extinction. The best fit age does not change by more than 0.3 dex for a reasonable range of these two parameters. The same is true for the other 7 spectra that are not shown here. To avoid the artificial rescaling of the χ^2 value to the expected value as done for the Lick index method in Section 5.2, we therefore quote 0.3 dex as a conservative error estimate on the derived age in Table 5.4. Note that this justifies in retrospect our choice of age intervals for the SSP templates. Metallicity in itself seems to be a well-defined quantity as well, as its best fit value changes only for extinction values very far from the best fit value. We therefore do not quote any error on Z. Formal errors on the extinction are probably much lower than the chosen step size of 0.1 mag. From rescaling χ^2 to the expected value, the iso-$\Delta\chi^2$ contour of 11.3, which corresponds to the 99% confidence interval in three parameters, is always smaller than or comparable to this step size. It should be kept in mind here that we will show in Section 5.5 that the

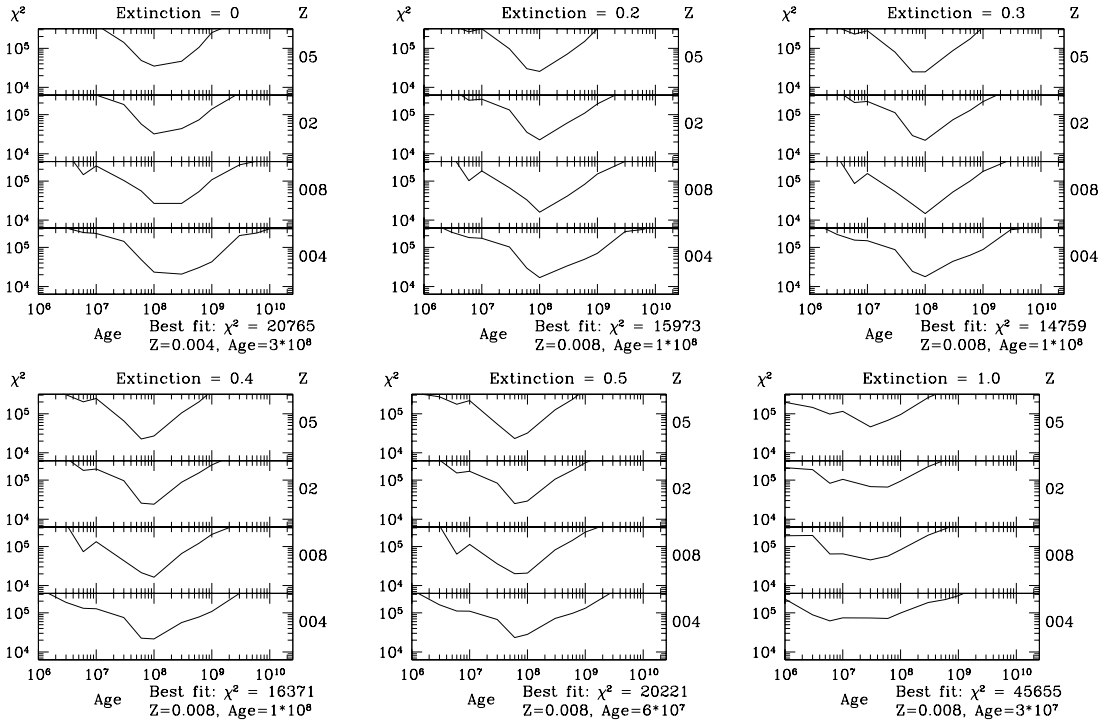

Figure 5.8: Three dimensional χ^2 space in the three parameters age, metallicity Z and Extinction A_I for the nuclear spectrum in NGC7793. Note that the best fit age is almost independent of the chosen metallicity and extinction.

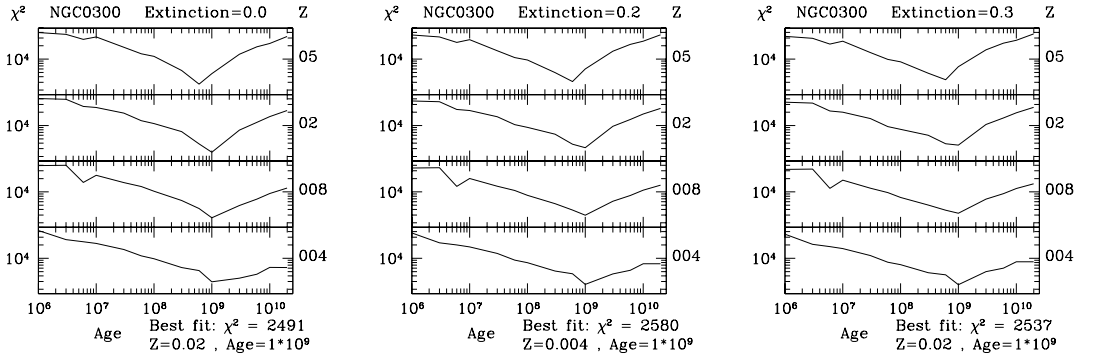

Figure 5.9: Three dimensional χ^2 space in the three parameters age, metallicity Z and Extinction A_I for the nuclear spectrum in NGC300.Note that the best fit age is almost independent of the chosen metallicity and extinction.

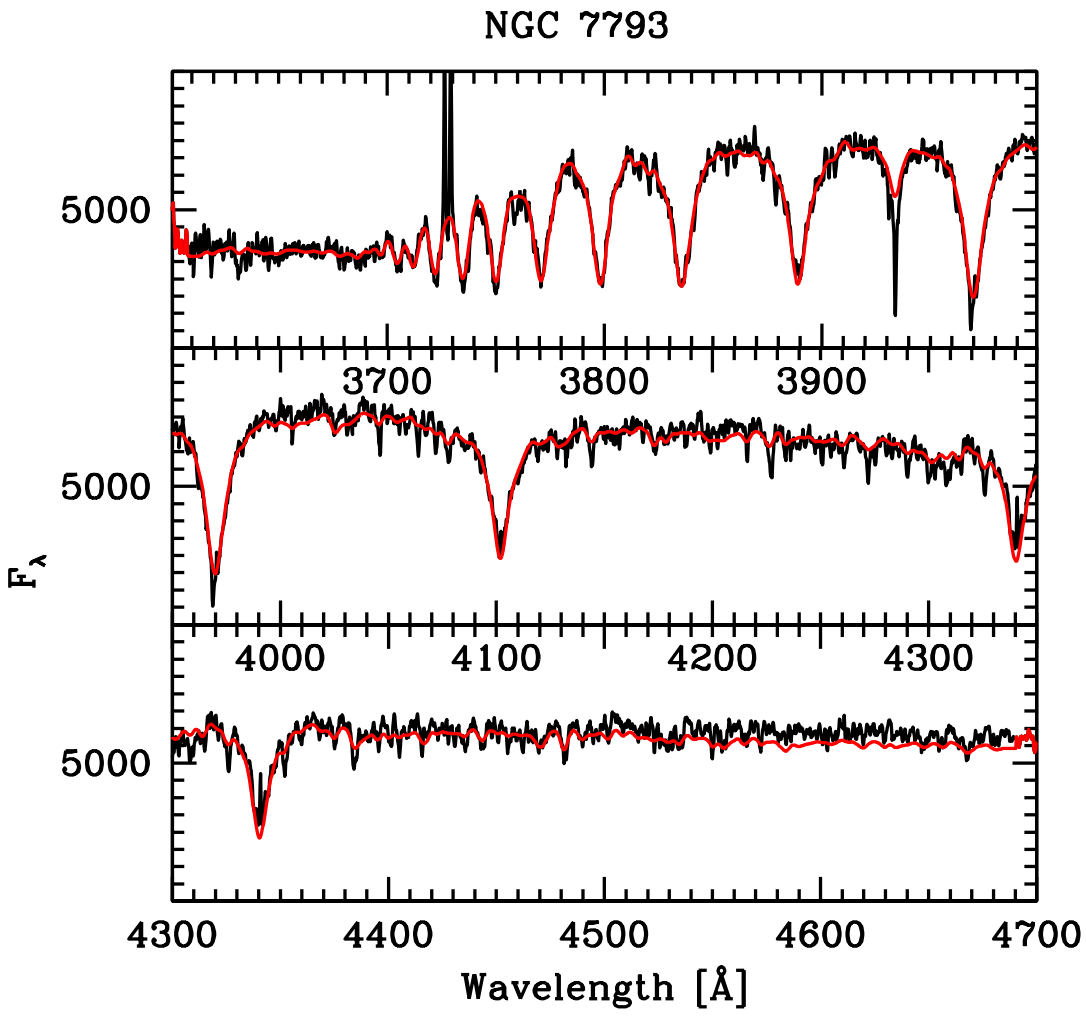

Figure 5.10: Best single age fit for NGC7793 (red line) compared to the observed spectrum (black line). Note that the Balmer and OII emission lines are excluded from the fit. Also note that the single age fit fails to fit the Ca K line.

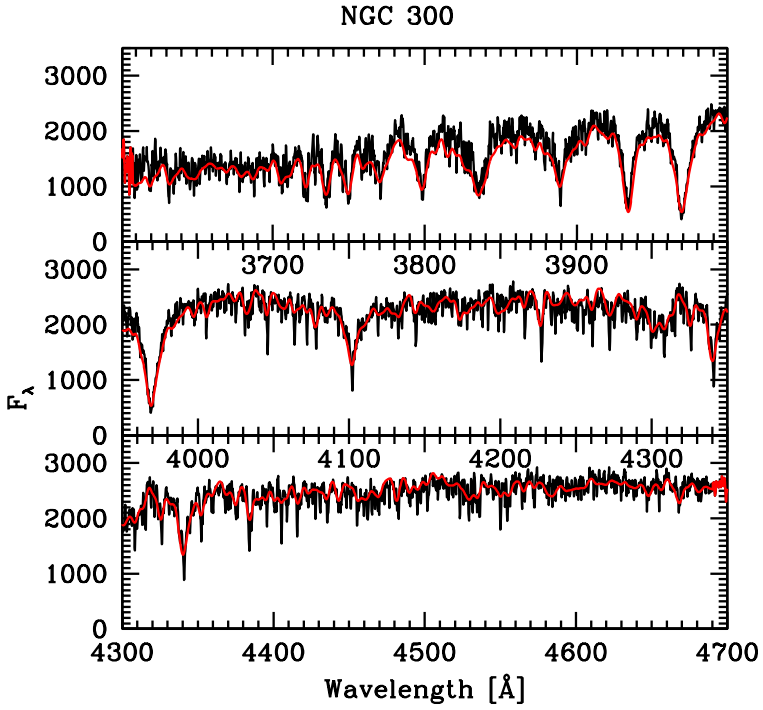

Figure 5.10 *continued*: Best single age fit for NGC300

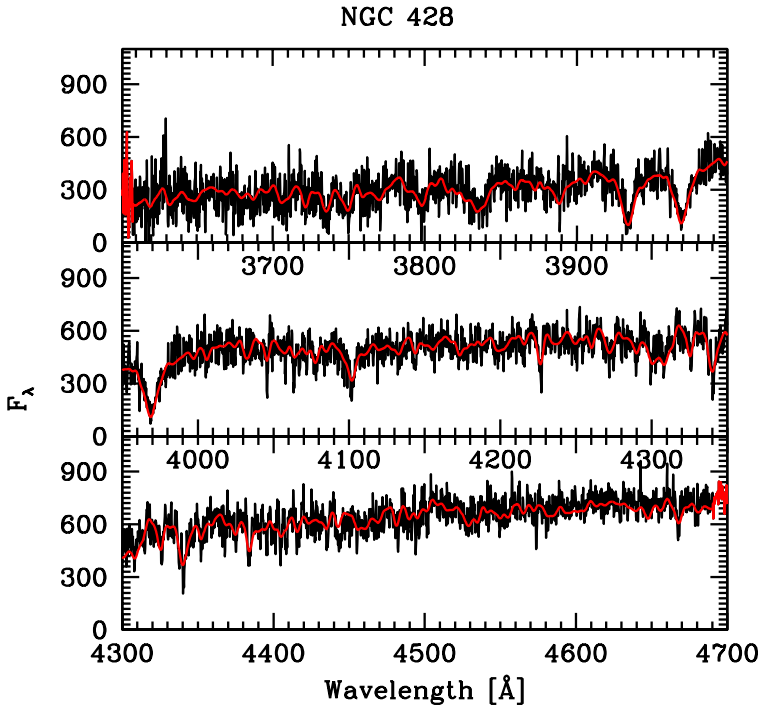

Figure 5.10 *continued*: Best single age fit for NGC428

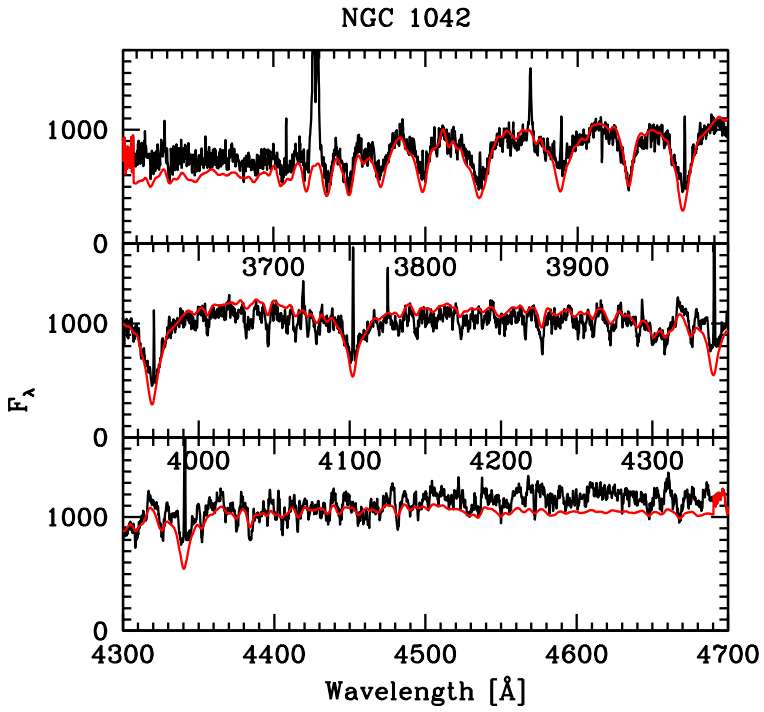

Figure 5.10 *continued*: Best single age fit for NGC1042

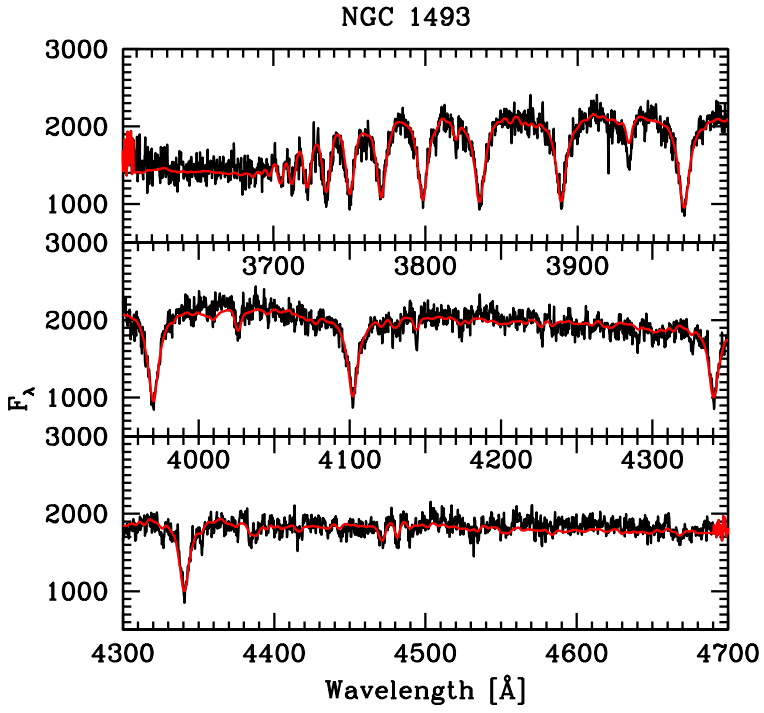

Figure 5.10 *continued*: Best single age fit for NGC1493

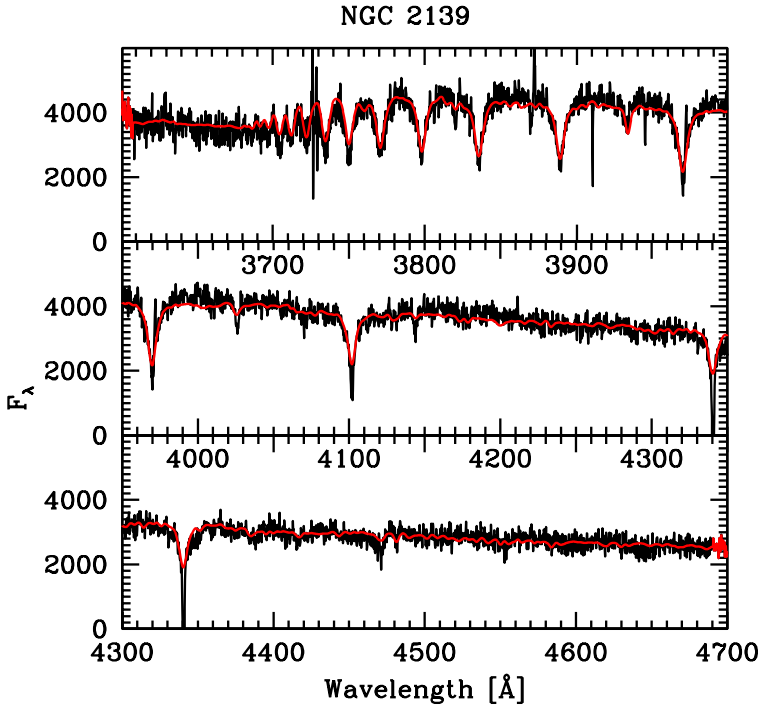

Figure 5.10 *continued*: Best single age fit for NGC2139

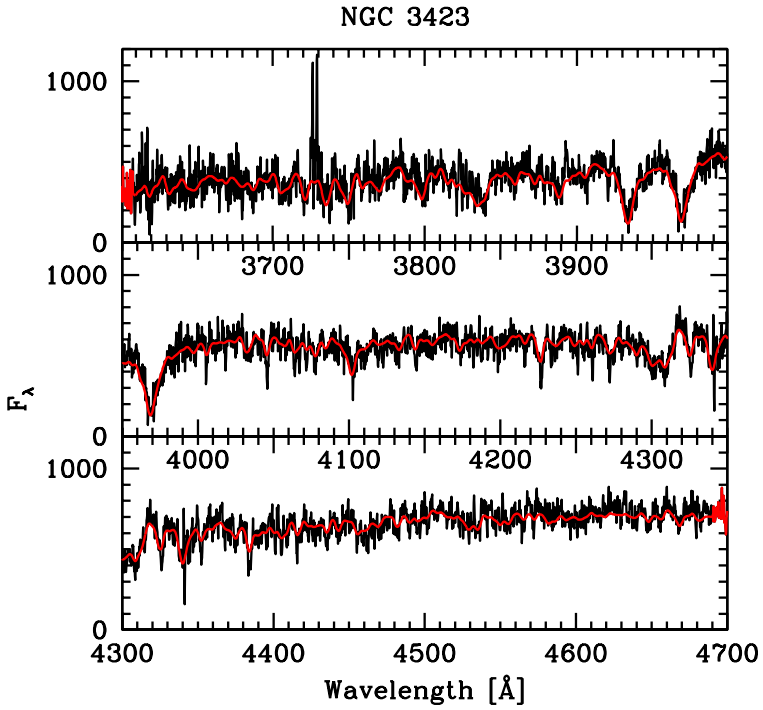

Figure 5.10 *continued*: Best single age fit for NGC3423

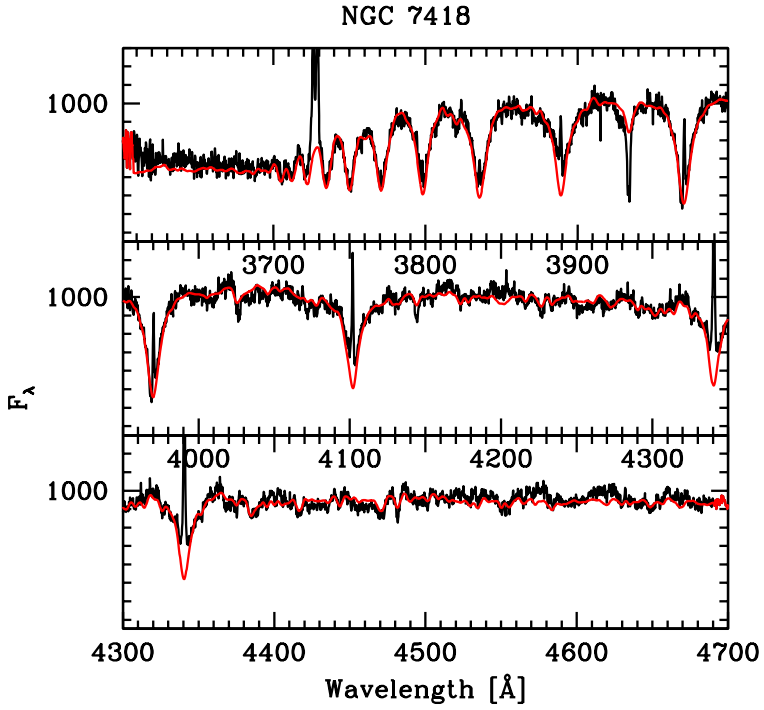

Figure 5.10 *continued*: Best single age fit for NGC7418

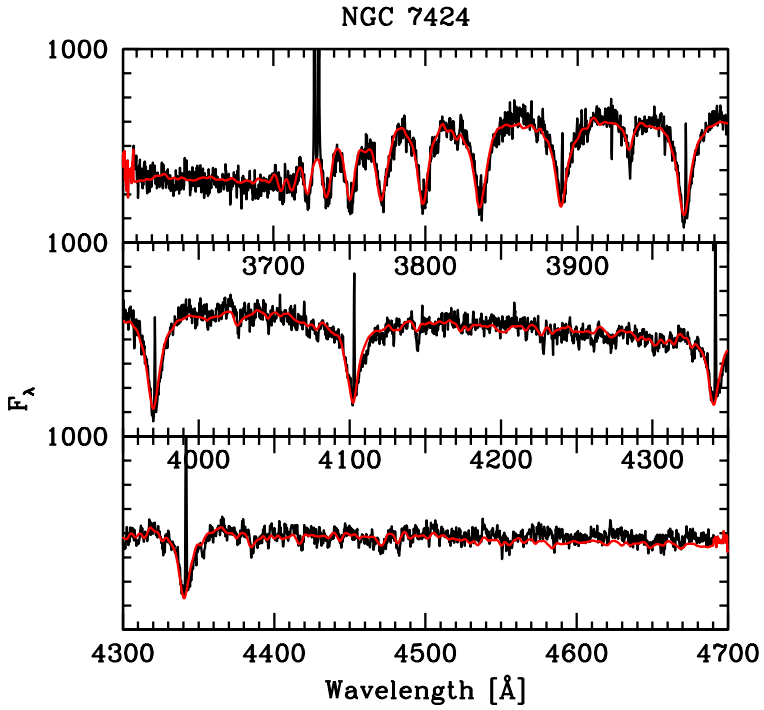

Figure 5.10 *continued*: Best single age fit for NGC7424

use of composite age fits can change the value of the derived extinction considerably. Table 5.4 also quotes the mass-to-light ratios for each derived age as derived from the population synthesis models.

Figure 5.10 shows the observed spectrum of each object along with the SED of the best fit single age. In general the fits are quite good and reproduce also small features of the observed spectrum. As the Balmer and OII emission lines are excluded from the fit, they do not influence the determined age. On the other hand several characteristic features are not fit well. These are e.g. the Ca K line in the NGC7793 spectrum, the continuum shape in NGC1042 as well as the small features around 4600 Å in the spectra of NGC7418 and NGC7424.

In summary, the age of the best fitting single age stellar population is robust in respect to the chosen metallicity and extinction and agrees quite well with the ages as determined from the spectral indices.

5.4 Continuum subtraction

The two objects where the ages derived from the index method and the SSP fitting method agree least, are NGC1042 and NGC2139. These spectra happen to also sport emission lines with a broad base. Indeed given the age of NGC1042 it is hard to explain where the ionizing photons should come from that would power the emission lines. It is an interesting excercise to repeat the SSP fits including a continuum term, thereby testing for the presence of a non-stellar continuum from some low-luminosity AGN. We also include NGC7793 into this excercise as a comparison object.

The fit method is exactly the same as in Section 5.3. However, before the fitting a second order polynomial is subtracted from both the object and the template. This has the effect of removing possible non-thermal contributions to the continuum. However this procedure also removes the thermal continuum, leaving only the absorption lines as a diagnostic. We quote the results as before in Table 5.5.

The control object NGC7793 shows that the derived age and metallicity are indeed independent of continuum subtraction if used on high signal-to-noise spectra. Accordingly the χ^2 value does not change very much. The quoted extinction technically is not the same. However, extinction mostly affects the continuum. It is therefore not surprising to find that the extinction is only weakly constrained from the fits. The extinction values quoted here are for the best fit, however are not significant for any of the spectra.

The age derived for NGC1042 is the same as the one derived before from the SSP fit without continuum subtraction. However the fact that χ^2 is half its former value shows that the fit is significantly improved by the removal of the continuum. This may be due to the different metallicity that is derived. The huge error bars on the NGC1042 age as derived from the Lick indices seems to indicate a problem with

Table 5.5: Ages and metallicities from continuum-subtracted spectra

Galaxy	χ^2	log(Age)	Z	A_I
NGC1042	343	9±0.3	0.02	0.0
NGC2139	424	7.48±0.3	0.008	0.0
NGC7793	14681	8±0.3	0.008	0.1

these indices, possibly the non-subtracted emission lines.

For NGC2139 χ^2 drops significantly, while the age derived from the SSP continuum subtracted fit does agree now with the one derived from the indices. This is what should be expected if a significant featureless continuum is present, given that the index method and the present continuum-subtracted fit both sample only the absorption features and discard the continuum. Interpretation of this result is not straightforward however: the spectra of very young populations (< 10 My) contain O-stars with very blue continua which are also basically featureless. In other words, it is not clear if the continuum we are subtracting here is an O-star continuum or some non-thermal continuum.

5.5 Fitting composite stellar populations

There are different reasons to expect that the spectra are only poorly described by SSP models. First, some of the spectra actually represent an aperture that encompasses cluster light and disk light in similar amounts. Galaxy disks are expected to form stars continually. Their spectra should therefore be better described by a mixture of differently aged stellar populations. Second, as will be shown in Section 6.4, the M/L ratios we derive from the dynamical modelling of Chapter 4 are usually higher than the ones derived from the SSP ages. This can be interpreted in terms of an older population that has higher M/L and therefore is underrepresented in the observed spectrum. The younger population with lower M/L dominates the spectrum, though it may contribute only little to the mass. We therefore want to test if we can robustly detect mixed stellar populations in the nuclear spectra. Ideally we would like to date the last burst of star formation as well as the oldest population in the spectrum.

As described at the beginning of this Chapter, any composite star formation history can be described as a linear superposition of multiple bursts of star formation. The task to assign a linear weight to each SSP in the template set can be conveniently solved by using the `losvdfit` code's inbuilt capability of matching the optimal linear combination of different templates to a given object spectrum. We use the

same template library and the same emission line masks as for the SSP fitting. As initial template we choose the best fit single age from Section 5.3. Although in principle every burst of star formation occuring in the nucleus could have different metallicity, in practice it is important for the sake of a well-defined answer to reduce the number of available templates by choosing one mean metallicity for all templates in the library. It would also be possible that every population, especially the young ones, could have a different extinction. We here however assume that one extinction is sufficient to describe all populations in one specific spectrum, again for no other than the practical reason to reduce the number of free parameters.

One constraint on the finally derived star formation history is that it needs to reproduce the M/L ratios derived from dynamics in Chapter 4. We would also expect the luminosity weighted mean age as determined from the composite fit to be similar to the best fit single age as determined in Section 5.3. The mass M_k and the luminosity L_k corresponding to the k-th template spectrum are given from the population synthesis model. The code also puts out the weight a_k it attributes to template number k with age T_k in the library of n templates. The luminosity weighted mean age $< A >$ and the total mass-to-light ratio M/L are then given by:

$$< A >= \frac{\sum_{k=1}^{n} a_k L_k T_k}{\sum_{k=1}^{n} a_k L_k} \tag{5.8}$$

and

$$M/L = \frac{\sum_{k=1}^{n} a_k M_k}{\sum_{k=1}^{n} a_k L_k}. \tag{5.9}$$

We cover the full χ^2 plane of metallicity and extinction and derive the best fitting composite age fit. Tests show that the code finds very low velocity dispersions of around 10 km s^{-1}. This is to be expected, as the resolution of the templates is lower than the resolution of the object spectra. We therefore keep the velocity dispersion fixed at 10 km s^{-1}. We do not choose zero to stay clear of rounding errors. Similarly the code always fits relative velocities of < 10 km s^{-1}. As no velocity shift is expected anyway, we therefore also keep it fixed at 0 km s^{-1}. Table 5.6 displays the best fit M/L and the best fit age $< A >$ for every object together with the associated metallicity Z and the extinction A_I. Table 5.7 lists the mass-to-light ratio (M/L) and the mass fraction (F_M) of each SSP in the best fit. F_M for an SSP with index number s is here given by

$$F_M = \frac{a_s M_s}{\sum_{k=1}^{n} a_k M_k} = \frac{M_{SSP}}{M_{NC}} \tag{5.10}$$

Although the mass fractions of the young SSPs seem rather low in most cases, note that the M/L varies by two orders of magnitude from young to old ages. So the fractional contributions to the total luminosity (F_L), which is what counts for the fitting process, are higher for the young populations and lower for the old ones.

Table 5.6: Results from composite fits

Galaxy	χ^2	Z	A_I	M/L	$< A >$
NGC 300	1795.7	0.008	0.2	0.96	9.68
NGC 428	329.5	0.02	0.7	0.65	9.31
NGC1042	233.3	0.02	0.2	1.58	9.91
NGC1493	2293.6	0.008	0.2	0.48	9.33
NGC2139	409.4	0.008	0.0	0.06	7.40
NGC3423	3903.0	0.008	0.1	1.12	9.75
NGC7418	204.6	0.008	0.7	0.12	8.26
NGC7424	223.4	0.004	0.1	0.26	9.09
NGC7793	8251.7	0.008	0.1	0.45	9.26

The conversion is $F_L = F_M/(M/L)$. Note however that we quote I-band M/L for easy comparison with the dynamical results. This relation will thus result in I-band luminosities. However the fit is carried out in a spectral region that lies more in the blue. Due to different overall continuum slopes the actual luminosity weights in the fit are different in the sense that older populations contribute less light and younger ones more than what they do in the I band.

To derive errors we assume that the model and the spectrum only differ by the measurement error, i.e. that the model SED is in principle able to describe the observed SED completely. This assumption is better justified than in Section 5.2. There we tried to model the SED with a single age, varying metallicity, no extinction model. Here we allow for extinction and for the presence of composite stellar populations. In the limits of our model we therefore allow for the maximum number of free parameters. Under this assumption, the low χ^2 values we derive for the best fit simply means that we overestimated the errors on the spectra. The expected value for χ^2 is around 4400, as this is the number of measurement points (i.e. pixels) in the spectrum (the exact number is different for each spectrum, as different regions of the spectrum are clipped because of emission lines) minus number of free parameters. Rescaling χ^2 to this expected value is then equivalent to rescaling the errors to a "right" value. Again as in Section 5.2, errors projected on a two parameter space can then be derived from iso-$\Delta\chi^2$ contours. It turns out in all cases that no other combination of the two parameters Z and A_I yields a fit with a $\Delta\chi^2$ of less than 2.3. The derived M/L and $< A >$ depend on a total of 16 parameters (14 template weights, metallicity and extinction). To derive meaningful error estimates one would have to cover the full 16-dimensional χ^2 space. This is computationally too expensive. We therefore will give a discussion of the significance of the results in the next Section.

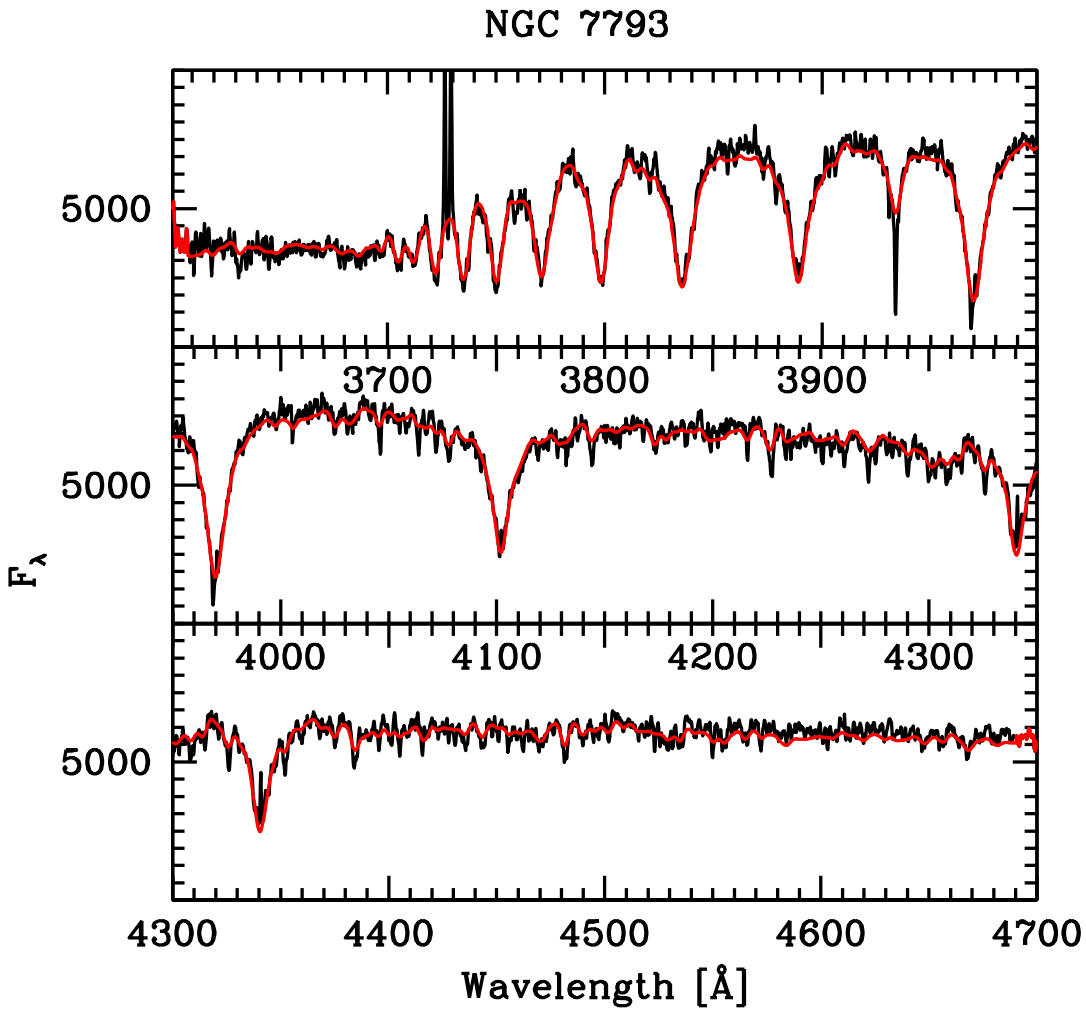

Figure 5.11: Best composite fit for NGC7793 (red line) compared to the observed spectrum (black line). Note that the Balmer and OII emission lines are excluded from the fit.

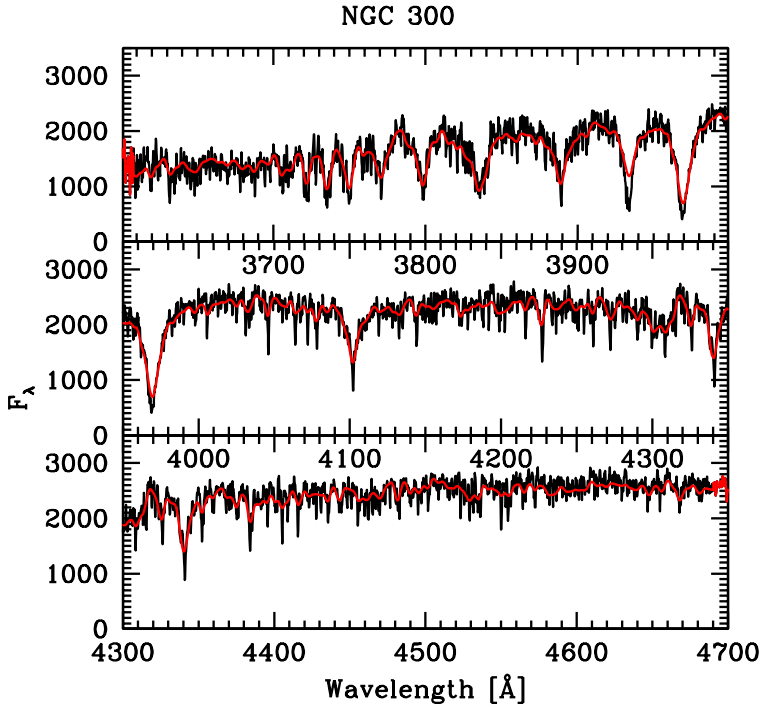

Figure 5.11 *continued*: Best composite fit for NGC300

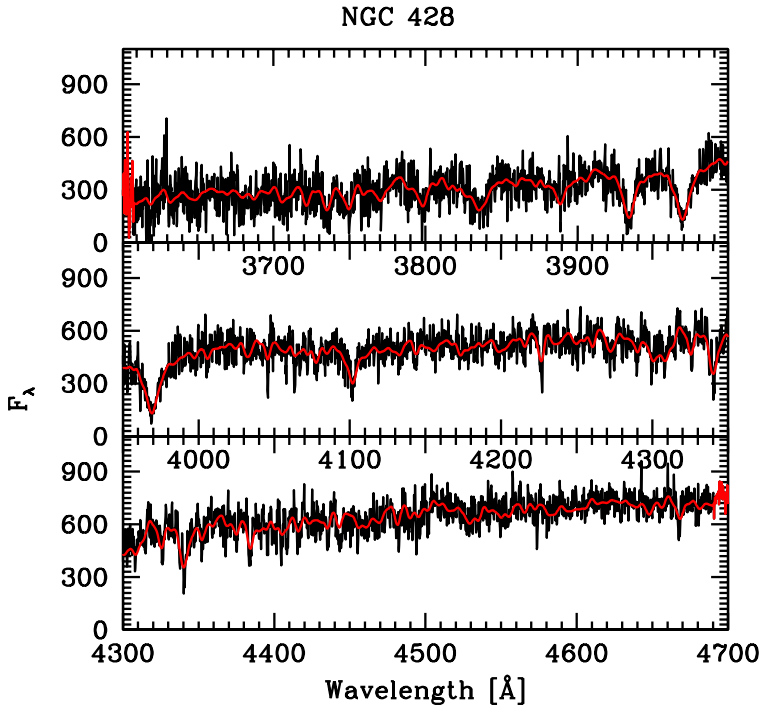

Figure 5.11 *continued*: Best composite fit for NGC428

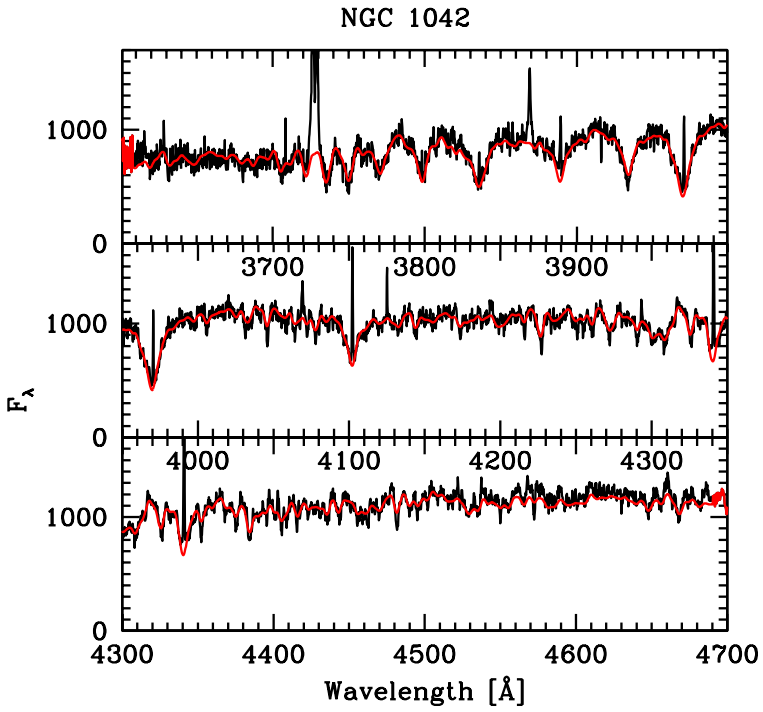

Figure 5.11 *continued*: Best composite fit for NGC1042

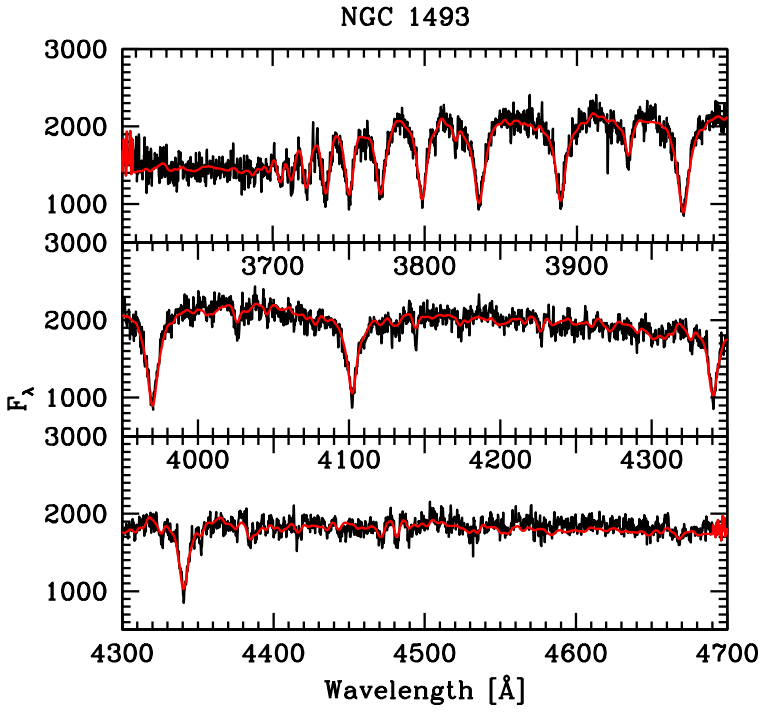

Figure 5.11 *continued*: Best composite fit for NGC1493

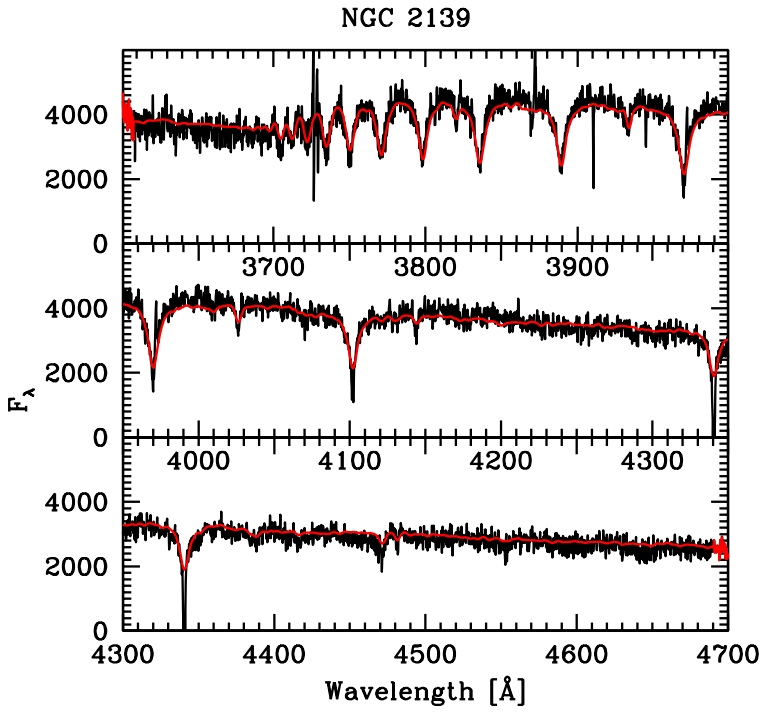

Figure 5.11 *continued*: Best composite fit for NGC2139

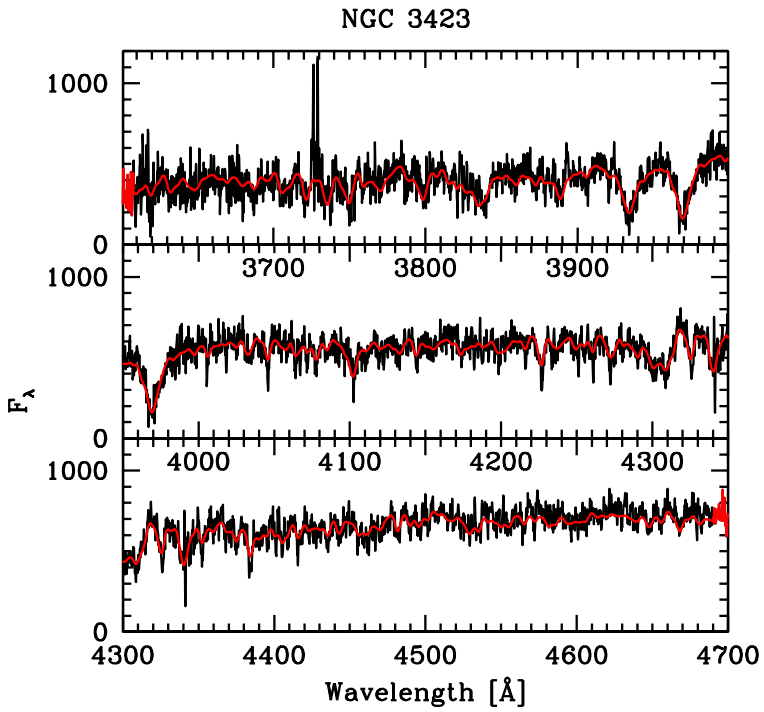

Figure 5.11 *continued*: Best composite fit for NGC3423

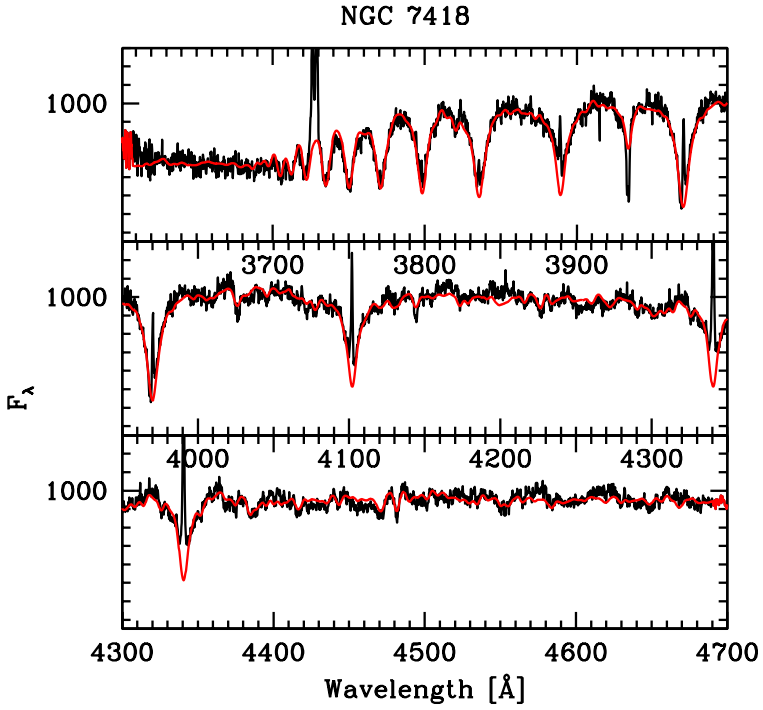

Figure 5.11 *continued*: Best composite fit for NGC7418

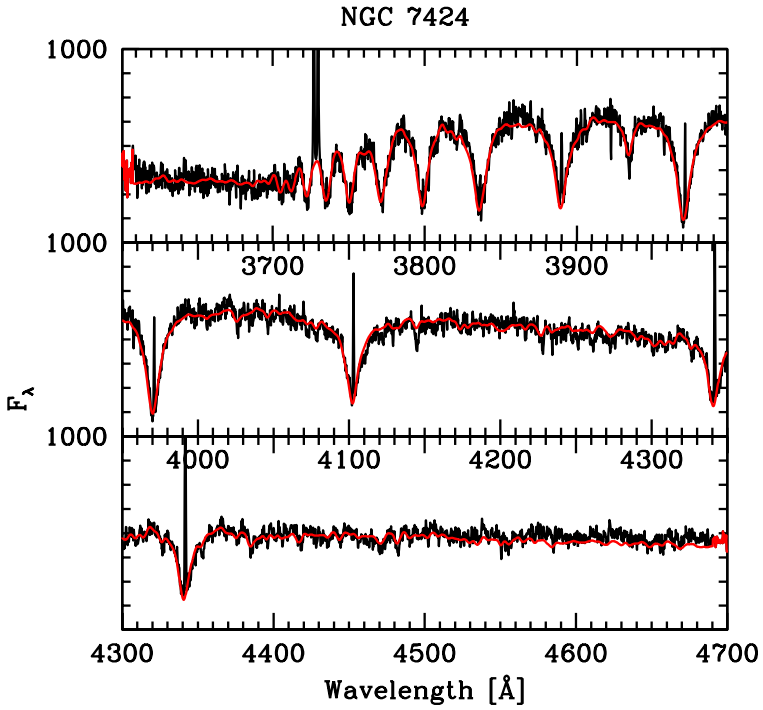

Figure 5.11 *continued*: Best composite fit for NGC7424

Table 5.7: Linear mass weights of contributing SSPs in the composite fit

lg(age)	M/L_I	300	428	1042	1493	2139	3423	7418	7424	7793
6.00	0.05	.000	.000	.000	.000	.000	.000	.005	.001	.000
6.48	0.02	.000	.000	.000	.000	.106	.000	.000	.000	.000
6.78	0.02	.000	.001	.001	.000	.000	.000	.040	.004	.000
7.00	0.02	.000	.000	.000	.000	.000	.000	.000	.000	.000
7.48	0.07	.000	.000	.000	.069	.894	.002	.194	.000	.000
7.78	0.10	.000	.000	.000	.000	.000	.000	.000	.202	.000
8.00	0.15	.022	.000	.001	.000	.000	.000	.032	.000	.160
8.48	0.23	.000	.000	.008	.000	.000	.000	.000	.244	.000
8.78	0.34	.005	.000	.000	.082	.000	.000	.728	.000	.110
9.00	0.41	.012	.283	.046	.000	.000	.000	.000	.000	.000
9.48	0.87	.000	.716	.173	.000	.000	.000	.000	.000	.000
9.78	1.47	.960	.000	.000	.849	.000	.998	.000	.000	.730
10.00	2.08	.000	.000	.000	.000	.000	.000	.000	.000	.000
10.30	3.53	.000	.000	.771	.000	.000	.000	.000	.549	.000

5.6 Comparing the different approaches

We have presented three different methods to derive mean ages, metallicities, extinction parameters and mass-to-light ratios for integrated SEDs of star clusters. It seems worthwhile to compare the results of the different approaches. To facilitate reference we will call the approach of Section 5.2 the index method, the approach of Section 5.3 will be called SSP method and finally the approach of Section 5.5 will be called composite fit.

It is first noteworthy that although the model indices are measured on the exact same spectra that are used for the spectral fitting, the index method does seem to match significantly less well than the spectral fitting. The index method purposedly relies on a very small wavelength range, to extract specific information from the spectrum - it compresses the information. For the spectra of old stellar populations, where the use of the indices has been optimized and is well understood, the index method should be superior to spectral fitting. However a specific disturbance to this small wavelength range, as e.g. emission lines, can lead to significant changes in the reliability of the method. Indeed we believe this is what is happening for our data. The spectral fitting on the other hand does use the full information content of the spectra and provides a means to correct for a disturbance in a small wavelength range by masking it from the fit. It is therefore the method of choice in the following discussion. Spectral fitting however does not allow to distinguish between the effects

of different parameters easily, because the change of one parameter does not only affect a single feature in the spectrum but rather changes the whole SED. This interpretation problem will stay with us during the rest of this Section.

Concerning metallicity, all three approaches agree and measure in general a sub-solar metallicity. It therefore seems safe to draw the conclusion that the nuclei of bulge-less spirals are indeed metal poor, with an average metallicity of 2/5 the solar value.

Concerning extinction, the SSP method seems to produce a coherent picture in the sense that extinction seems in general to be negligible for the old spectra and substantial for spectra with age $\lesssim$ 100 Myrs - just as we would have expected naively. The only exceptions from this rule are NGC428 and NGC2139. However the composite fit does only agree partially here. It seems to be clear that NGC7418 is highly extincted. This is consistent with the dust lane that is visible on the HST I-band image. NGC428 is the only other object where extinction is high (0.7) from the composite fit. An explanation for this somewhat surprising finding might be that NGC428 galaxy as a whole probably is a recent merger and is forming stars at a rather high rate (Smoker et al., 1996). All other objects have moderate extinctions of 0.1 to 0.2 mag. This is most surprising in the case of NGC2139, which does have a very young spectrum. As pointed out earlier the measured extinction depends most strongly on the slope of the continuum. The continuum slope itself is a function of age and metallicity. Therefore there clearly is a trade-off between including an old population into the composite fit and applying a higher extinction. Or vice-versa including a young population into the fit or applying a lower extinction. While extinctions measured from SSPs therefore are certainly biased, the extinctions measured from the composite fit should be less influenced by systematic biases.

Concerning age, the index method and the SSP method agree remarkably well within the errors - despite all problems with the later. Thus, both suggest a distinction into two groups of nuclei: those that are $\lesssim$ 0.1 Gyr (NGC1493, NGC2139, NGC7418, NGC7424, NGC7793) and those that are $\gtrsim$ 1 Gyr (NGC300, NGC428, NGC1042, NGC3423). Note that none of the inferred ages are nearly as high as those of the globular clusters of the Milky Way.

The mean luminosity weighted age as derived from the composite fit is older in all nine cases. The division into 4 old and 5 young nuclei is however still valid in the sense that NGC300, NGC428, NGC1042 and NGC3423 all have less than $<$3% of their mass in any population younger than 1 Gyr. For the other 5 spectra this fraction is at least 15%. From the point of view of the composite fit, none of the single age fits are statistically acceptable. Although this is not obvious from Figures 5.10 and 5.11, χ^2 increases by 48 % from the composite fit to the SSP fit on average over all nine spectra (30% leaving out the drastic case of NGC1042, see also Figure 5.14). A very close inspection of the fits backs up these numbers. For example in NGC7793 the fit to the Ca K line as well as the redmost range of

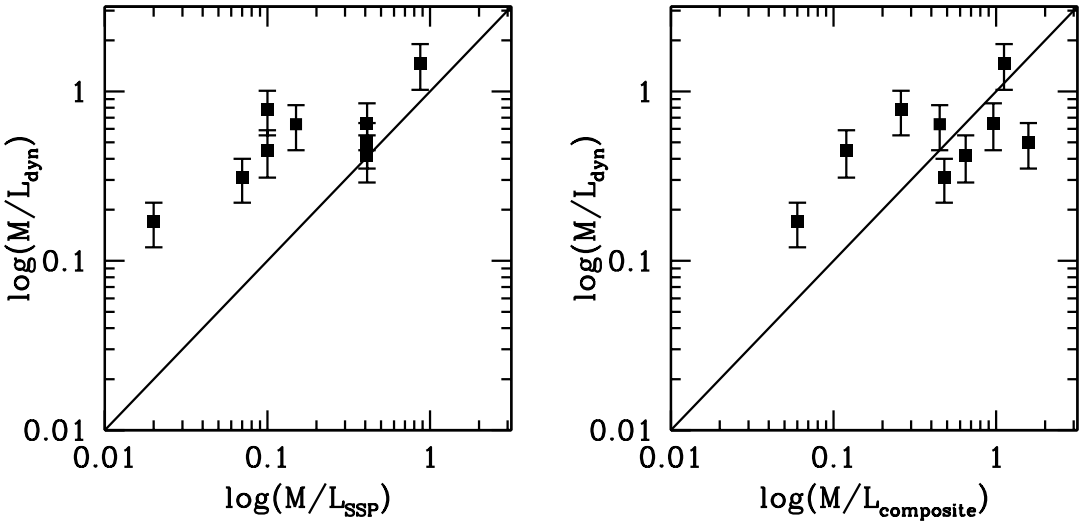

Figure 5.12: The mass-to-light (M/L) ratios as derived by the dynamical analysis of Section 4 against the M/L as derived from fitting SSPs to the blue spectra (left, Section 5.3) or from fitting composite stellar populations (right, Section 5.5). The line indicates a one-to-one relation. Note that the M/L values of the composite fit are a better match to the M/L as measured from the dynamics.

the spectra is visibly improved in the composite fits. There is another indication that we are doing something right by allowing for a composite fit. It was discussed earlier that the M/L ratios derived from the dynamical analysis should be matched by the population analysis. Figure 5.12 shows the mass-to-light ratios derived from the dynamical analysis against the mass-to-light ratios derived from the population analysis. Left is for the assumption of a single-age population in the spectra. It is obvious that all but one object lie above the one to one relation indicated as a straight line. This systematic offset is reduced significantly if the mass-to-light ratio from the composite fit is plotted into the same graph (right) - albeit with a very large scatter. Note here that this comparison is fully justified also in respect of the contamination from non-cluster light, because both values have been determined on spectra that were extracted on the same aperture.

In Figure 5.12 there is one significant outlier, namely NGC1042 at an M/L_{comp} of 1.58. However, M/L as well as mean age values depend of course on which weight is given to each template. The central question therefore is: How significant is the weight of each template? Proper treatment of this question requires that we purposedly vary the weight a_k of each template in the fit. It is not feasible to vary on purpose the mass or the I-band luminosity weight directly, because the derived total mass and the total I-band luminosity are different in each fit. However the total

integrated luminosity over the range of the blue spectra is constant. By excluding specific templates from the composite fit or subtracting a specified percentage of the blue light in form of one template we can then study the response of the fit.

How significant are the higher M/L we derive from the composite fit? The high mean age and M/L of NGC1042 is mostly due to the inclusion of a very old, 20 Gyr old population into the fit. To test if this very old component is statistically significant, we repeat the composite fit excluding the oldest contributing SSP template. The results are summarized in Table 5.6. The fit is degenerate as to which one of the old populations we include. This can be understood intuitively by looking at Figure 5.1. There the difference between the 1 Gyr old template and the 10 Gyr old template is much smaller than the difference between 0.1 Gyr and 1 Gyr. NGC7424 is just another example. We also test if it would be possible to inflate the M/L of NGC3423 to the dynamically required value. To that end we exclude the 3 and 6 Gyr old templates from the composite fit. In this case, there is a marginally significant increase in χ^2. It follows that the mass fractions as given in Table 5.7 are only certain to around 50%. It would be desirable here to be able to fix the M/L in the composite fit of each spectrum to the dynamically derived value, effectively thus fixing the total mass of the cluster. We can rewrite Equation 5.9 to

$$\sum_{k=1}^{n} a_k(M/L_{NC} \times L_k - M_k) = 0, \tag{5.11}$$

which is linear in the a_k. This additional constraint on the fit will be implemented in a future version of the `losvdfit` code.

In summary, it currently seems impossible to accurately age date the first generation of stars in these spiral nuclei. The mass-to-light ratio however depends heavily on this component, it seems therefore impossible to derive an accurate prediction for M/L from the spectra alone. This is why we do not quote any M/L in Table 5.6 which summarizes the results of our age dating efforts. The mean age we quote there is the age as determined from the SSP method, as this is much better defined.

On the other hand, in NGC2139 even a modest contribution of 10% of the blue light from any population ≥ 0.1 Gyr is ruled out, in qualitative agreement with the very low M/L derived dynamically. It is quite possible therefore that NGC2139 is a *forming* nuclear cluster!

How significant is the age of the youngest stellar population that contributes to the fit? Or in other terms, is there an upper bound to the age of the last star formation burst in the spiral nuclei? We derive this age by reducing step by step the number of available templates in the composite fit. That is, we start from the best fit, obtained from a total of 14 template SSPs ranging in age from 1 Myr to 20 Gyr. We then omit first the youngest SSP age, leaving only 13 templates ranging from 3 Myr on. Then we repeat the fit omitting also the 3 Myr template, leaving only 12 templates from 6 Myr to 20 Gyr and so on. The age of the last star

Table 5.8: Restricted composite fits

Galaxy	χ^2_{old}	χ^2_{new}	M/L_{new}	$< A >_{new}$
NGC1042[1]	233.3	233.6	0.73	9.39
NGC3423[2]	3903.0	3909.3	1.58	9.97
NGC7424[1]	223.4	223.6	0.12	8.12

[1] The templates with age 10 Gyr and 20 Gyr have been removed from the template list for the composite fit. [2] The templates with age 3 and 6 Gyr have been removed from the template list for the composite fit.

formation burst then is the age of the SSP whose omission increases χ^2 significantly. The results of this procedure are shown in Figure 5.13 as $\Delta\chi^2$ plots. Although an exact definition of a confidence interval is non-trivial here (because of the change of degrees of freedom per fit), it is clear for all spectra, which SSP's omission changes $\Delta\chi^2$ drastically. A conservative estimate of the last star formation age is given by the 99% confidence region in a 14 dimensional parameter space ($\Delta\chi^2 < 29$). Ages of the last SF burst (A_{lb}) derived this way are given in Table 5.6. The mean age of the last star formation burst is then 44 Myr.

To derive estimates on the mass of this burst, one could think of varying the mass fraction F_M of the last star formation burst (see Equation 5.10). However we have seen above that the total mass of the population fit is not well constrained. This leads to a serious problem also in the present case. Fitting after subtraction of a certain SSP may change the total M/L and thus M_{NC} erratically. Indeed, increasing the fraction of light that a specified SSP contributes to the total blue luminosity of the object spectrum, does not necessarily imply increasing its mass fraction too. In the case of an increase of the total M/L, the mass fraction of the specified SSP may actually decrease. In turns out in practice that this is exactly what happens, making it impossible to derive a robust estimate of the mass of the last star formation burst.

For completeness, let us state that our results are consistent with the literature. A young age for the NGC7793 nucleus has already been inferred by Frogel (1985); Diaz et al. (1982). The disk of NGC 300 has a metallicity of 0.006 (Butler et al., 2004), very similar to what we derive for its nuclear region.

Can we extend our conclusions about the spectra to the nuclear clusters themselves? We test if the presence of multi-age populations in the spectra can be ascribed to the contamination by non-cluster light (NCL). We compute a measure of the statistical difference between the SSP and the composite fit, namely

$$\Delta\chi^2 = (\chi^2_{SSP} - \chi^2_{comp})\frac{N_{DoF} - N_{free}}{\chi^2_{comp}}, \tag{5.12}$$

where N_{DoF} is the number of degrees of freedom and N_{free} is the number of free

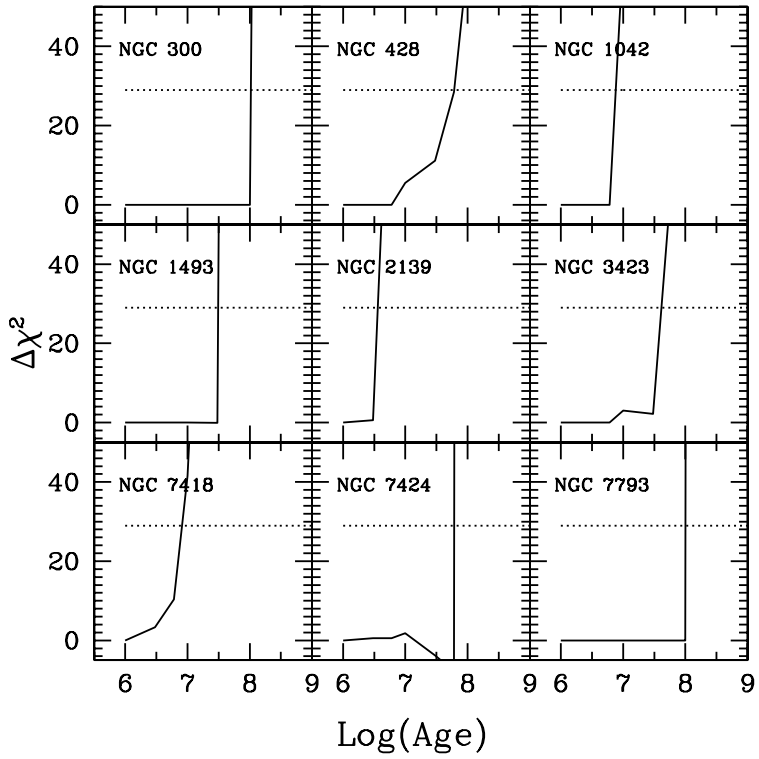

Figure 5.13: $\Delta\chi^2$ as a function of the age of the youngest SSP in the template library for the composite fit. The dotted line shows the 99% confidence region in a 14 dimensional parameter space ($\Delta\chi^2 < 29$).

parameters. In Figure 5.14 we plot this $\Delta\chi^2$ against the fraction of non-cluster light NCL from Table 3.1. Less disk contaminated spectra are not more consistent with a single-age model. For comparison the 99% confidence limit in a 14 dimensional χ^2 space is shown as a dotted line. We therefore conclude that the presence of mixed populations is a general feature not only of these galaxy center, but also of the nuclear clusters. As we find no evidence that there are significant population differences between disks and clusters, we will assume for the discussion of the next chapter that the results of this chapter are representative for the populations in the clusters.

In summary, there is strong evidence that nuclear star clusters have low metallicity, multiple aged stellar populations. The derived population quantities are summarized in Table 5.6.

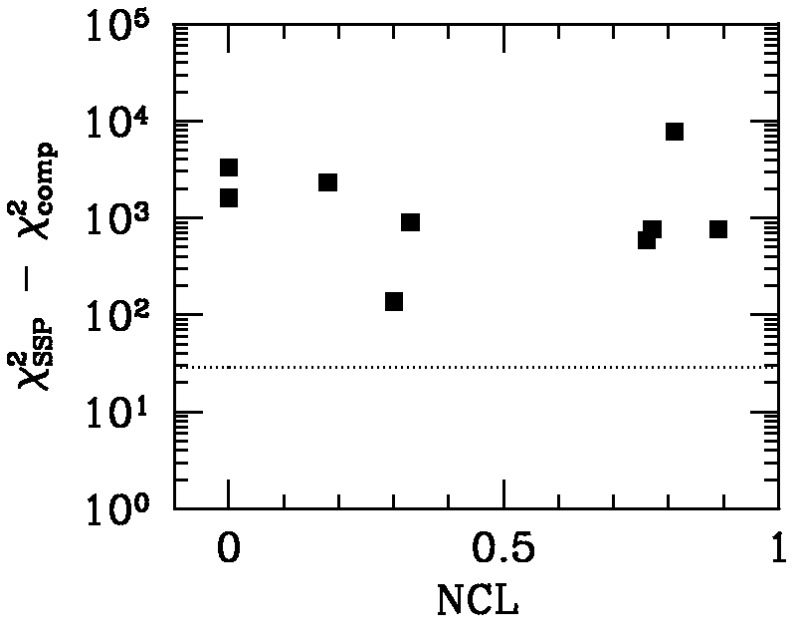

Figure 5.14: $\Delta\chi^2$ between SSP fit and composite fit against the fraction of non-cluster light NCL in the spectra. The absence of a correlation shows that the presence of composite populations is a general feature not only of these galaxy center, but also of the nuclear clusters.

Table 5.9: Population quantities

Galaxy	$\log(< A >)$	Z	$\log(A_{lb})$
NGC0300	9.00	0.008	8.00
NGC0428	9.00	0.02	7.78
NGC1042	9.00	0.02	6.78
NGC1493	7.48	0.008	7.48
NGC2139	6.78	0.008	6.48
NGC3423	9.48	0.008	7.48
NGC7418	7.78	0.008	6.78
NGC7424	7.78	0.004	7.78
NGC7793	8.00	0.008	8.00

Note: Errors on the mean ages are $\pm$ 0.3 dex. Errors on Z and $\log(A_{lb})$ are less than the sampling size of the chosen model grid.

Chapter 6

Interpretation

Where we try to make some sense of the results we obtained.

We here examine the consequences of what we found in Chapters 4 and 5. We put the structural properties of nuclear star clusters in relation to other star clusters. We also use the derived age information to examine whether NCs could be the progenitors of other known massive clusters. We finally derive the duty cycle of star formation in the nuclei of bulge-less galaxies and use it to constrain gas transport processes in disks.

6.1 Comparison to other dynamically hot systems

Dynamically hot stellar systems are defined by three observable quantities (neglecting effects of non-homology): velocity dispersion σ_e, effective radius r_e and effective surface brightness I_e. The total luminosity and mass are related to these quantities according to $L = 2\pi r_e^2 I_e$ and equation (4.1). Dynamically hot systems satisfy a variety of correlations between their fundamental quantities, generally known under the keyword "fundamental plane". Any derived quantities will therefore also correlate. A popular way to view these relationships is κ space (Bender et al., 1992). The κ parameters are defined in terms of the fundamental observables so that κ_1 is related to mass, κ_3 is related to M/L, and κ_2 is related to the product of M/L and the third power of the effective surface brightness. Elliptical galaxies fall on a fundamental plane that is seen edge-on when viewed as κ_1 vs. κ_3 and is seen face-on when viewed as κ_1 vs. κ_2. Intrinsic age spreads however complicate the interpretation in κ space, because κ parameters are defined using luminosity surface density. Here we have done detailed modeling that provides mass and M/L directly of our sample NCs. We therefore choose to work with the more fundamental properties, rather than resort to κ space.

In Figure 6.1 we plot effective projected mass density ($\Sigma_e \equiv (M/L)I_e$) vs. mass.

This is similar, but not identical, to a plot of κ_1 vs. κ_2. Discussions of the latter that are of relevance to the present topic can be found in Geha et al. (2002) and Martini and Ho (2004). We plot a wide variety of different dynamical systems. Galaxy sized systems fill the lower right corner of the plot. Here small skeletal triangles show galaxy type systems from the compilation in Burstein et al. (1997). The dwarf spheroidal (dSph) galaxies have been specially marked with additional open triangles. M32, the nearest compact elliptical galaxy, is marked with an open pentagon filled with a star. The nucleated dE galaxies of the Virgo cluster from Geha et al. (2002) are represented by open squares filled with a cross. Stellar clusters on the other hand fall on a well defined band in the left of the plot. Here NCs are represented by black squares. The nuclei of dEs in Geha et al. (2002) are shown as open squares. Small stars show the locus of Milky Way globular clusters. Structural parameters (r_e and total V luminosities) of 108 Galactic GCs are derived from the online catalogue of King-model parameters maintained by W. E. Harris (Harris, 1996). Total cluster masses and related derived quantities then follow from applying V-band mass-to-light ratios computed by McLaughlin & van der Marel (2004, in prep) using the population-synthesis code of Bruzual and Charlot (2003). These population-synthesis M/L values generally compare quite well with the dynamical M/L_V derived by McLaughlin (2000) for a subsample of 40 globulars with measured velocity dispersions; see McLaughlin & van der Marel (2004, in prep) for more details. The most massive globular cluster of the Milky Way, ω Cen (NGC5139), is specially marked as a big star. G1, the most massive globular cluster of M31 (Meylan et al., 2001; Baumgardt et al., 2003) is also pointed out as a filled triangle. The most massive globular clusters of Centaurus A (NGC5128 Harris et al., 2002; Martini and Ho, 2004) are represented as starred crosses. Two super star clusters in M81 with dynamical mass estimates from McCrady et al. (2003) are shown as starred triangles. These were selected to be particularly bright and hence are not representative for the total SSC population. The young, peculiar globular cluster in NGC6946 described in Larsen et al. (2001) is denoted by an open triangle. It resides in an Sc galaxy in the disk at 5 kpc from the center and is surrounded by an extended star forming region. The cluster is extremely luminous (M_V=-13.2) and relatively massive (1.7×10^6 $M_\odot$). Also shown is the most massive cluster known, W3 in the merger remnant galaxy NGC 7252 (Maraston et al., 2004). We additionally plot the approximate locus of the ultra compact dwarf galaxies from Drinkwater et al. (2003) as a solid circle. As these authors do not give numbers for each one of their objects we plot only a mean of the range of values given in that paper. The solid line running through the cluster sequence represents a line of constant $r_e = 3$ pc, which is appropriate for Milky Way globular clusters.

Concentrating on the mass scale only, Figure 6.1 shows that NCs are more massive than the typical Milky Way globular cluster by more than one order of magnitude. While MW globular clusters range from 10^4 – 10^6 $M_\odot$, NCs fall in the range

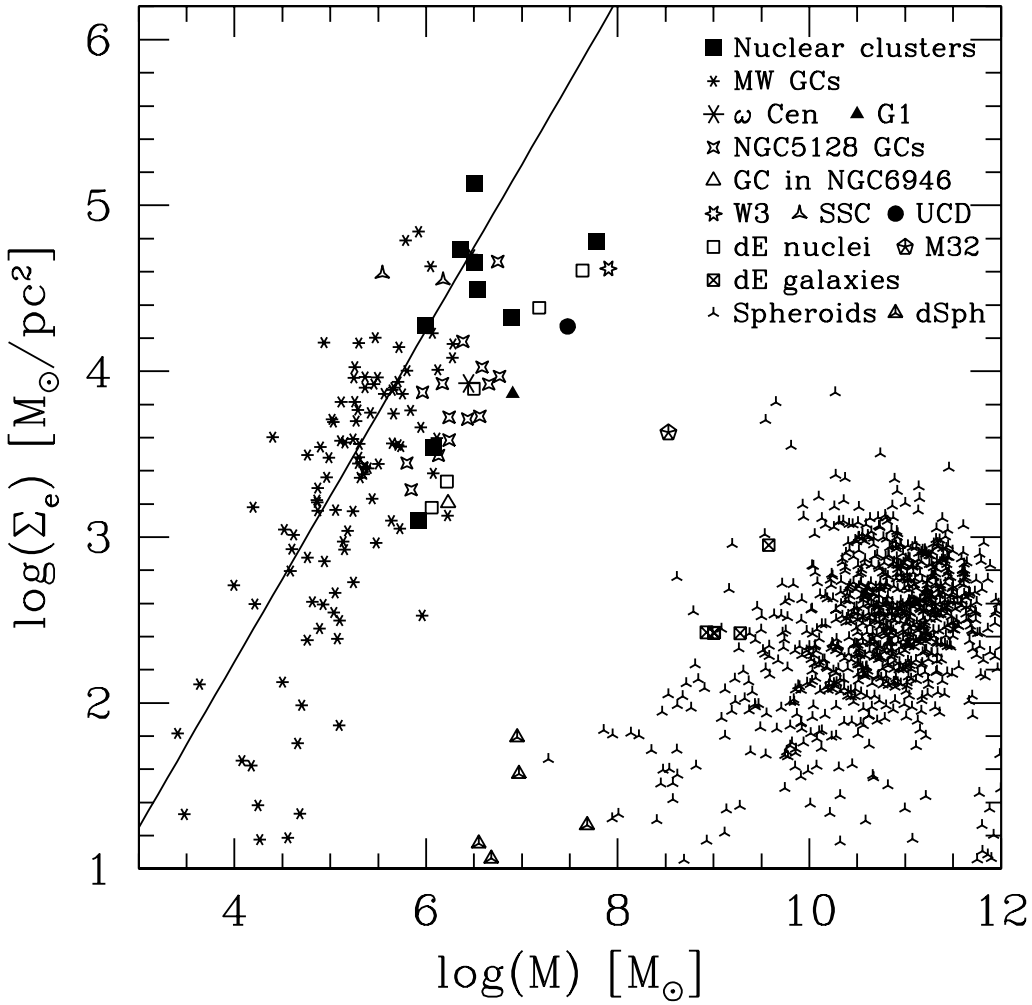

Figure 6.1: Mean projected mass density inside the effective radius against the total mass. This is similar to face-on view of the fundamental plane. Symbols represent different types of dynamically hot stellar systems. Nuclear clusters occupy a region together with different types of massive stellar clusters and are well separated from any bulge. The solid line represents the locus of clusters with constant radius, r_e = 3 pc.

10^6 – 10^7 $M_\odot$. Several extragalactic star clusters are however also found in this range. First the globular cluster system of Centaurus A extends the mass range of globular clusters by one order of magnitude. Then several clusters that have been speculated to be the remaining nuclei of accreted satellite galaxies are also found in this mass range (e.g. ω Cen or G1). Further the least massive galaxies, i.e. the dSph galaxies, are as massive as the most massive stellar clusters, showing that the stellar mass ranges of galaxies and star clusters overlap.

A clear distinction between clusters and galaxies however remains. dSph galaxies are less dense by 4 orders of magnitude than the most massive clusters. It is indeed striking that all massive clusters prolong the well known globular cluster sequence towards higher masses and higher densities. Nuclear star clusters fall well on this sequence, while there is a wide gap in properties to the location of compact ellipticals or bulges. Indeed the later Hubble type a galaxy has, the more its bulge will become exponential and blend with the underlying disk (compare MacArthur et al., 2003; Böker et al., 2003b, and references therein), instead of remaining a small but distinct entity. Compact small bulges do not exist or at least have not been observed so far. While at first sight a tempting hypothesis, because of their location at the centers of their host galaxies, a smooth evolutionary transition from NCs to bulges therefore seems highly unlikely as there are no transition objects to fill the gap in Figure 6.1.

The well-defined cluster sequence also means that, independent of their different environment, nuclear star clusters follow similar scaling relations between mass and radius as all other types of star clusters. From their location in Figure 6.1 the ultra compact dwarf galaxies of the Fornax cluster (Drinkwater et al., 2003) may well have to be treated as huge star clusters. There is only a hint at a possible discontinuity in properties. While Milky Way globular clusters are consistent with a constant radius line, the cluster sequence may bend over at a characteristic scale of $\approx 10^6$ $M_\odot$, in the sense that more massive clusters have larger effective radii. This is analogous to the so-called "zone of avoidance" in the κ-space cosmic metaplane, as discussed e.g. in Burstein et al. (1997). Those authors infer an upper limit to the 3-D luminosity density which scales roughly as $\sim M^{-4/3}$. In our plot of 2-D mass density, the empty upper-right region of Figure 6.1 suggests $\Sigma_{\rm max} \sim M^{-1/2}$.

6.2 Phase space densities

Figure 6.2 shows f_h, the characteristic phase space density inside the half-mass radius, against mass for the same types of stellar systems as used in Figure 6.1. We define f_h using the half-mass radius r_h, total mass M and measured velocity dispersion σ according to

$$f_h = \frac{\rho_h}{\sigma^3} = \frac{M}{2}\frac{1}{\frac{4}{3}\pi r_h^3 \sigma^3} \propto r_h^{-2}\sigma^{-1}. \qquad (6.1)$$

This quantity can be calculated for various dynamically hot systems using the literature mentioned in Section 6.1. The projected effective radii r_e have been converted to 3-D half-mass radii r_h by the approximate relation $r_e = 0.75\ r_h$ (see Spitzer, 1987, p. 12). No correction was applied to the velocity dispersions.

Additionally the lines in Figure 6.2 show fits to two different subsets of the systems. The dotted line is a fit to Milky Way globular clusters only, where $\log(f_h) = 2.57 - 0.5 * \log(M)$. The virial theorem dictates that $M \propto r_h \sigma^2$. The fit therefore is a line of constant r_h, where $r_h \approx 8$ pc. The solid line is a fit to the galaxy type systems, where $\log(f_h) = 3.44 - 1.1 * \log(M)$ (excluding the Virgo dE,N from Geha et al., 2002). This fit implies that $M \propto \sigma^{3.3}$, which is a Faber and Jackson (1976) type relationship.

Again as in Section 6.1 nuclear clusters fall on the locus of typical massive star clusters. There is a clear discontinuity to galaxies, but more importantly a change of slope, thereby reinforcing the statement that nuclear star clusters are typical massive star clusters (and not progenitors of bulges).

On the other hand the phase space densities may be directly linked to star formation processes. Dynamical evolution is potentially not responsible for the slope observed in the cluster sequence as there is no obvious trend with age, even though the ages of the involved clusters range from around 10^7 years (SSCs, YMC in NGC6946) over 10^8 years (some of the NCs, W3) to very old objects like the Milky Way globular clusters. A more detailed interpretation of this result clearly requires simulations of the formation of massive star clusters and NCs in particular.

6.3 Formation of intermediate mass black holes

Due to their very high mass densities, NCs might be considered to be ideal candidates for fast core collapse and subsequent runaway merging of young massive stars, thus forming an intermediate mass black hole. Comparison with relevant current models (Zwart et al., 2004, Marc Freitag, priv. comm.) however shows that NCs do not fall into the appropriate region of parameter space. The dynamical friction time scale t_{df} for a massive star in a roughly circular orbit to sink from the half-mass radius R to the cluster centre is given in Equation (1) of Zwart et al. (2004) as

$$t_{df} = \frac{< m >}{100 M_\odot} \frac{0.138 N}{ln(0.11 M / 100 M_\odot} \left(\frac{R^2}{GM} \right)^{1/2}. \qquad (6.2)$$

Here $< m >$ and M are the mean stellar mass and the total mass of the cluster, respectively, N is the number of stars, and G is the gravitational constant. Typical values of NCs are $R = 3$ pc, $< m > = 3$ M$_\odot$, N $= 1.5 \times 10^6$ and $M = 5 \times 10^6$ M$_\odot$. We thus obtain a dynamical friction time scale of the order of 24 Myr for a 100 M$_\odot$ star, which is much longer than its lifetime. These stars therefore will explode as

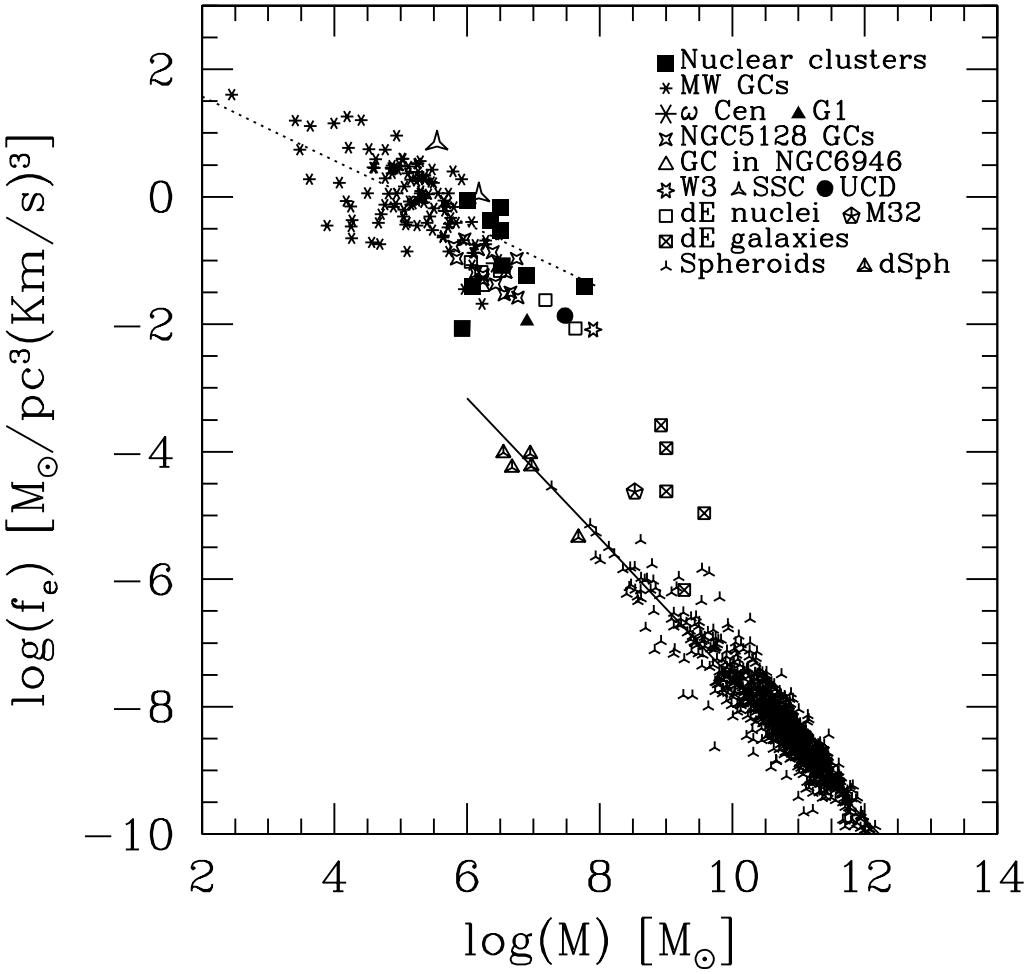

Figure 6.2: The characteristic phase space density f_h, i.e. the mean phase space density inside the half-mass radius r_h for the same dynamically hot systems as in Figure 6.1. The dotted line represents the locus of systems that obey the virial theorem and have constant radius r_h. The solid line represents a locus of systems that obey the virial theorem as well as a Faber-Jackson (1976) type relationship of the form $M \propto \sigma^{3.33}$.

supernovae before reaching the center of the cluster and will not experience runaway merging. Less-massive stars undergo weaker dynamical friction, and are thus even less likely to reach the cluster center in an appropriate timescale for the formation of a black hole.

6.4 The duty cycle of star formation

The age of the last star formation burst in the NCs can be used to derive the duty cycle of star formation in the clusters. The duty cycle is the fraction of time during which star formation is "on", i.e. the fraction of time that the clusters are actively forming stars. Let us assume the typical duration of one star formation event is 10^6 years. For each cluster we know that no star formation occurred in the time since the last burst. So, each individual cluster was on a fraction $f^k_{on} = 10^6 y/A^k_{lb}$ of the time. Here A^k_{lb} is the time since the last burst in cluster k as taken from Table 5.6. All n clusters together were on a fraction

$$f_{on} = \frac{n10^6 y}{\sum_{k=1}^{n} A^k_{lb}} \tag{6.3}$$

of the time, which is the current duty cycle. The duty cycle as derived from the nine clusters in our sample is then 2.3 %. Assuming the typical duration of a burst is 10^7 years yields a duty cycle of 23 %.

We also derive the star formation rate $<$ SFR $>$ in the mean over all nine clusters in our sample. We follow two different approaches. First we simply assume that clusters build their mass M_{clus} (as given in Table 4.2) continually over a Hubble time $t_H = 10$ Gyr:

$$< \mathrm{SFR} >_1 = \sum_{k=1}^{9} \frac{M^k_{clus}}{t_H} = 9 \times 10^{-4} M_\odot / y \tag{6.4}$$

Second we check for the consistency of this picture over the most recent 10^8 years. We take the best fit mass weights m^k_l of the composite population fits at face value. Here k is an index running over the nine clusters and l is an index running over the 14 SSP templates. We consider two broad age bins: the recently formed mass with age between 10^6 and 10^8 years and the old or "underlying" population with age between 3×10^8 years and 20 Gyr. The mean star formation rate $<$ SFR $>_2$ in the young bin is then

$$< \mathrm{SFR} >_2 = \sum_{k=1}^{9} \left(\frac{\sum_{l=1}^{7} m^k_l M^k_{clus}}{10^8 y} \right) = 2 \times 10^{-2} M_\odot / y, \tag{6.5}$$

where l runs from the template with age 10^6 years and index l = 1 to the template with age 10^8 years and index l = 7. NGC7418, which has by far the largest mass

of all NCs and also a sizable percentage of young stars, contributes the bulk of this recent star formation. If we leave out this one cluster, $< \text{SFR} >_2 = 3 \times 10^{-3} M_\odot/y$, which is probably a more typical value.

We found in Section 5.6 that the star formation bursts are typically separated by 44 Myr. The mass of stars that is formed per burst M_{fpb} is then

$$M_{fpb} = < \text{SFR} >_2 * 44 Myr = 1.3 \times 10^5 M_\odot \tag{6.6}$$

and each cluster has experienced of the order of 50 bursts in its lifetime.

As discussed in Section 5.6, the mass fractions of the populations in each cluster are uncertain by 50%. Therefore the same is true for the star formation rates we derive. However $< \text{SFR} >_2$ is bigger than $< \text{SFR} >_1$ by almost one order of magnitude. Assuming that contemporaneous star formation rates are typical for the whole existence of the clusters, it seems therefore safe to conclude that nuclear clusters do not form in the very young universe. At the current $< \text{SFR} >_2$ (leaving out NGC7418), NCs need only be $\approx$ 2 Gyr old to build up their typical mass of 5×10^6 $M_\odot$. We already pointed out in Section 5.6 that the nuclear cluster of NGC2139 does not contain any population older than 100 Myr. NGC2139 is also the lightest of the clusters at a mass of only 8×10^5 $M_\odot$ (one could speculate that this could be the typical mass at formation time for a NC). This cluster is very likely forming at the present time. We therefore conclude that NCs form late in the history of the universe.

6.5 Self-enrichment

All evidence seems to point to recurrent star formation as the formation mechanism for nuclear star clusters. Star formation however will lead to stellar winds and explosions of supernovae, thereby enriching the surrounding gas with metals. In fact the nuclei of earlier type galaxies are well-known to be metal-rich. Is it difficult to understand the low metallicities we measure in this context?

Let us draw up a simple model of a "recurrently replenished closed box", simplifying the discussion in Binney and Merrifield (1998, Chapter 5.3). We adopt the instantaneous recycling approximation, i.e. we neglect the delay between formation of the stellar population and the ejection of the heavy elements. At any time there is a mass M_s of stars in the cluster. We now have an infalling cloud of gas with mass M_g and zero metallicity. This gas cloud forms star with some efficiency $f = M_b/M_g$, where M_b is the stellar mass formed in this burst. The mass M_h of heavy elements produced by this star formation burst is $M_h = p \times M_b = pfM_g$, where p is the yield of heavy elements of that generation of stars.

The gas is falling in recurrently. The next infalling gas cloud is assumed to mix completely with the feedback gas. The metallicity of the Nth generation of stars is

then

$$Z = \frac{\text{mass in metals}}{\text{mass in gas}} = \frac{\sum_{i=0}^{N} f^i M_h}{\sum_{i=0}^{N} f^i M_g} = \frac{M_h}{M_g} = pf. \tag{6.7}$$

This zero-th order model is consistent with a roughly constant metallicity over the lifetime of the cluster, no self-enrichment occurs. The actual value of the metallicity then depends on the specific star formation efficiency and yield in the nuclear clusters, which are unknown. Of course this model is too simple. It is well known that supernovae and stellar winds can drive significant parts of the infalling gas out of the cluster. On the other hand the infalling gas is very probably not metal-free, as it has been reprocessed in the stellar disk of the galaxy.

6.6 Formation of Massive Clusters

In Figure 6.1, the average properties of NCs are similar to those of the Fornax UCDs and the nuclei of dE galaxies. Further individual globular clusters, such as ω Cen and G1, have similar properties as well. The average properties of the Milky Way and NGC 5128 globular cluster sample, however are different. Many authors have shown that the most massive globular clusters can be the remaining stripped nuclei of accreted satellite galaxies. In this scenario a nucleated galaxy is stripped off all of its stellar envelope through tidal forces during a minor merger with a bigger galaxy, as e.g. our Milky Way. The nucleus however is compact enough to survive and remains in the halo of the bigger galaxy as a massive globular cluster. This scenario has been proposed for ω Cen (see e.g. Bekki and Freeman, 2003, and references therein), G1 orbiting M31 (e.g. Meylan et al., 2001), the ultra compact dwarf galaxies in the Fornax cluster (Drinkwater et al., 2003) and others. One might therefore speculate that NCs, the nuclei of dEs and UCDs are basically the same thing, albeit in different evolutionary stages of their host galaxy. Remember however that all of the involved samples are biased. The Milky Way globular cluster sample is probably not representative for all globular cluster systems in that it lacks the most massive ones, as shown by the measurements of the most luminous globular clusters of NGC 5128. Our own NC sample only covers the brighter 2/3 of the luminosity function of NCs and might therefore be biased to higher masses. In the case of UCDs, more compact and less luminous specimens might exist without being detected.

Let us take Figure 6.1 at face-value however and accept the hypothesis that the most massive clusters all have a common origin. Accepting this unification picture, star clusters formed in the nuclei of galaxies are, as a class, more massive and more dense than the globular cluster class. It would then be natural to attribute these special properties to their location in the center of their host galaxy at formation

time. It however remains unclear, why the centers of bulge-less galaxies would be special places, conducive to the formation of stellar systems with extreme physical properties.

6.7 Formation of nuclear star clusters

It has become clear during this thesis that nuclear clusters, once formed, continue to grow through repeated episodes of star formation. Not only do the spectra show direct evidence for composite stellar populations. Also the generally young mean ages as well as the age of the last star formation burst point towards recent star formation in all of the clusters. Finally, to reach the very high space densities that are found in these clusters in one star formation event, an extremely high efficiency of star formation is necessary, implying high gas pressure from the surroundings of the forming cluster. Otherwise the gas blown out by feedback will invariably puff up the cluster to a much bigger size (e.g. Geyer and Burkert, 2001). High space densities in a quiescent environment, as is the case in the centers of late type spirals, can be reached more naturally by invoking repeated bursts of star formation from repeated infall of fresh gas. Each infalling cloud will turn some percentage of its mass into stars inside the boundaries of the cluster — thus increasing the space density — before blowing out the remainder through feedback. It has also been shown by Böker et al. (2003a) that there is enough molecular gas (typically 10^7 $M_\odot$) in the central regions of late type spirals in general to support repetitive star formation. In one specific case, IC342, Schinnerer et al. (2003) showed that it is even possible to trace the inflow of molecular gas, both in morphology and kinematics.

The initial formation process of nuclear star clusters however remains completely unknown. Any seed cluster formed in the center of a late type spiral will induce gas falling into the cluster to form stars in its deeper potential well. There are however two scenarios of the circumstances:

Either the appearance of a seed cluster is a random process that can happen anywhere in the central region. In this scenario nuclear clusters are the most massive relatives of globular clusters, the only difference being the formation environment that allows nuclear clusters to grow bigger than the typical globular cluster. It remains however unclear, why one single cluster should grow under these conditions to be so specially massive. As the HST images show, there are sufficient other clusters in their close vicinity that could grow through the same process. Still, there always is only one cluster that is brighter than all others by two magnitudes.

On the other hand the appearance of a nuclear cluster could be a generic property of the centers of spiral disks and thus an essential part of galaxy formation. This scenario has been advocated by Milosavljević (2004) under the assumption of a divergent dark matter density profile. Then sufficient gas can be transported to

the central several 100 pc of the spiral disk. It remains however unclear why this should lead to the formation of a very compact cluster instead of the also commonly observed pseudo-bulges. Also, for very late type galaxies this scenario does not work well, because, as several authors (e.g. Matthews and Gallagher, 2002) find, the rotation curves of very late type spirals are nearly linear, implying a constant surface mass density and a harmonic central potential.

The cluster in the galaxy NGC2139 is especially interesting in this context as it seems we have caught it in the act of forming. The host galaxy is noteworthy for showing some signs of interaction as can be seen from Figure 6.3, taken from The Carnegie atlas of galaxies (Sandage and Bedke, 1994). In the south of the main galaxy there seems to be a presently merging companion, which could trigger the presence of the elongated structure in the center of NGC2139 and thereby the formation of the nuclear cluster.

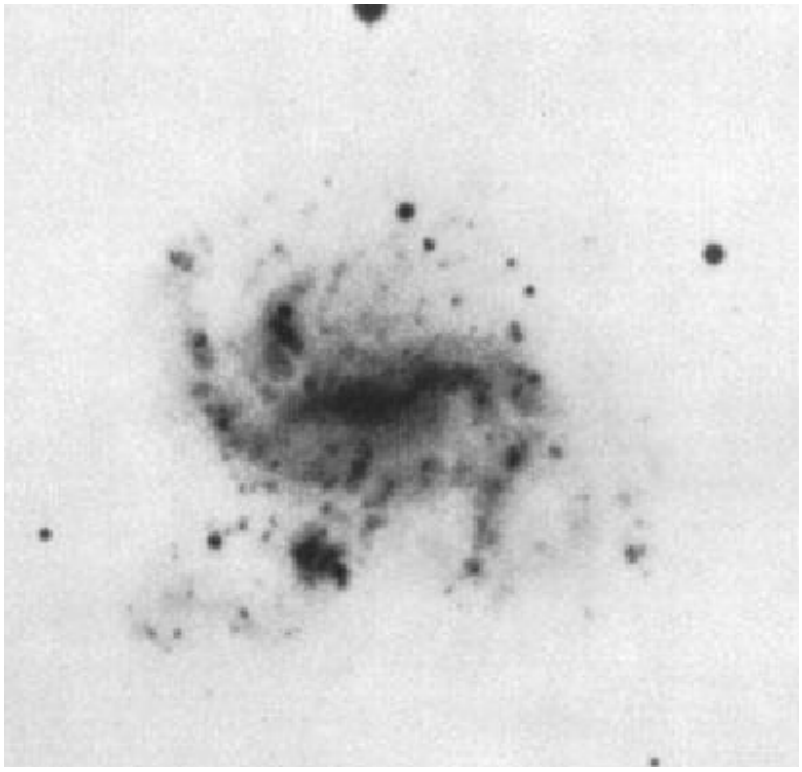

Figure 6.3: An image of NGC2139 taken in the blue wavelength region (around 4050 Å, from Sandage and Bedke, 1994). There seems to be a small companion in the south, possibly presently merging with NGC2139.

Table 6.1: Morphology of the host galaxy

Galaxy	NED Type	Eyeball type	$\log(< A >)$	$\log(A_{lb})$
300	SA	smooth	9.00	8.00
428	SAB	smooth	9.00	7.78
1042	SAB	smooth	9.00	6.78
1493	SB	elong	7.48	7.48
2139	SAB	elong	6.78	6.48
3423	SA	smooth	9.48	7.48
7418	SAB	dust	7.78	6.78
7424	SAB	elong	7.78	7.78
7793	SA	smooth	8.00	8.00

6.8 Relation to the host galaxy

Bars are known to funnel gas into the centers of galaxies (see e.g. Prendergast, 1983, for a review). In the context of the recurring star formation scenario this is an interesting way to provide the necessary gas to either form the cluster or trigger the successive SF bursts. We therefore investigate if the mean age or the age of the last burst correlates with the presence of a bar. Table 6.8 lists the NED classification of the galaxies, the mean age and the age of the last star formation burst. The NED classification is based on large scale images. However the HST WFPC I-band images show the central region in more detail. We therefore also include an eyeball classification based on the HST images (compare Figure 3.1). Galaxies can be either smooth, i.e. show no sign of structure in their disks, or sport a prominent elongated structure (elong), where it remains unclear if this is a small scale bar or a star formation structure. One galaxy, NGC7418, is characterized by a dust lane and therefore does not fall into either of the two categories. It turns out that the NED classification does not correlate with either of the determined ages. In contrast, the presence of an elongated structure is a very good predictor of the mean age of the cluster (but not of the age of the last star formation burst, Figure 6.4). The only outlier, NGC7793, happens to be one of the two clusters where the longest time has elapsed since the last burst of star formation. The emerging picture here is that the recurring star formation may occur on small timescales, however does not necessarily contribute significantly to the mass and to the spectrum of the cluster. On the other hand, when one of these elongated structures is present, the cluster can be significantly rejuvenated. One could speculate that these elongated structures are therefore associated with the build-up of the main mass of the cluster. Whether they are really stellar bars remains left to speculation at the present stage.

It has been suggested by Ferrarese (2002) that the relation between the nucleus

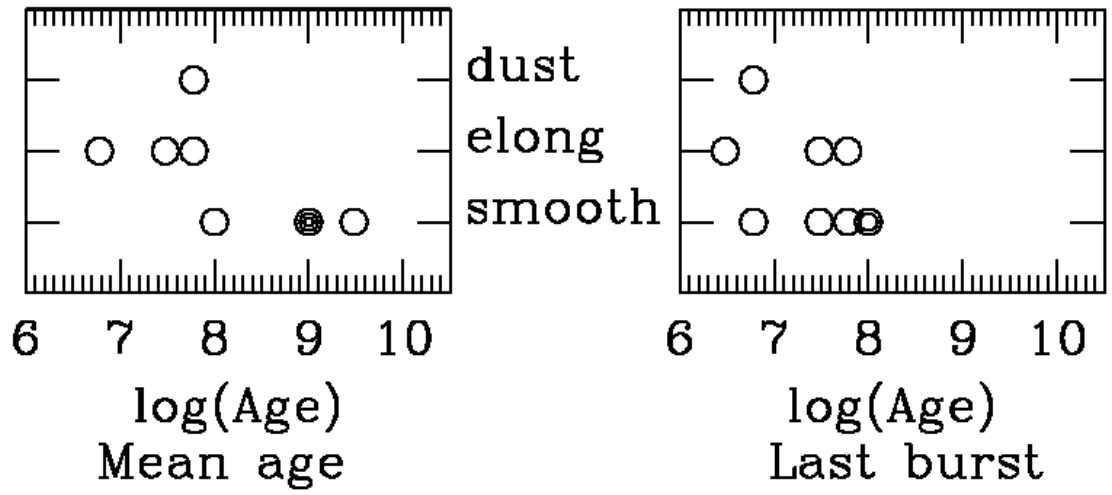

Figure 6.4: Age of the last burst (right) and mean luminosity weighted age of the cluster (left) against the small scale morphology around the cluster. Where several circles are shown this indicates that more than one cluster has these exact properties.

and the large scale properties of a galaxy is a relation between the mass of the central object and the total mass of the dark matter halo. We here explore the crazy idea that in our case the central compact object is a nuclear star cluster. As described in Ferrarese (2002) the total mass of the dark matter halo can be derived from and depends monotonically on the circular velocity in the flat outer parts of the rotation curves of spiral galaxies. These are the parts of the galaxy where the potential is dominated by the dark matter component. A correlation between the mass of the central object and the mass of the dark matter halo can therefore be tested directly from the measurement of the circular velocity. For the galaxies in our sample, resolved Hα rotation curves do only exist for three out of the nine objects. However, the maximum rotation velocity has been measured from the HI 21-cm line widths and homogenized in a convenient way by Paturel et al. (2003) and is available from the LEDA database. Using HI data has an additional advantage: Matthews and Gallagher (2002) show that Hα rotation curves usually do not flatten out in such very late type galaxies. However, HI disks tend to be larger than the stellar disks (e.g. van der Kruit and Shostak, 1984; Ryder et al., 1995; Carignan and Puche, 1990). Indeed Matthews and Gallagher (2002) find that most of the galaxies in their sample have double-peaked global H I profiles, which in turn implies that the outer rotation curve contains a flat or relatively flat region, although it may lie outside the stellar disk.

Figure 6.5 shows the maximum rotation velocity of HI against the mass of the nuclear cluster. There is no apparent correlation. Taking into account that large scale Hubble type is equally unrelated to the properties of the NC, we therefore

conclude that the evolution of nuclear clusters is most likely influenced by local phenomena in the inner disk rather than by the properties of the host galaxy as a whole.

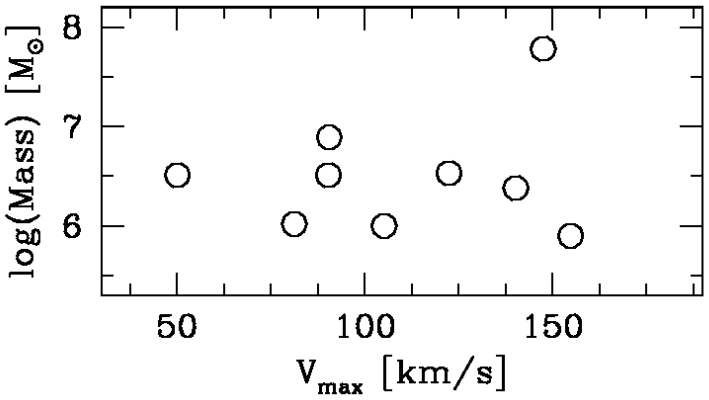

Figure 6.5: Maximum disk rotation velocity v_{max} against mass of the nuclear cluster. No correlation is apparent.

Chapter 7

Conclusions

In which we repeat our main results.

Most bulge-less, very late-type galaxies have been shown to have photometrically distinct, compact nuclear star clusters (several pc in size) at their photometric centers, a stark contrast to the diffuse stellar disk around them. We determine the stellar velocity dispersion for 9 such nuclear star clusters, derived from high resolution spectra taken with UVES at the VLT. For observational reasons we sample the brighter 2/3 of the luminosity range covered by the clusters. In conjunction with light profiles from the WFPC2 camera on board the HST, we also determine their masses. We find them to range from 8×10^5 $M_\odot$ to 6×10^7 $M_\odot$. The nine objects analyzed provide an order of magnitude increase in the number of available determinations, as the only mass known so far had been determined in IC342 to be 6×10^6 $M_\odot$ (Böker et al. 1999). We use population synthesis models to measure mean luminosity weighted ages over the aperture of the extracted spectra. These range from 6×10^6 to 3×10^9 years and are independent of assumed metallicity or internal extinction. We also present evidence that nuclear star clusters are not single-age populations, we therefore fit for the age composition of the clusters. These fits show that the typical metallicity of nuclear clusters is 2/5 solar and that while most of the clusters have moderate extinctions of 0.1 to 0.2 mags in the I band, two out of nine clusters are extincted by 0.7 mag. The mass-to-light ratio as well as the mean luminosity weighted age is not well constrained from these fits. However, we are able to derive the age of the last star formation burst, which was in the mean over our nine sample clusters 44 Myr ago. All of the clusters experienced star formation in the last 100 Myr. The best estimate for the mean star formation rate over the last 2 Gyr is $< \mathrm{SFR} >= 3 \times 10^{-3} M_\odot/y$.

The mass estimates show that as a class, these nuclear clusters in late type galaxies have structural properties similar to the most massive known stellar clusters.

- At around 5×10^6 $M_\odot$ their characteristic masses are much larger than those

of Milky Way globular clusters, except ω Cen. They however fall in the same range as some of the most extreme stellar clusters observed so far, as e.g. G1 in M31 or the most massive globular clusters of NGC 5128.

- The properties of the nuclear clusters show that they are widely distinct from all bulges with measured structural parameters, by orders of magnitude in mass and radius.

- Combining the mass estimates with their effective radii, we find nuclear clusters to be among the clearly distinct stellar systems with the highest mean mass density within their effective radius. Remarkably, although they lie in hugely different environments and thus presumably form in different ways, different sorts of star clusters follow the same mass to density and mass to phase-space density relations.

The age estimates show that nuclear clusters are very different from all other compact clusters in that they experience repeated episodes of star formation over a significant fraction of a Hubble time. There are several independent arguments that support this statement.

- The mean age of the clusters is much smaller than a Hubble time. It would be extremely improbable that by chance all clusters in our sample have formed lately. In the case of repeated star formation however, a young population can dominate the spectrum due to its lower mass-to-light ratio, although a more massive older population might be present in the cluster. This biases the measurement of the mean age to the last star formation episode.

- A fit to the spectra of the clusters is significantly better if allowed to include differently aged SSPs. This demonstrates that populations with different ages are really present in the clusters. We also acertain that the presence of composite populations in the spectra can not be attributed solely to the contamination by disk light.

- Repetitive star formation provides a (maybe too) easy explanation for their large masses concentrated in small spatial regions.

Nuclear clusters are untypical for galaxy centers in that they have low metallicity. We have shown that this is consistent with recurrent star formation. These nuclei then refill periodically with fresh gas, thereby avoiding self-enrichment. The population fits and star formation rates also show that NCs form late in the history of the universe, typically a few Gyr ago.

From their position in their host galaxies, the closest relatives of nuclear clusters appear to be the nuclei of dwarf ellipticals, which could be older and somewhat

more diffuse analogs. Thus, assuming that massive globular clusters and the Fornax ultra-compact dwarf galaxies are the remainders of accreted nucleated dwarf galaxies, all massive clusters with very high effective mass densities could have a common origin in the centers of galaxies. The combination of a galaxy center and a dynamically quiescent environment appears to be conducive to the creation of dense stellar systems with extreme physical properties. These results thus confirm that even in these very late-type galaxies, of overall low stellar surface mass density, the center of the galaxy is 'special'. This leaves open the question, of why some late-type galaxies seem not to have any such clusters.

We relate the properties of the nuclear clusters with the large scale properties of their host galaxies, i.e. Hubble type and circular velocity of the disk, and find no correlation. However the age of the cluster seems to be correlated with the existence of an elongated structure in the inner disk on a scale of < 1 kpc. We therefore conclude that the evolution of nuclear clusters is most likely influenced by local phenomena in the inner disk rather than by the properties of the host galaxy as a whole.

Chapter 8

Outlook

What could be done next.

This project has not been dissimilar to the rest of science in raising as many questions as it has answered.

8.1 Emission line spectra

In this thesis we have analyzed the absorption line spectra of the clusters. However, the UVES data also show emission lines which can yield valuable information. For example the ongoing star formation in several of the clusters is visible through the Hα emission line and others. Figure 8.1 shows the coadded equivalent widths of several emission lines in relation to the ages we determine from the spectral fitting. We determine the emission line equivalent widths by simply interpolating the stellar continuum by eye. This procedure is very inaccurate due to uncertainties in the extent of the wings of the emission lines. We also do not subtract any stellar continuum, thereby likely underestimating especially the strength of the Hα emission line. This is why we use several emission lines and coadd their equivalent widths, hopefully thereby minimizing systematic errors.

Through this preliminary procedure, we find that the emission line strength does not correlate with the mean age of the cluster, but with the age of the last star formation burst. This is to be expected, as the number of ionizing photons declines rapidly with age in young stellar populations. Thus the emission line strength should correlate only with the presence of a population that is young enough to produce significant amounts of ionizing photons. It is important to keep in mind that though encouraging, this relation is not the full story. While we were able to date the age of the last burst, there is at present no really good estimate of its mass. It therefore remains unclear if there really are enough ionizing photons to produce the observed emission lines. We will come back to this problem in the next Section.

The emission line ratios will also be used in the future to derive the temperature, the density and the metallicity of the interstellar medium.

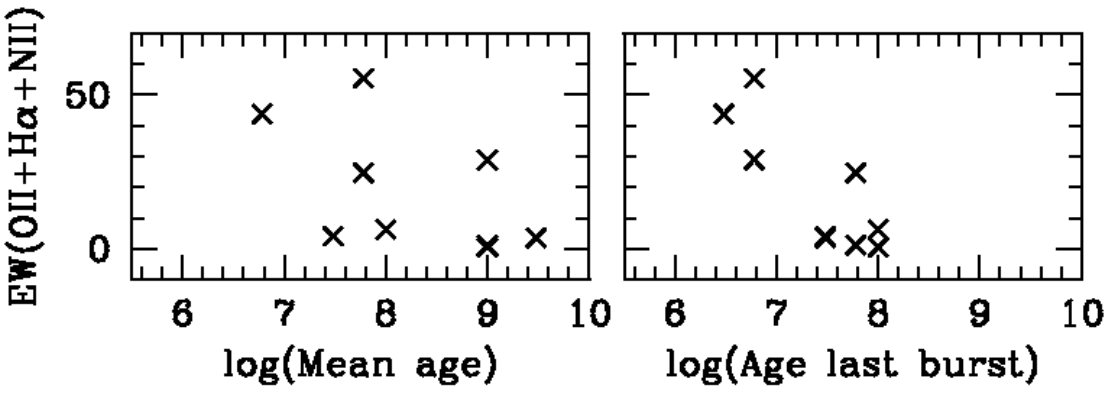

Figure 8.1: The coadded equivalent widths of the OII, Hα and NII emission lines against the mean age (left) and the age of the last star formation burst (right) of the clusters. Note that while the mean age does not correlate with the emission line strength, the age of the last burst does. In each of the plots, two nuclear clusters happen to have the same properties, which is why there are only eight crosses.

8.2 Are there AGN?

Active Galactic Nuclei and their dormant counterparts, the massive black holes, are known to be ubiquitous in the centers of earlier type galaxies. Unfortunately, it is not probable that the presence of a black hole can be determined dynamically for any of the clusters in our sample. Their distances, their faintness and the demise of STIS make it impossible to obtain spatially resolved spectra any time in the near future. Our only hope of finding these possible black holes is through signs of activity of the AGN type. While this activity could prove the presence of black holes in these clusters, the lack of such an activity will not disprove their existence. At present, only one AGN type object in such a late type galaxy is known (NGC 4395, Filippenko and Sargent, 1989).

When investigating the emission line spectra for signs of AGN type activity, two objects in our sample seem promising. The emission lines of the two nuclear clusters in NGC2139 and NGC1042 are noteworthy for having extended wings with FWZI of 400 km/s or more on their Hα, [SII] and [NII] lines. Further NGC1042 is one of the very old clusters with only tiny amounts of young stars, implying that there may not be enough young stars to provide the ionizing photons necessary to power

Table 8.1: Emission lines in NGC1042

Element	λ [Å]	$FWHM_1$ km/s	EW_1 [Å]	$FWHM_2$ km/s	EW_2 [Å]
[NII]	6548	50	0.96	146	1.86
Hα	6563	40	5.84	132	2.91
[NII]	6584	50	3.22	176	6.26
[SII]	6716	47	1.03	139	1.79
[SII]	6731	58	1.25	175	2.02

the emission lines. We therefore concentrate on this cluster for this preliminary analysis. For reference, the stellar velocity dispersion for the cluster is 32 km/s (75 km/s FWHM).

Table 8.2 shows the equivalent widths and FWHM widths of several emission lines in NGC1042. We choose only emission lines in the red part of the spectrum, where the continuum is nearly flat, apart from Hα absorption. Neither of the emission lines can be fit appropriately by a single Gaussian. This is why Table 8.2 quotes two Gaussians, where one is supposedly a "broad component". The two components have been deblended and the fluxes have been determined using the task `splot` in IRAF. Quoting fluxes and equivalent widths is basically equivalent here, as the continuum is approximately constant. Note that the broad component is narrowest for the Hα line. Additionally it is much weaker in relation to the narrow component than for all other emission lines. This is very probably due to the fact that we did not subtract the continuum, i.e. the Hα absorption, properly. For the other emission lines the results are reasonably consistent given the simple procedure used to treat the emission lines. In particular the distinction in a broad and a narrow component seems to be robust as well as the FWHM of each. We will use 50 km/s as the typical FWHM of the narrow component and 160 km/s as that of the broad component.

If not bound, the broad component gas would leave the cluster in less than 1 Myr at its present speed. As it is unlikely that we observe the cluster in such a short-lived phase, it is probable that the gas is bound, i.e. that its speed needs to be less than the escape velocity from the cluster or the central black hole, if one was there. Unfortunately, what the FWHM speed of the broad component means in terms of the escape velocity for the nuclear cluster is not clear. The escape velocity depends strongly on the density profile of the cluster. However, the true run of the density is unknown as explained in Chapter 4.2.

While for a cluster with constant density, the escape speed from the effective radius is only 117 km/s and from the center of the cluster still only 148 km/s, for a probably more realistic power-law profile, escape velocities are much higher,

$v_e \gtrsim 300$ km/s. It is therefore not clear, whether a black hole is needed to keep the gas from escaping from the cluster on a very short timescale.

There are several other ways to diagnose the presence of an AGN. First, emission line ratios can be used to derive the physical state of the gas. In this case for example, the [SII] 6716/6731 ratio is noteworthy for having a value of almost exactly 1. This line ratio is a density diagnostic and this value implies moderately dense gas in this object (Osterbrock, 1989). The composite age fit of Chapter 5.5 also provides an estimate of the ionizing photon flux available from young stars, which can be compared to the intensity of the emission lines. In NGC1042 in particular the line flux predicted from the population analysis falls short of the observed line flux by approximately an order of magnitude.

Several combinations of easily-measured lines can be used to separate objects into one of four categories according to the principal excitation mechanism: normal H II regions, planetary nebulae, objects photoionized by a power-law continuum, and objects excited by shock-wave heating (Baldwin et al., 1981). The [OIII]/Hβ ratio is important for classification but these lines fall in the gap in the UVES data; however NGC1042 was observed in the SDSS. This ratio is 1.3 in the SDSS spectrum, albeit measured on a somewhat larger aperture (fiber with 3 arcsec diameter). Other relevant ratios are: [NII]6583/Hα = 1.1 and [SII]6716+6731/Hα = 0.7. Plotting the derived line ratios in the classification diagrams (see Figure 10.4 in Krolik, 1999) shows that the spectrum is AGN-like. We can not decide at the moment, if the fact that the Hα_1/Hα_2 ratio is much larger than the same ratio in the other emission lines is significant, because this ratio will depend strongly on the subtraction of the stellar continuum. There is one other interesting aspect of NGC 1042 that may or may not be relevant to understanding the above results. NGC 1042 has a Hubble type of SBcd. However, the surface photometry analyses for the HST imaging (Böker et al., 2002, 2003b) show that among the observed sample, this galaxy has the strongest component of central bulge-like excess light.

The combination of line ratios, large linewidths, high gas density, and ionizing photon deficit from stars makes it tempting to interpret this as a weak AGN. Further study of the UVES spectra for all objects in the sample will proceed along the lines sketched this far.

There are however other convincing ways to finally detect the possible AGN and study its properties. AGN are usually identified by a series of properties, besides emission line ratios also radio emission, X-ray emission and variability on short timescales. For NGC4395, the lowest luminosity AGN known to date, all of these observational programs have been carried out successfully. Spatially unresolved radio continuum emission at 20 cm has been observed as well as soft X-ray emission at 0.12-4 keV (Moran et al., 1999). Optical continuum variability of the order of 20% per day has been observed by Lira et al. (1999).

NGC1042 has been observed in the 20 cm line as well (Condon, 1987), albeit

with less spatial resolution than for NGC4395. The resulting radio continuum map is shown in Figure 8.2. In contrast to galaxies of similarly late type, NGC1042 is noteworthy for the *absence* of radio continuum emission at the center of the disk. The bulk of the observed continuum radio emission is probably contributed by supernova remnants (Condon, 1992).

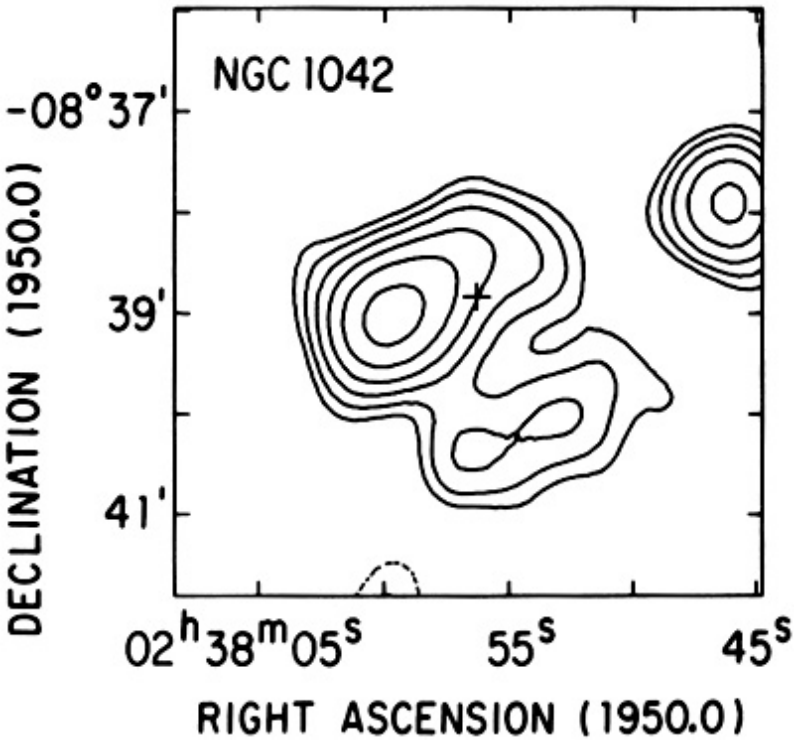

Figure 8.2: The 1.49 Ghz radio continuum map of NGC1042 from Condon (1987). Note that there is no indication for a nuclear source.

In contrast to NGC4395, the possible AGN in NGC1042 is so weak in comparison to the surrounding stellar population, that the AGN is indistinguishable from a young component in the optical spectrum. Monitoring the variability of the emission lines however should be rather straightforward, as these are strong enough to be observed even in the short exposure spectrum of the Sloan Digital Sky Survey. Good seeing will be the most important constraint, in order to separate the nucleus as well as possible from the disk light.

A detection in the X-ray regime with Chandra would probably not be a straightforward proof of the existence of an AGN. As seen in the case of NGC4395, the X-ray luminosity can be very low. While an AGN could easily account for this modest luminosity, it could also be produced by a single bright binary star system emitting near the Eddington limit for a stellar-mass neutron star or black hole. Such an

ambiguity is likely to arise in the case of NGC1042 as well. Elucidating the nature of this object will therefore be a rather complex task, requiring multi-wavelength studies and detailed modelling.

8.3 Cluster dynamics

Nuclear clusters represent a central, massive and compact component in otherwise bulge-less galaxies. The possible presence of black holes in these clusters is of interest in the context of the M-σ relation and in the context of other massive clusters, which might host black holes too. We discuss here some possible formation mechanisms for a black hole.

We found in Chapter 6.3 that runaway mergers are not likely to occur in nuclear clusters following the model as published in Zwart et al. (2004). These authors investigate what happens if a very dense and concentrated cluster forms by following the dynamical evolution of a purely stellar cluster. Formula 6.2 gives the dynamical friction timescale for the inspiral of a massive star starting from the half-mass radius. The value of this starting radius needs to be chosen large enough to acertain that there are enough very massive stars inside this radius in a given cluster to actually merge. In the case of the most massive clusters in our sample, as e.g. NGC7418, there could be enough massive stars inside a significantly smaller starting radius, thus producing the conditions for a runaway merger.

Another property of NCs could help in producing runaway mergers: we have shown that recurrent star formation occurs in the clusters. Therefore a significant amount of gas is present. It has been shown by Escala et al. (2004) for the case of a binary black hole in a galaxy center that the dynamical evolution of the binary can be significantly accelerated by the presence of gas, leading to black hole mergers. For this scenario to work, the mass in gas needs to be larger or comparable to the mass in the binary. In the case of a nuclear cluster the dynamical configuration is much more complex, with probably several massive stars, many low-mass stars and a clumpy gas distribution. To answer the question whether the presence of gas can accelerate the dynamical evolution and therefore induce runaway mergers in NCs will therefore need dedicated simulations including all these components.

8.4 Kinematic center

Although throughout this thesis we have spoken of nuclear clusters as the "nuclei" of their host galaxies (based on their unusual locations and properties), actually nuclear clusters still remain only candidates for being true galaxy nuclei as long as we have not established that they indeed occupy the dynamical centers of their host galaxies. While the clusters do lie very close to the photometric centers of their host

galaxies, the position of the photocenter itself is sometimes not well defined due to the shallow surface brightness distribution and possible asymmetries in the galaxy light distribution due to active star formation. It further remains unclear whether the photometric center really coincides with the dynamical center. This need not be true in the shallow gravitational potentials of late type galaxies. In fact Matthews and Gallagher (2002) report from a kinematic analysis of late type spirals based on longslit spectra of the Hα emission line that nuclear clusters could be offset from the dynamical center of their host galaxy.

We have initiated observations with the ARGUS integral field unit at the VLT to solve this question. We will reconstruct the full 2D Hα velocity field from the measured velocity centroids of the Hα emission lines. A fit to the center of a velocity field readily reveals the recession velocity, kinematic position angle and, most importantly for our purpose, the kinematic center of the galaxy. The derived position of the kinematic (and thus dynamic) center of the galaxy will then be compared to the location of the identified nuclear cluster. We will thus know if the photometric center indeed coincides with the dynamical one as presumed. The kinematic signature of the cluster in the velocity field will be usable as a mass estimate that can be compared to the direct measurements from the velocity dispersions in the UVES data. Non-circular motions will be attributed to either star forming regions or the general lack of a well defined center. In those galaxies where no nuclear cluster was identified in the HST images, the velocity pattern will again directly pinpoint the true center. Either a nuclear cluster will be identified there after all, or we will identify the peculiarities that hindered it from coming into existence.

8.5 Properties of very late type spirals

In the Introduction we have linked the question of understanding the evolution of galaxies to the evolution of their nuclei. In the case of late type galaxies, we have made the point that they actually evolve only passively during their lifetimes, as evidenced by the lack of the telltale signs of violent evolution, namely prominent bulges. To avoid the formation of such a luminous bulge, the galaxies have to avoid two violent processes:

- Major mergers: The frequency of major mergers should be a function of density of galaxies in the environment. Indeed the morphology-density relation (Dressler, 1980) is consistent with this conception. However, although very late type spirals are known to avoid the center of massive galaxy clusters, they can be found in groups (NGC300 and NGC7793 are in the Sculptor group) and even in the Virgo cluster (Binggeli et al., 1985). Exactly how and how much the environment influences the evolution of these pure disk galaxies can only be studied on a statistical basis using large imaging surveys. However

their study has been somewhat neglected because their low surface brightness makes it difficult to identify them. It would seem worthwhile to study, if the stringent constraints on their interaction with their environment, set by the absence of a bulge, can be explained in a more quantitative way.

- Internal dynamical evolution: It has been emphasized by Kormendy and Kennicutt (2004) that: "any nonaxisymmetry in the gravitational potential plausibly rearranges disk gas." Rearranged gas falls to the center of the potential, forms stars and becomes visible as a bulge or pseudobulge. Some of the galaxies show slight central luminosity enhancements, which could be interpreted as small bulges (Böker et al., 2003b), so there is some place for internal evolution. However, galaxies with fairly light, low surface density disks, are stable to the formation of a stellar bar (Mayer and Wadsley, 2004). There is another way for pure disks to avoid bar formation: central point-like mass concentrations can dissolve the bar completely (see e.g. Hasan and Norman, 1990; Shen and Sellwood, 2004). How much central mass is required to destroy the bar differs in different papers, but it seems to be around 5% of the total bar mass for a compact central mass as are the nuclear clusters. Clearly, measurements of the disk mass and its age would reveal which scenario is more convincing.

While late type disks are distinct from their earlier type counterparts through the lack of a central bulge, they are also distinct from irregular galaxies through their at least nearly regular appearance. Producing exceptional objects like the nuclear clusters very likely requires a special (i.e. central) location in the host galaxy which may not be present in more irregular galaxies. It is worth emphasizing here that 25% of the galaxies in Böker et al. (2002) lack a nuclear cluster. We have described in Section 8.4 a project to study the regularity of the velocity fields in the sample galaxies to address the question whether the absence of the NC necessarily implies the absence of a special kinematic center as well. Another approach would be the study of the disk morphology with infrared images. This is more likely to reveal the true morphology and mass distribution in the disk than optical images, as observations in the infrared are less influenced by biases to recent star formation events.

ACKNOWLEDGMENTS

I would like to thank Prof. Hans-Walter Rix as a director of the Max Planck Institut für Astronomie for giving me the opportunity to undertake my research here.

It is a deeply felt pleasure to also express my gratitude to Hans-Walter for being my supervisor during these three years. With never failing patience you have provided me with all that I needed: huge loads of encouraging words and trust, financial resources, and most importantly, you taught me large parts of what I have learned about science.

I thank Prof. Dr. Rainer Spurzem for being willing to be the co-referee of this thesis.

This research would not have been possible without the support and help from a group of close collaborators. I am grateful for the long and fruitful working sessions I had with Torsten Böker, Stephane Charlot, Roeland van der Marel, Dean McLaughlin, and Joe Shields. The mass modelling was done in close collaboration with Roeland van der Marel at STScI during a long- term visit under a directors discretionary research fund grant.

I also would like to thank Marc Freitag, Marla Geha, Luis Ho, Jihane Moultaka, Pierre Ocvirk, Chien Peng, and Marc Sarzi for enlightening discussions at various occasions during the last three years.

Dan Zucker, Nadine Häring and Torsten Böker read parts of this thesis and gave useful comments.

I would also like to thank all colleagues at MPIA who helped me cope in one way or another during my stay here. The following people can only represent them all: David Andersen, Olivier Chesneau, Nadine Häring, Ulrich Hiller, Sebastian Jester, Thilo Kranz, Sebastiano Ligori, Torsten Naab, Laura Pentericci, Jens Rodmann, Johnny Setiawan, and Dan Zucker.

Bibliography

T. Böker, S. Laine, R. P. van der Marel, M. Sarzi, H. Rix, L. C. Ho, and J. C. Shields. A Hubble Space Telescope Census of Nuclear Star Clusters in Late-Type Spiral Galaxies. I. Observations and Image Analysis. *AJ*, 123:1389–1410, Mar. 2002.

T. Böker, U. Lisenfeld, and E. Schinnerer. Molecular gas in the central regions of the latest-type spiral galaxies. *A&A*, 406:87–103, July 2003a.

T. Böker, M. Sarzi, D. E. McLaughlin, R. P. van der Marel, H. Rix, L. C. Ho, and J. C. Shields. A Hubble Space Telescope Census of Nuclear Star Clusters in Late-Type Spiral Galaxies. II. Cluster Sizes and Structural Parameter Correlations. *AJ*, 127:105–118, Jan. 2004.

T. Böker, R. Stanek, and R. P. van der Marel. Searching for Bulges at the End of the Hubble Sequence. *AJ*, 125:1073–1086, Mar. 2003b.

T. Böker, R. P. van der Marel, L. Mazzuca, H. Rix, G. Rudnick, L. C. Ho, and J. C. Shields. A Young Stellar Cluster in the Nucleus of NGC 4449. *AJ*, 121:1473–1481, Mar. 2001.

T. Böker, R. P. van der Marel, and W. D. Vacca. CO Band Head Spectroscopy of IC 342: Mass and Age of the Nuclear Star Cluster. *AJ*, 118:831–842, Aug. 1999.

J. A. Baldwin, M. M. Phillips, and R. Terlevich. Classification parameters for the emission-line spectra of extragalactic objects. *PASP*, 93:5–19, Feb. 1981.

M. L. Balogh, S. L. Morris, H. K. C. Yee, R. G. Carlberg, and E. Ellingson. Differential Galaxy Evolution in Cluster and Field Galaxies at z$\sim$0.3. *ApJ*, 527:54–79, Dec. 1999.

H. Baumgardt, J. Makino, P. Hut, S. McMillan, and S. Portegies Zwart. A Dynamical Model for the Globular Cluster G1. *ApJL*, 589:L25–L28, May 2003.

K. Bekki and K. C. Freeman. Formation of ω Centauri from an ancient nucleated dwarf galaxy in the young Galactic disc. *MNRAS*, 346:L11–L15, Dec. 2003.

R. Bender. Unraveling the kinematics of early-type galaxies - Presentation of a new method and its application to NGC4621. *A&A*, 229:441–451, Mar. 1990.

R. Bender, D. Burstein, and S. M. Faber. Dynamically hot galaxies. I - Structural properties. *ApJ*, 399:462–477, Nov. 1992.

B. Binggeli, A. Sandage, and G. A. Tammann. Studies of the Virgo Cluster. II - A catalog of 2096 galaxies in the Virgo Cluster area. *AJ*, 90:1681–1759, Sept. 1985.

J. Binney and M. Merrifield. *Galactic astronomy*. James Binney and Michael Merrifield. Princeton, NJ : Princeton University Press, 1998. (Princeton series in astrophysics), 1998.

G. Bruzual and S. Charlot. Stellar population synthesis at the resolution of 2003. *MNRAS*, 344:1000–1028, Oct. 2003.

D. Burstein, R. Bender, S. Faber, and R. Nolthenius. Global Relationships Among the Physical Properties of Stellar Systems. *AJ*, 114:1365, Oct. 1997.

D. J. Butler, D. Martínez-Delgado, and W. Brandner. The Stellar Content and Star Formation History of the Late-Type Spiral Galaxy NGC 300 from Hubble Space Telescope Observations. *AJ*, 127:1472–1485, Mar. 2004.

J. A. Cardelli, G. C. Clayton, and J. S. Mathis. The relationship between infrared, optical, and ultraviolet extinction. *ApJ*, 345:245–256, Oct. 1989.

C. Carignan and D. Puche. H I studies of the Sculptor group galaxies. II - NGC 7793. *AJ*, 100:394–402, Aug. 1990.

C. M. Carollo, M. Stiavelli, P. T. de Zeeuw, and J. Mack. Spiral Galaxies with WFPC2.I.Nuclear Morphology, Bulges, Star Clusters, and Surface Brightness Profiles. *AJ*, 114:2366, Dec. 1997.

C. M. Carollo, M. Stiavelli, and J. Mack. Spiral Galaxies with WFPC2. II. The Nuclear Properties of 40 Objects. *AJ*, 116:68–84, July 1998.

G. Chabrier. Galactic Stellar and Substellar Initial Mass Function. *PASP*, 115: 763–795, July 2003.

J. J. Condon. A 1.49 GHz atlas of spiral galaxies with B(T) = +12 or less and delta = -45 deg or greater. *ApJS*, 65:485–541, Dec. 1987.

J. J. Condon. Radio emission from normal galaxies. *ARA&A*, 30:575–611, 1992.

T. J. Davidge. Near-Infrared Adaptive Optics Imaging of the Central Regions of Nearby SC Galaxies. I. M33. *AJ*, 119:748–759, Feb. 2000.

A. I. Diaz, B. E. J. Pagel, M. G. Edmunds, and M. M. Phillips. On the nature of the stellar population in the nucleus of the SD galaxy NGC 7793. *MNRAS*, 201: 49P–55P, Nov. 1982.

A. I. Diaz, E. Terlevich, and R. Terlevich. Near-IR features in late type stars - Their relation with stellar atmosphere parameters. *MNRAS*, 239:325–345, July 1989.

A. Dressler. Galaxy morphology in rich clusters - Implications for the formation and evolution of galaxies. *ApJ*, 236:351–365, Mar. 1980.

M. J. Drinkwater, M. D. Gregg, M. Hilker, K. Bekki, W. J. Couch, H. C. Ferguson, J. B. Jones, and S. Phillipps. A class of compact dwarf galaxies from disruptive processes in galaxy clusters. *Nature*, 423:519–521, May 2003.

A. Escala, R. B. Larson, P. S. Coppi, and D. Mardones. The Role of Gas in the Merging of Massive Black Holes in Galactic Nuclei. I. Black Hole Merging in a Spherical Gas Cloud. *ApJ*, 607:765–777, June 2004.

S. M. Faber and R. E. Jackson. Velocity dispersions and mass-to-light ratios for elliptical galaxies. *ApJ*, 204:668–683, Mar. 1976.

L. Ferrarese. Beyond the Bulge: A Fundamental Relation between Supermassive Black Holes and Dark Matter Halos. *ApJ*, 578:90–97, Oct. 2002.

L. Ferrarese and D. Merritt. A Fundamental Relation between Supermassive Black Holes and Their Host Galaxies. *ApJL*, 539:L9–L12, Aug. 2000.

A. V. Filippenko and W. L. W. Sargent. Discovery of an extremely low luminosity Seyfert 1 nucleus in the dwarf galaxy NGC 4395. *ApJL*, 342:L11–L14, July 1989.

J. A. Frogel. The stellar content of the nuclei of late-type spiral galaxies. *ApJ*, 298: 528–543, Nov. 1985.

J. S. Gallagher, J. W. Goad, and J. Mould. Structure of the M33 nucleus. *ApJ*, 263: 101–107, Dec. 1982.

K. Gebhardt, R. Bender, G. Bower, A. Dressler, S. M. Faber, A. V. Filippenko, R. Green, C. Grillmair, L. C. Ho, J. Kormendy, T. R. Lauer, J. Magorrian, J. Pinkney, D. Richstone, and S. Tremaine. A Relationship between Nuclear Black Hole Mass and Galaxy Velocity Dispersion. *ApJL*, 539:L13–L16, Aug. 2000.

M. Geha, P. Guhathakurta, and R. P. van der Marel. Internal Dynamics, Structure, and Formation of Dwarf Elliptical Galaxies. I. A Keck/Hubble Space Telescope Study of Six Virgo Cluster Dwarf Galaxies. *AJ*, 124:3073–3087, Dec. 2002.

A. E. Gelatt, D. A. Hunter, and J. S. Gallagher. The Star Clusters in the Irregular Galaxy NGC 4449. *PASP*, 113:142–153, Feb. 2001.

M. P. Geyer and A. Burkert. The effect of gas loss on the formation of bound stellar clusters. *MNRAS*, 323:988–994, May 2001.

K. D. Gordon, M. M. Hanson, G. C. Clayton, G. H. Rieke, and K. A. Misselt. The Dusty Starburst Nucleus of M33. *ApJ*, 519:165–176, July 1999.

J. Gorgas, N. Cardiel, S. Pedraz, and J. J. González. Empirical calibration of the λ 4000 Å break. *A&AS*, 139:29–41, Oct. 1999.

A. W. Graham, P. Erwin, N. Caon, and I. Trujillo. A Correlation between Galaxy Light Concentration and Supermassive Black Hole Mass. *ApJL*, 563:L11–L14, Dec. 2001.

N. Häring and H. Rix. On the Black Hole Mass-Bulge Mass Relation. *ApJL*, 604: L89–L92, Apr. 2004.

W. E. Harris. A Catalog of Parameters for Globular Clusters in the Milky Way. *AJ*, 112:1487, Oct. 1996.

W. E. Harris, G. L. H. Harris, S. T. Holland, and D. E. McLaughlin. Structural Parameters for Globular Clusters in NGC 5128. *AJ*, 124:1435–1451, Sept. 2002.

H. Hasan and C. Norman. Chaotic orbits in barred galaxies with central mass concentrations. *ApJ*, 361:69–77, Sept. 1990.

L. Hernquist, P. Hut, and J. Kormendy. A post-core-collapse model for the nucleus of M33. *Nature*, 354:376, Dec. 1991.

G. Kauffmann, T. M. Heckman, S. D. M. White, S. Charlot, C. Tremonti, J. Brinchmann, G. Bruzual, E. W. Peng, M. Seibert, M. Bernardi, M. Blanton, J. Brinkmann, F. Castander, I. Csábai, M. Fukugita, Z. Ivezic, J. A. Munn, R. C. Nichol, N. Padmanabhan, A. R. Thakar, D. H. Weinberg, and D. York. Stellar masses and star formation histories for 10^5 galaxies from the Sloan Digital Sky Survey. *MNRAS*, 341:33–53, May 2003.

J. Kormendy and R. C. Kennicutt. Secular Evolution and the Formation of Pseudobulges in Disk Galaxies. *ARA&A*, 42:603–683, Sept. 2004.

J. Kormendy and R. D. McClure. The nucleus of M33. *AJ*, 105:1793–1812, May 1993.

J. Kormendy and D. Richstone. Inward Bound—The Search For Supermassive Black Holes In Galactic Nuclei. *ARA&A*, 33:581, 1995.

J. Krist and R. Hook.

J. H. Krolik. *Active galactic nuclei : from the central black hole to the galactic environment*. Julian H. Krolik. Princeton, N. J. : Princeton University Press, 1999.

S. S. Larsen. Young massive star clusters in nearby galaxies. II. Software tools, data reductions and cluster sizes. *A&AS*, 139:393–415, Oct. 1999.

S. S. Larsen, J. P. Brodie, B. G. Elmegreen, Y. N. Efremov, P. W. Hodge, and T. Richtler. Structure and Mass of a Young Globular Cluster in NGC 6946. *ApJ*, 556:801–812, Aug. 2001.

C. L. Lawson and R. J. Hanson. *Solving least squares problems*. Prentice-Hall Series in Automatic Computation, Englewood Cliffs: Prentice-Hall, 1974, 1974.

D. Le Borgne, B. Rocca-Volmerange, P. Prugniel, A. Lançon, M. Fioc, and C. Soubiran. Evolutionary synthesis of galaxies at high spectral resolution with the code PEGASE-HR. Metallicity and age tracers. *A&A*, 425:881–897, Oct. 2004.

J.-F. Le Borgne, G. Bruzual, R. Pelló, A. Lançon, B. Rocca-Volmerange, B. Sanahuja, D. Schaerer, C. Soubiran, and R. Vílchez-Gómez. STELIB: A library of stellar spectra at R $\sim$ 2000. *A&A*, 402:433–442, May 2003.

P. Lira, A. Lawrence, P. O'Brien, R. A. Johnson, R. Terlevich, and N. Bannister. Optical and X-ray variability in the least luminous active galactic nucleus, NGC 4395. *MNRAS*, 305:109–124, May 1999.

K. S. Long, P. A. Charles, and G. Dubus. Hubble Space Telescope Spectroscopy of the Nucleus of M33. *ApJ*, 569:204–213, Apr. 2002.

L. A. MacArthur, S. Courteau, and J. A. Holtzman. Structure of Disk-dominated Galaxies. I. Bulge/Disk Parameters, Simulations, and Secular Evolution. *ApJ*, 582:689–722, Jan. 2003.

J. Magorrian, S. Tremaine, D. Richstone, R. Bender, G. Bower, A. Dressler, S. M. Faber, K. Gebhardt, R. Green, C. Grillmair, J. Kormendy, and T. Lauer. The Demography of Massive Dark Objects in Galaxy Centers. *AJ*, 115:2285–2305, June 1998.

C. Maraston, N. Bastian, R. P. Saglia, M. Kissler-Patig, F. Schweizer, and P. Goudfrooij. The dynamical mass of the young cluster W3 in NGC 7252. Heavy-weight globular cluster or ultra compact dwarf galaxy? *A&A*, 416:467–473, Mar. 2004.

D. Marchesini, E. D'Onghia, G. Chincarini, C. Firmani, P. Conconi, E. Molinari, and A. Zacchei. Hα Rotation Curves: The Soft Core Question. *ApJ*, 575:801–813, Aug. 2002.

P. Martini and L. C. Ho. A Population of Massive Globular Clusters in NGC 5128. *ApJ*, 610:233–246, July 2004.

L. D. Matthews and J. S. Gallagher. B and V CCD Photometry of Southern, Extreme Late-Type Spiral Galaxies. *AJ*, 114:1899, Nov. 1997.

L. D. Matthews and J. S. Gallagher. High-Resolution Optical Rotation Curves of Low-Luminosity Spiral Galaxies. *ApJS*, 141:429–442, Aug. 2002.

L. Mayer and J. Wadsley. The formation and evolution of bars in low surface brightness galaxies with cold dark matter haloes. *MNRAS*, 347:277–294, Jan. 2004.

N. McCrady, A. M. Gilbert, and J. R. Graham. Kinematic Masses of Super-Star Clusters in M82 from High-Resolution Near-Infrared Spectroscopy. *ApJ*, 596: 240–252, Oct. 2003.

D. E. McLaughlin. Binding Energy and the Fundamental Plane of Globular Clusters. *ApJ*, 539:618–640, Aug. 2000.

G. Meylan, A. Sarajedini, P. Jablonka, S. G. Djorgovski, T. Bridges, and R. M. Rich. Mayall II=G1 in M31: Giant Globular Cluster or Core of a Dwarf Elliptical Galaxy? *AJ*, 122:830–841, Aug. 2001.

M. Milosavljević. On the Origin of Nuclear Star Clusters in Late-Type Spiral Galaxies. *ApJL*, 605:L13–L16, Apr. 2004.

E. C. Moran, A. V. Filippenko, L. C. Ho, J. C. Shields, T. Belloni, A. Comastri, S. L. Snowden, and R. A. Sramek. The Nuclear Spectral Energy Distribution of NGC 4395, the Least Luminous Type 1 Seyfert Galaxy. *PASP*, 111:801–808, July 1999.

T. Naab and A. Burkert. Statistical Properties of Collisionless Equal- and Unequal-Mass Merger Remnants of Disk Galaxies. *ApJ*, 597:893–906, Nov. 2003.

R. W. O'Connell. Star formation in the semistellar nucleus of M33. *ApJ*, 267:80–92, Apr. 1983.

D. E. Osterbrock. *Astrophysics of gaseous nebulae and active galactic nuclei*. Mill Valley, CA, University Science Books, 1989, 422 p., 1989.

G. Paturel, G. Theureau, L. Bottinelli, L. Gouguenheim, N. Coudreau-Durand, N. Hallet, and C. Petit. HYPERLEDA. II. The homogenized HI data. *A&A*, 412: 57–67, Dec. 2003.

W. Pence. CFITSIO, v2.0: A New Full-Featured Data Interface. In *ASP Conf. Ser. 172: Astronomical Data Analysis Software and Systems VIII*, page 487, 1999.

A. C. Phillips, G. D. Illingworth, J. W. MacKenty, and M. Franx. Nuclei of Nearby Disk Galaxies.I.A Hubble Space Telescope Imaging Survey. *AJ*, 111:1566, Apr. 1996.

K. H. Prendergast. Theoretical studies of gas flow in barred spirals galaxies. In *IAU Symp. 100: Internal Kinematics and Dynamics of Galaxies*, pages 215–220, 1983.

W. H. Press, S. A. Teukolsky, W. T. Vetterling, and B. P. Flannery. *Numerical recipes in FORTRAN. The art of scientific computing*. Cambridge: University Press, 1992, 2nd ed., 1992.

H. Rix and S. D. M. White. Optimal estimates of line-of-sight velocity distributions from absorption line spectra of galaxies - Nuclear discs in elliptical galaxies. *MNRAS*, 254:389–403, Feb. 1992.

S. D. Ryder, L. Staveley-Smith, D. Malin, and W. Walsh. A new optical and H I study of the nearby galaxy NGC 1313. *AJ*, 109:1592–1607, Apr. 1995.

A. Sandage and J. Bedke. *The Carnegie atlas of galaxies*. Washington, DC: Carnegie Institution of Washington with The Flintridge Foundation, 1994, 1994.

W. L. W. Sargent, P. L. Schechter, A. Boksenberg, and K. Shortridge. Velocity dispersions for 13 galaxies. *ApJ*, 212:326–334, Mar. 1977.

E. Schinnerer, T. Böker, and D. S. Meier. Molecular Gas and the Nuclear Star Cluster in IC 342: Sufficient Inflow for Recurring Star Formation Events? *ApJL*, 591:L115–L118, July 2003.

J. Shen and J. A. Sellwood. The Destruction of Bars by Central Mass Concentrations. *ApJ*, 604:614–631, Apr. 2004.

S. M. Simkin. Measurements of Velocity Dispersions and Doppler Shifts from Digitized Optical Spectra. *A&A*, 31:129, Mar. 1974.

J. V. Smoker, R. D. Davies, and D. J. Axon. H I and optical observations of the NGC 428 field. *MNRAS*, 281:393–405, July 1996.

L. Spitzer. *Dynamical evolution of globular clusters*. Princeton, NJ, Princeton University Press, 1987, 191 p., 1987.

A. W. Stephens and J. A. Frogel. The Structure and Stellar Content of the Central Region of M33. *AJ*, 124:2023–2038, Oct. 2002.

D. Thomas, C. Maraston, and R. Bender. Stellar population models of Lick indices with variable element abundance ratios. *MNRAS*, 339:897–911, Mar. 2003.

J. Tonry and M. Davis. A survey of galaxy redshifts. I - Data reduction techniques. *AJ*, 84:1511–1525, Oct. 1979.

S. C. Trager, G. Worthey, S. M. Faber, D. Burstein, and J. J. Gonzalez. Old Stellar Populations. VI. Absorption-Line Spectra of Galaxy Nuclei and Globular Clusters. *ApJS*, 116:1, May 1998.

S. van den Bergh. The Semistellar Nucleus of M33. *ApJ*, 203:764–765, Feb. 1976.

P. C. van der Kruit and G. S. Shostak. Studies of nearly face-on spiral galaxies. III - H I synthesis observations of NGC 1058 and the mass distribution in galactic disks. *A&A*, 134:258–267, May 1984.

R. P. van der Marel and M. Franx. A new method for the identification of non-Gaussian line profiles in elliptical galaxies. *ApJ*, 407:525–539, Apr. 1993.

G. Worthey. Comprehensive stellar population models and the disentanglement of age and metallicity effects. *ApJS*, 95:107–149, Nov. 1994.

G. Worthey and D. L. Ottaviani. Hγ and Hδ Absorption Features in Stars and Stellar Populations. *ApJS*, 111:377, Aug. 1997.

S. F. P. Zwart, H. Baumgardt, P. Hut, J. Makino, and S. L. W. McMillan. Formation of massive black holes through runaway collisions in dense young star clusters. *Nature*, 428:724–726, Apr. 2004.